Constraints on Ecosystem Carbon and Water Flux Estimates in a Temperate Australian Evergreen Forest

By

Alexandre A. Renchon

A thesis submitted in fulfilment of the requirements for the degree of

Doctor of Philosophy

April 2019

WESTERN SYDNEY UNIVERSITY

Hawkesbury Institute for the Environment

Acknowledgements

First I thank my supervisor Elise Pendall for her continuous advice and support, my co-supervisors Belinda Medlyn and Matthias Boer for their regular inputs, and the entire HIE staff for their help.

I wouldn't have been able to complete this PhD without the contribution of the Pendall lab, especially Anne Griebel, Dan Metzen, Craig Barton and Chelsea Maier.

I also received important guidance on modelling from Vanessa Haverd from CSIRO, and advice on data analysis from Christopher Williams from Clark University.

I thank my master thesis supervisor Marc Aubinet for encouraging me to do a PhD.

I thank my mother Magdeleine Avignon who supported me throughout and particularly during my fourth and last year of my PhD.

I thank all my fellow PhD students at HIE for the great time we had together, supporting each other.

Declaration of Authenticity

The work presented in this thesis is, to the best of my knowledge and belief, original except as acknowledged in the text. I hereby declare that I have not submitted this material, either in full or in part, for a degree at this or any other institution.

[redacted]

Table of contents

List of figures 7

List of tables 11

Abstract 12

1 Chapter 1. Introduction 14

1.1 Context: carbon cycle perturbation and climate change 14
1.2 Constraints on fluxes 15
1.3 Ecosystem-atmosphere exchange 17
1.3.1 Direct measurements 17
1.3.2 Remote sensing 18
1.3.3 Empirical and mechanistic modelling 19
1.4 Knowledge gaps and objectives 21
1.5 Candidate contributions 25

2 Chapter 2. Upside-down fluxes Down Under: CO_2 net sink in winter and net source in summer in a temperate evergreen broadleaf forest 28

2.1 Abstract 28
2.2 Introduction 30
2.3 Material and methods 33
2.3.1 Site description 33
2.3.2 Environmental measurements 33
2.3.3 Net ecosystem exchange 34
2.3.4 Vertical turbulent flux (F_{CT}) 35
2.3.5 Storage flux (F_{CS}) 36
2.3.6 Gap-filling of environmental variables and NEE separation into gross fluxes 37
2.3.7 Flux footprint 38
2.3.8 Energy balance 38
2.3.9 Surface conductance 38
2.3.10 Dynamics of canopy phenology (leaf area index, litter and leaf production) and photosynthetic capacity 39
2.3.11 Analysis of light-response of NEE 40
2.3.12 Leaf gas exchange spot measurements 40

2.3.13 Remotely sensed land surface greenness 40
2.4 Results 41
2.4.1 Seasonality of environmental drivers and leaf area index 41
2.4.2 Seasonality of carbon and water fluxes 43
2.4.3 Diurnal trend of CO_2 flux and drivers in winter and summer 43
2.4.4 Analysis of NEE light response curve 44
2.4.5 Atmospheric demand (D) and soil drought control on GPP, ET, G_s and WUE 45
2.4.6 Canopy phenology control of GPP 47
2.5 Discussion 50
2.6 Conclusions 55
3 Chapter 3. Phenology of canopy dynamics and carbon fluxes in a temperate evergreen broadleaved forest: a data-model comparison 56
3.1 Abstract 56
3.2 Introduction 58
3.3 Materials and methods 62
3.3.1 Site description, measurements and modelling 62
3.3.2 Photosynthetic capacity 68
3.3.3 Seasonal allocation of F_{NPP} to leaf growth 68
3.4 Results 70
3.4.1 Environmental drivers and phenology of LAI_{EVI} 70
3.4.2 Phenology of climate, canopy and observed fluxes 72
3.4.3 Model results 73
3.4.3.1 Model simulation vs. observation 73
3.4.4 Comparison between simulations with constant and varying LAI 75
3.5 Discussion 78
3.5.1 Environmental drivers and phenology of LAI_{EVI} 78
3.5.2 Model results 80
3.6 Conclusions 82
4 Chapter 4. Contribution of soil CO_2 efflux to seasonal and diurnal dynamics of ecosystem respiration in a dry sclerophyll forest 83
4.1 Abstract 83
4.2 Introduction 84
4.3 Materials and methods 87

4.3.1 Site description 87
4.3.2 Meteorological drivers 87
4.3.3 R_{eco} data 88
4.3.4 R_{soil} data 89
4.3.5 R_{AG} estimation 92
4.3.6 Seasonal and diel apparent temperature sensitivity 92
4.3.7 Alternate predictions of R_{eco} using R_{soil} 92
4.4 Results 94
4.4.1 Temporal dynamics of soil and ecosystem respiration and their drivers 94
4.4.2 R_{soil} and R_{eco} response to T_{soil} and θ with the DAMM model 96
4.4.3 Seasonal and diurnal pattern of R_{soil}, R_{eco} and R_{AG} 98
4.4.4 Constraining R_{eco} using R_{soil} 101
4.5 Discussion 105
4.5.1 Seasonal and diurnal patterns of R_{soil}, R_{eco} and R_{AG} 105
4.5.2 Bias of nighttime and daytime ecosystem respiration by standard methods? 105
4.5.3 Modelling R_{eco} using the DAMM model 108
4.6 Conclusions 108
5 Chapter 5. Conclusions 110
5.1 Most important results 110
5.2 Recommended measurements and analysis for better constraints of fluxes in evergreen broadleaf forests in South-East Australia 111
6 Supplementary information 114
7 References 141

List of figures

Figure 1.1 Visualisation of the theoretical volume and three components of the mass balance equation in the eddy-covariance method. 17

Figure 1.2 Soil CO_2 efflux automated chamber 18

Figure 1.3 Light response curve of net ecosystem exchange 19

Figure 1.4 Response of ecosystem and soil respiration to soil temperature and soil moisture. 20

Figure 1.5 Conceptual figure of the dissertation. 24

Figure 2.1 Time series of fluxes and weather 42

Figure 2.2 Diurnal trend of fluxes, surface conductance and vapour pressure deficit 46

Figure 2.3 Half-hourly measured NEE vs. PPFD, coloured by D 48

Figure 2.4 NEE µmol m^{-2} s^{-1} light response parameters, calculated for different bins of climatic drivers 49

Figure 2.5 Light saturated GPP or A_{max}, ET or T, WUE, G_s or g_s responses to D and SWC. . 51

Figure 2.6 Photosynthetic capacity and surface conductance response to leaf area index and enhanced vegetation index. 54

Figure 3.1 Time series of leaf area index, precipitation, air temperature, net ecosystem productivity and evapotranspiration over the 2001-2017 period. 71

Figure 3.2 Phenology of leaf area index. 73

Figure 3.3 Response of light saturated (F_{PPFD} > 1000) net ecosystem productivity (F_{NEP}, µmol m^{-2} s^{-1}) and evapotranspiration (F_{ET}, mm half-$hour^{-1}$) to vapor pressure deficit (D, kPa) and soil water content (SWC, brightness indicates SWC, for 5 quantiles, from wet (dark) to dry (bright)). Dots indicates average of y value for 4 quartiles of x, shading indicates standard error. Blue line: CABLE with varying LAI. Red line: CABLE with constant LAI. Cyan line: eddy-covariance observation. 74

Figure 3.4 Monthly fluxes, canopy dynamic and meteorological drivers. 76

Figure 3.5 Annual net ecosystem productivity vs. LAI, T_{air} and precipitation. 79

Figure 3.6 Monthly photosynthetic capacity vs. leaf area index. 79

Figure 4.1 Time series of daily ecosystem respiration, soil respiration, soil moisture and soil temperature over the 2014-2017 period. 95

Figure 4.2 Daily (night median) response of soil respiration (a-f) and ecosystem respiration (g) to soil temperature and soil moisture, and Dual-Arrhenius Michaelis Menten (DAMM) model fit. 97

Figure 4.3 Seasonal and diurnal pattern of observed simultaneous soil respiration, ecosystem respiration, above-ground respiration, soil temperature and air temperature. 99

Figure 4.4 Apparent seasonal and diurnal temperature responses of observed ecosystem and soil respiration and estimated above-ground respiration, fitted to the Lloyd and Taylor (1994) equation. 100

Figure S2. 1. Canopy height model at AU-Cum site, generated at 30m spatial resolution using LiDAR data. 114

Figure S2. 2. Nighttime net ecosystem exchange, vertical turbulent exchange and change in storage vs. friction velocity, for 5 air temperature quantiles and 4 soil moisture quantiles. . 115

Figure S2. 3. Vertical wind and CO_2 concentration cospectra, and comparison with the Kaimal model, using 2014-2017 data. 116

Figure S2. 4. Diurnal course of all measured, quality checked and u_* filtered net ecosystem exchange of CO_2 (NEE) and CO_2 vertical turbulent exchange (F_{CT}). 117

Figure S2. 5. Footprint climatology at AU-Cum site, for all data, unstable, neutral and stable conditions. 118

Figure S2. 6. Energy balance closure (sensible + latent heat flux vs. net radiation - ground heat flux), daily data from 2014 through end of 2016. 119

Figure S2. 7. Light response of F_{CT}, NEE, and NEE after stationarity filter, colored by D. . 120

Figure S2. 8. Time series (bottom: January 2014, top: January 2017) and diurnal course of fluxes and environmental drivers over the three years of the study. 121

Figure S2. 9. Similar to figure 2.1, but with NDVI instead of EVI in panel (d). 122

Figure S2. 10. Similar to figure 2.6, but with NDVI instead of EVI. 124

Figure S2. 11. Light-saturated (photosynthetically active radiation (PAR) > 1000 µmol m^{-2} s^{-1}) C-fluxes: net ecosystem exchange (NEE), gross primary productivity (GPP) and ecosystem respiration (R_{eco}, from SOLO) versus air temperature. 125

Figure S2. 12. Wavelet coherence between D and GPP, for the four year study (2014 through 2017). 126

Figure S2. 13. G_s or g_s vs. GPP or Amax/√D. 127

Figure S3. 1. Comparison of estimates of LAI at the Cumberland Plain site. 128

Figure S3. 2. Monthly change in leaf area index over time ($dLAI_{EVI}/dt$, m^2 m^{-2} $month^{-1}$) as a function (multiple linear regression) of monthly precipitation (Precip, mm $month^{-1}$) and monthly average air temperature (T_{air}, °C). 129

Figure S3. 3. Wavelet coherence between dEVI/dt and monthly precipitation (mm $month^{-1}$) 130

Figure S3. 4. r-square of linear regression of yearly peak of LAI_{EVI} vs. sum of precipitation X months before LAI_{EVI} max. 131

Figure S3. 5. Correlation between half-hourly eddy-covariance net ecosystem productivity observation (F_{NEP} obs., µmol m^{-2} s^{-1}) and evapotranspiration observation (F_{ET} obs., mm hh^{-1}) and CABLE half-hourly F_{NEP} and F_{ET} model. 132

Figure S4. 1. Responses of nighttime CO_2 flux (vertical turbulent exchange F_{CT}, change in storage F_{CS} and ecosystem respitation $R_{eco} = F_{CT} + F_{CS}$) to friction velocity ($u_*$). 135

Figure S4. 2. Seasonal course (monthly median of half-hourly data) of ecosystem respiration (R_{eco}), soil respiration (R_{soil}), above-ground respiration (R_{AG}), soil temperature (T_{soil}) and air temperature (T_{air}). 137

Figure S4. 3. Diurnal pattern of soil and ecosystem respiration, soil and air temperature, for each month of the year in 2017. 138

Figure S4. 4. Contribution of F_{CT} and F_{CS} to R_{eco} observation at night, (a) versus time and (b) versus air temperature. 139

Figure S4. 5. Linear regression of nightly R_{soil} vs. R_{eco}, for 6 R_{soil} chambers. 140

List of tables

Table 1.1 Mean daily air temperature (MAT, °C) and mean annual precipitation (MAP, mm) of the three broadleaf evergreen woodland equipped with a flux tower in South-East Australia. 22

Table 1.2 List of symbols and acronyms 27

Table 2.1 Annual fluxes and weather over the 2014-2017 period. 44

Table 3.1 List of symbols and acronyms 61

Table 3.2 CABLE-POP parameters fitted to measured data. 67

Table 3.3 Annual precipitation, air temperature, leaf area index, and net ecosystem productivity over the period 2001-2017. 77

Table 4.1 Fitted parameters values and quality of fit of the semi-mechanistic heterotrophic respiration model Dual Arrhenius Michaelis Menten (DAMM) 102

Table 4.2 Parameter values (E_0 and R_{10} and quality of fit (r-square)) of Lloyd and Taylor fitted on monthly or half-hourly ecosystem respiration, soil respiration and above-ground respiration. 103

Table 4.3 Quality of fit (R^2) of models fitted on night-time observation of ecosystem respiration (R_{eco}), using half-hourly night data or median of night data with at least 10 half-hours, for different driver sets. 104

Table S3. 1. Parameters of CABLE after PEST optimisation, refer to Table 3.1 for description and units 133

Table S3. 2. Parameter correlation matrix (pearson's r), refer to Table 3.1 for description and units 134

Abstract

Land-atmosphere carbon dioxide (CO_2) exchange is the least constrained component of the global carbon cycle, yet it is driving most of its inter-annual variability. Seasonal and inter-annual variations in weather conditions affect biological activity and resulting CO_2 exchanges, but the relative effects of phenology and climate on carbon cycling are not well understood. I used four years of eddy covariance data from a eucalypt woodland located near Sydney, South-East Australia, to better constrain carbon and water fluxes from this forest type. At our site, I observed a seasonal pattern of net ecosystem exchange (NEE) that contrasted with other flux tower sites in eucalypt forests. While similar Australian sites acted as a sink of carbon all year, especially in summer, our site behaved as a net sink of carbon in winter and a net source of carbon in summer. This pattern was caused by ecosystem respiration (R_{eco}) driving the seasonal course of NEE, as the seasonal variability in R_{eco} was bigger than that of gross primary production (GPP). GPP was limited by stomatal closure at high vapour pressure deficit in summer, but remained high in winter, while R_{eco} was high in summer, and lower in winter. Leaf area index (LAI) varied seasonally, increasing rapidly mid-summer to reach a maximum in late summer, then decreased until the next year. LAI was a good predictor of canopy photosynthetic capacity (PC). The Community Atmosphere Biosphere Land Exchange (CABLE) land surface model was able to reproduce the seasonal variation in forest NEE but did not entirely capture canopy PC variability. Leaf demography, which is not accounted for in the model, may partly explain the mismatch between observed and simulated PC and should be further investigated. Our estimate of allocation of net primary productivity (NPP) to leaf growth was dynamic seasonally, which contrasts with the CABLE model assumption of a constant allocation factor in the evergreen broadleaf forest biome. Improved representation of dynamic allocation may further improve carbon cycle predictions in evergreen broadleaf forests. A semi-mechanistic model of heterotrophic

respiration, the Dual Arrhenius Michaelis Menten model (DAMM), reproduced seasonal variations of R_{soil} and R_{eco} as a function of temperature and soil moisture. Daily to seasonal patterns of soil CO_2 efflux were similar to those of R_{eco}, but hourly dynamics were different, as R_{soil} remained nearly constant overnight while R_{eco} decreased. While decreasing air temperatures overnight may explain decreasing above-ground respiration, advection could also play a role, leading to a systematic data bias. Additional continuous, high frequency measurements of R_{eco} components such as leaf respiration, stem respiration and soil respiration would improve mechanistic understanding of nighttime and daytime R_{eco}. While weather variation was the major control of fluxes, the canopy phenology (leaf area index variations and leaf demography) also played an important role and needs to be incorporated in land surface models.

1 Chapter 1. Introduction

1.1 Context: carbon cycle perturbation and climate change

The global carbon cycle has been remarkably perturbed in recent years. While the total global amount of carbon is fixed, its distribution among different pools (atmosphere, biomass, soils, ocean) is being changed, mainly by anthropogenic burning of fossil fuels. Exchanges of carbon (fluxes) among these pools are being studied to understand and predict fluxes and pools of carbon in the future.

This perturbation of the global carbon cycle is causing climate change, mainly from increasing greenhouse gas concentrations in the atmosphere, especially CO_2. Understanding ecosystem-atmosphere feedbacks is crucial to make predictions of future climate under different emission scenarios (Le Quéré et al. 2018). Ecosystems have been consistently absorbing about 55% of anthropogenic emissions of CO_2 per year (30% by land, 24% by the oceans), with 45% remaining in the atmosphere. That is, as human emissions have increased in magnitude, so have ecosystem sinks (Le Quéré et al. 2018). However, the future strength of these sinks is uncertain as climate change impacts increase.

In the last several decades, important research efforts have been directed at estimating ecosystem carbon fluxes, by measurements and modelling. Among them, a global network of flux towers (https://fluxnet.fluxdata.org/) has been used for continuous monitoring of meteorological drivers (precipitation, air temperature, air humidity, radiation, soil moisture and temperature, etc.) and atmospheric CO_2 concentration and land-atmosphere carbon, water and energy exchange at several hundred locations worldwide (Baldocchi 2008).

In forest ecosystems, it has been found that biomass has been increasing globally, leading to a "greening of the earth" visible from satellites (Zhu et al. 2016, Song et al. 2018). This increase in forest productivity in recent years is believed to be caused mainly by CO_2

fertilisation, as increased atmospheric CO_2 means more "food" for forests globally (Tans et al. 1990, Friedlingstein et al. 1995, Kicklighter et al. 1999, Yang et al. 2016). However, increased atmospheric CO_2 also means that global air temperature is increasing, which is impacting forests' productivity positively or negatively depending on regional climate (Lindroth et al. 1998, Phillips et al. 2008, Pilegaard et al. 2011, Keenan et al. 2014). Another consequence of climate change is a change in precipitation regime, which is also greatly impacting forest-atmosphere CO_2 exchange depending on context (Schuur 2003, Betts et al. 2004). The responses of forest ecosystems to these changes are also a function of nutrient availability, and elevated CO_2 may not increase productivity if there are other limiting factors (Ellsworth et al. 2017).

It remains uncertain how ecosystems will respond with further CO_2 increase, temperature increase and precipitation regime change (Keenan et al. 2016). Predicting these changes is particularly challenging because they will occur under unprecedented conditions, so there is no data available for comparison. Moreover, observations of fluxes only started about thirty years ago (Wofsy et al. 1993), and it is hard to make prediction on a time resolution greater than the available data. Evaluating current and recent patterns and mechanisms of ecosystem-atmosphere CO_2 exchange provides important contextual information against which to compare future carbon cycling as climate change impacts become stronger.

1.2 Constraints on fluxes

To improve our understanding of forests-atmosphere exchange, it is key to reconcile estimates of fluxes over various spatial and temporal resolutions. Spatial resolution ranges from the molecular level to leaf level to forest level to global level. Time resolution ranges from second to hourly to daily to seasonal to inter-annual and further. At each step of increasing resolution, emergent properties appear, mechanisms become important that did not matter at lower resolution (Ponge 2005, Ollinger et al. 2013). For example, the age-related

decline in forest growth results from a stand level process and cannot be inferred by studying individual tree physiology (Smith and Long 2001). Another example, in time, is the impact of climate change on a forest land-atmosphere exchange, which becomes important at inter-annual scales, but is not relevant at second, daily or seasonal time resolutions.

It is also important to reconcile independent measurement estimates from different methods, as physically they should all yield to the same data, depending on the uncertainties associated with the methods (Brændholt et al. 2018). For example, estimates of net primary productivity can be estimated by directly measuring the change in pool size over time (allometries, the size of the trees), and by measuring the fluxes over the same time period (with flux towers, or by upscaling small scale flux chambers) (Anić et al. 2018, Ouimette et al. 2018, Teets et al. 2018). Mismatch between independent measurements presents an opportunity to identify what may be causing a measurement error (Van Gorsel et al. 2007). Agreement between independent measurements can help increase the confidence and robustness of the data.

Similarly, it is important to reconcile experimental science (data) with modelling science (Medlyn et al. 2015). Mismatch, again, presents an opportunity to improve the model and the data (McHugh et al. 2017, Restrepo-Coupe et al. 2017a). Agreement between model and data increases the confidence and robustness in both the model and the data (Dou and Yang 2018). This holds true for both empirical and mechanistic models. While empirical models are likely to work best in the narrow space and time on which they are calibrated, mechanistic models can be challenging to parameterize and may give the right result for the wrong reason. Nevertheless, mechanistic models can have broad predictive power across space and time (Rastetter et al. 2003).

1.3 Ecosystem-atmosphere exchange

1.3.1 Direct measurements

The only quasi-direct method to measure ecosystem-atmosphere exchange of carbon, water and energy is flux tower or eddy-covariance method (Baldocchi et al. 2001a). This method consists of solving a mass balance inside a theoretical volume that can be visualised as a cube going from the soil to above the canopy vertically (Figure 1.1). Any quantity produced or absorbed inside the volume can either a) change the concentration of the quantity inside the volume or b) be exchanged vertically or c) be exchanged horizontally. For example, for exchange of CO_2, we have:

$$F_{NEE} = F_{CT} + F_{CS} + F_{CA} \tag{1.1}$$

where F_{NEE} is the net ecosystem exchange, F_{CT} is the vertical exchange (by turbulence), F_{CS} is the change in storage, and F_{CA} is the net horizontal exchange (out – in) also called advection. In practice, we usually consider that F_{CA} is negligible compared to F_{CT} and F_{CS} under conditions of sufficient turbulence.

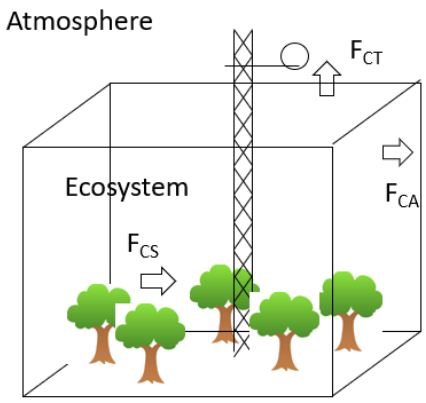

Figure 1.1 Visualisation of the theoretical volume and three components of the mass balance equation in the eddy-covariance method. F_{CT} is the vertical exchange (by turbulence), F_{CS} is the change in storage, and F_{CA} is the net horizontal exchange (out – in) also called advection.

Fluxes can also be measured from components, such as soil CO_2 efflux or leaf gas exchange, via different techniques, for example mass balance in a closed chamber like shown in Figure

1.2. As the chamber is closed, the terms F_{CT} and F_{CA} of the mass balance in equation 1.1 are nil (F_{CA} is nil if the chamber is installed properly), and F_{NEE} (soil CO_2 efflux) is equal to F_{CS}, the increase of CO_2 inside the volume over time. The sum of components (gas exchange from soil, leaves, stem) should be equal to the ecosystem CO_2 exchange.

Figure 1.2 Soil CO_2 efflux automated chamber

1.3.2 Remote sensing

While flux tower and component chambers are valuable tools, allowing direct measurements of carbon exchange, they can only be deployed in a limited number of ecosystems or sites globally. Satellite remote sensing products provide data over the entire globe, but they are not direct measurements of carbon exchange.

Many remote sensing platforms, such as Moderate-resolution Imaging Spectro-radiometer (MODIS), produce spectral information (reflectance) indicating the greenness of a pixel observed by the satellite, that can be translated into products such as enhanced vegetation index (EVI) or the normalized difference vegetation index (NDVI). These products, collected at frequent intervals (e.g., ~weekly), may be correlated with forest fluxes (such as gross primary productivity or net ecosystem exchange (Restrepo-Coupe et al. 2016)) and forest canopy indices (such as leaf area index or leaf demography (Wu et al. 2016b)). MODIS products have been developed as proxies of biosphere activity, such as GPP (Zhang et al. 2017), allowing global estimates at 500-m resolution for 8-day intervals for the years 2000-2016. The ~weekly values of MODIS products provides a high enough temporal resolution to

demonstrate seasonal patterns of biosphere activity, or phenology at the ecosystem scale (Noormets 2009). Continued development of remote sensing products by calibrating reflectance data against ecosystem measurements will provide constraints on global models of carbon cycling and improve understanding of carbon – climate feedbacks.

1.3.3 Empirical and mechanistic modelling

Patterns in ecosystem carbon, water and energy fluxes can be described in many ways, for example using responses to environmental drivers. A commonly described response is the light response curve, often described using 3 empirical parameters (Figure 1.3), fitted using a non-linear equations such as Mitscherlich (Mitscherlich 1909, Aubinet et al. 2001):

$$F_{NEE} = -(N_{es} + R_d)\left(1 - e^{-\alpha F_{PPFD}/N_{es}+R_d}\right) + R_d \qquad 1.1$$

where F_{NEE} is the net ecosystem exchange (µmol m^{-2} s^{-1}), N_{es} is the net exchange at light saturation (µmol m^{-2} s^{-1}), R_d is the respiration in the dark (µmol m^{-2} s^{-1}), α is the quantum yield efficiency (µmol CO_2 µmol photon^{-1}), and F_{PPFD} is photosynthetic photon flux density (µmol m^{-2} s^{-1}).

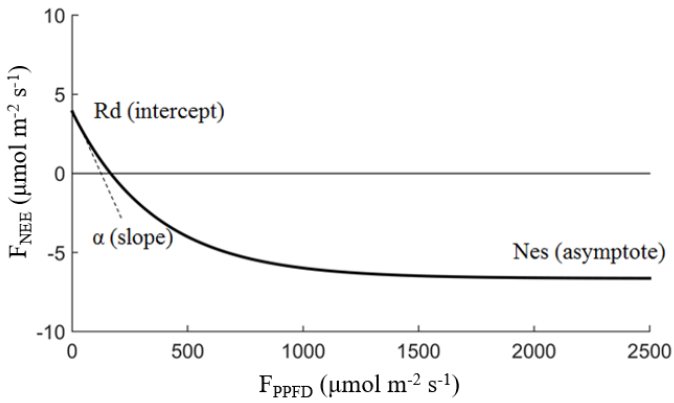

Figure 1.3 Light response curve of net ecosystem exchange. F_{NEE} is the net ecosystem exchange, F_{PPFD} is photosynthetic photon flux density, R_d is dark respiration, α is the quantum yield and N_{es} is the net exchange at light saturation.

Another common empirically described pattern is the response of soil respiration or ecosystem respiration to air or soil temperature and soil moisture, with a pattern similar to what is shown in Figure 1.4, where the response to temperature follows an exponential pattern, and the response to soil moisture follows a unimodal pattern.

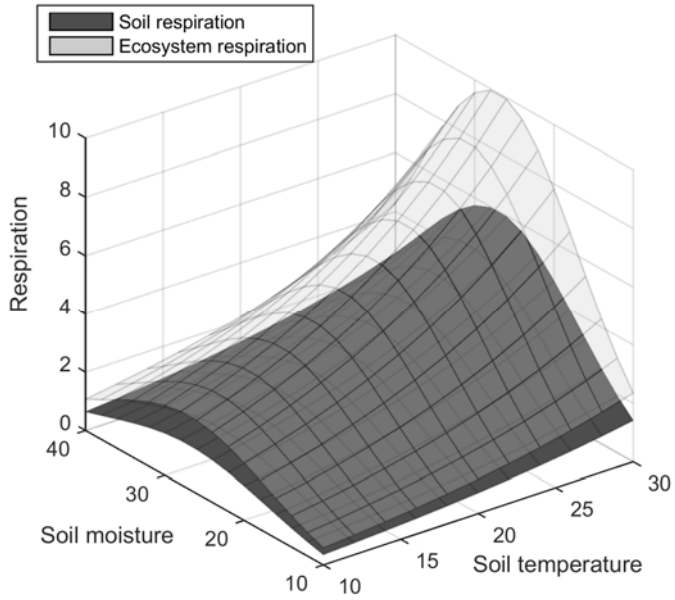

Figure 1.4 Response of ecosystem and soil respiration to soil temperature and soil moisture.

These patterns can be empirically described with prescribed linear or non-linear equations by fitting parameters, or data can be fitted automatically with methods such as an artificial neural network. Such methods can be useful to fill gaps of missing or bad data (Moffat et al. 2007) and can be insightful to compare parameter values in time and space (Aubinet et al. 2001). However, they lack mechanistic foundation, and are therefore limited in a narrow time and space.

Mechanistic models allow generalization of equations in space and time, allowing for global estimates if parameters are available, and for future prediction. However, they are more difficult to build as mechanisms must be identified, appropriate equations need to be developed, and parameters need to be determined.

The optimum soil moisture (θ) for soil respiration (pattern described in Figure 1.4), for example, can be explained by two distinct mechanisms. Heterotrophic respiration is limited at low θ due to low concentration of soluble carbon substrates at the reactive site of microbe enzymes, and is also limited at high θ due to anoxic conditions (Davidson et al. 2012).

Current land surface models (LSMs), such as the Community Atmosphere Biosphere Land Exchange model (CABLE), are composed of both mechanistic and empirical equations, and aim to increase their ability to capture mechanisms (Kowalczyk et al. 2006, Haverd et al. 2013, De Kauwe et al. 2015, Trudinger et al. 2016, Haverd et al. 2018).

1.4 Knowledge gaps and objectives

In this dissertation, I focus on a broadleaf evergreen forest in South-East Australia equipped with a flux tower, the Cumberland Plain SuperSite (AU-Cum on Fluxnet) of the TERN OzFlux network (http://www.ozflux.org.au/). This site is located within 2 km of the EucFACE site and is a similar forest (Ellsworth et al. 2017). Four other broadleaf evergreen forests are equipped with flux towers in South-East Australia (Beringer et al. 2016), the Wombat forest, the Tumbarumba forest, the Warra forest and the Whroo forest. All four sites are colder, and all except Whroo are wetter than the Cumberland Plain site (Table 1.1). Tumbarumba and Wombat have been shown to act as sinks of carbon all year long, in particular in summer (Keith et al. 2012, Hinko-Najera et al. 2017b). Understanding Southeast Australian forest fluxes is urgent, considering that climate change is making this region warmer and drier (Le Quéré et al. 2018), and that climatic drivers of ecosystem carbon fluxes in this region are not well established, especially in a region experiencing increasing heat waves and droughts (Van Gorsel et al. 2016).

Table 1.1 Mean daily air temperature (MAT, °C) and mean annual precipitation (MAP, mm) of the five broadleaf evergreen forests equipped with a flux tower in Southeast Australia.

Site	MAT (°C)	MAP (mm)	Latitude S	Longitude E	FLUXNET ID
Cumberland Plain	18	800	-33.6153	150.7236	AU-Cum
Tumbarumba	9	1380	-35.6566	148.1517	AU-Tum
Wombat	12	880	-37.4222	144.0944	AU-Wom
Warra	10	1000	-43.0950	146.6545	AU-Wrr
Whroo	16	400	-36.6732	145.0294	AU-Whr

In the second chapter, I addressed the knowledge gap of ecosystem-atmosphere carbon and water exchange patterns in a broadleaf evergreen woodland warmer and drier than previously observed sites, over the 4-year period 2014-2017. I aimed to identify the relevant mechanisms leading to the observed temporal and driver response patterns. In particular, I focused on the role of air and soil water stress. Atmospheric demand, also called vapor pressure deficit (VPD), is determined by air temperature and relative humidity, and can be calculated using Clausius-Clapeyron relationship to calculate water vapor pressure at saturation, VPD being the difference between the actual vapor pressure and saturation vapor pressure. VPD is a measure of atmospheric demand for water. At AU-Cum, air temperature goes very high (up to 48 °C), and relative humidity can be very low (down to 5%), leading to very high VPD (10 kPa). I studied the interaction of VPD and soil water content on stomatal regulation at the canopy scale, as well as the seasonal dynamics of ecosystem respiration and its response to temperature and soil moisture. I also investigated the influence of leaf area index on canopy photosynthetic capacity and how this changes temporally.

In the third chapter, I used the knowledge gained from the second chapter to improve land surface modelling of forests similar to our site. I used a land surface model (CABLE) to simulate our site fluxes and tested the importance of LAI phenology in an evergreen broadleaf forest such as the Cumberland Plain. LAI and leaf demography dynamic play an important role on forest productivity (Piao et al. 2019). The role of canopy phenology has been investigated in high latitude (Walker et al. 1995, Barr et al. 2004, Richardson et al.

2010) and tropical forests (Asner et al. 2000, Wu et al. 2016b), but its importance in temperate broadleaved evergreen forests is less well understood (Restrepo-Coupe et al. 2016).

In the fourth chapter, I addressed the knowledge gap of the common mismatch between ecosystem respiration and soil respiration (Van Gorsel et al. 2007, Phillips et al. 2017, Barba et al. 2018). I aimed to strengthen the robustness of our soil and ecosystem respiration datasets by analysing the contribution of soil CO_2 efflux to ecosystem respiration. I evaluated the capacity of a semi-mechanistic model of heterotrophic respiration, the dual Arrhenius Michealis Menten (DAMM) model to predict both soil and ecosystem respiration (Davidson et al. 2012, Drake et al. 2018). In particular, I focused on overnight patterns of hourly soil and ecosystem respiration and discussed what relevant measurement assumptions and ecological mechanisms may explain differences between overnight patterns of soil and ecosystem respiration. I also discussed the implications of our results for estimation of daytime ecosystem respiration, which was recently suggested to be over-estimated by standard methods because they do not account for light inhibition of leaf respiration (Wehr et al. 2016, Keenan et al. 2018, Keenan et al. 2019). Figure 1.5 presents the overall dissertation structure. Table 1.2 present a list of symbols and acronyms used in the text.

Constraints on fluxes in evergreen broadleaf woodland

Chapter 1 Introduction

Chapter 2 Cumberland Plain flux data (NEE, ET, GPP, R_{eco})
- Seasonal and diurnal pattern
- Key mechanism explaining these patterns

Chapter 3 Reconcile flux data and land surface model
- Do LSM (CABLE) reproduce flux data?
- Importance of LAI dynamics
- What is the next gap?

Chapter 4 Reconcile flux data and chamber data
- Seasonal and diurnal pattern of soil CO_2 efflux and R_{eco}
- Response to temperature and SWC (DAMM model)
- What is the next gap?

Chapter 5 Conclusions

Figure 1.5 Conceptual figure of the dissertation. NEE is net ecosystem exchange, ET is evapotranspiration, GPP is gross primary productivity, R_{eco} is ecosystem respiration, LSM is land surface model, CABLE is the Community Atmosphere Biosphere Land Exchange model (Haverd et al. 2018), LAI is leaf area index, SWC is soil water content, DAMM is the Dual Arrhenius Michaelis Menten model (Davidson et al. 2012).

1.5 Candidate contributions

Chapter 2 is published as Renchon, A. A., Griebel A., Metzen D., Williams C. A., Medlyn B., Duursma R. A., Barton C. V. M., Maier C., Boer M. M. Isaac P., Tissue D., Resco de Dios V., Pendall E. "Upside-down fluxes Down Under: CO_2 net sink in winter and net source in summer in a temperate evergreen broadleaf forest." *Biogeosciences, 2018, vol. 15, p. 3703-3716* (2018).

In chapter 2, the candidate conceived and designed the analysis, contributed as a team member to the collection and maintenance necessary to obtain the data, conducted all the data analyses, and drafted the manuscript. Anne Griebel and Dan Metzen provided assistance with eddy covariance data processing; Chris Williams, Remko Duursma, Belinda Medlyn, Matthias Boer, Peter Isaac and Victor Resco de Dios provided guidance on data analysis; David Tissue established the initial experiment; and Elise Pendall supervised the project. All co-authors provided comments on the manuscript.

Chapter 3 and 4 are in preparation for submission as journal articles. The PhD candidate is first author on chapters 3 and 4. Chapter 3 has the following co-authors: Vanessa Haverd, Cathy Trudinger, Anne Griebel, Daniel Metzen, Matthias Boer, Belinda Medlyn and Elise Pendall. In chapter 3, the candidate conceived, designed and conducted the analysis, and drafted the manuscript. Vanessa Haverd and Cathy Trudinger provided important help to run and parameterise the CABLE model. Anne Griebel and Dan Metzen provided assistance with data processing. Elise Pendall supervised the project. All co-authors provided comments on the manuscript.

Chapter 4 has the following co-authors: John Drake, Debjani Sihi, Eric Davidson, Nina Hinko-Najera, Catriona Macdonald, NamJin Noh, Mark Tjoelker and Elise Pendall. In chapter 4, the candidate conceived, designed and conducted the analysis, participated in the

collection and treatment of the raw data, and drafted the manuscript. John Drake, Catriona Macdonald and Mark Tjoelker established the initial soil respiration experiment. Debjani Sihi and Eric Davidson provided guidance in data analysis. Elise Pendall supervised the project. All co-authors provided comments on the manuscript.

Table 1.2 List of symbols and acronyms

Acronym (equation)	Definition	Unit
a_f	Allocation to leaf growth	fraction
A_{max}	Leaf net assimilation	µmol m^{-2} s^{-1}
D	Vapor pressure deficit	kPa
ET (F_{ET})	Evapotranspiration	mmol m^{-2} s^{-1} or mm $[time]^{-1}$
EVI	Enhanced vegetation index	-
F_{CS}	Change in storage of CO_2	µmol m^{-2} s^{-1}
F_{CT}	Vertical turbulent exchange of CO_2	µmol m^{-2} s^{-1}
F_{Lfall}	Litter fall	m^2 m^{-2}
$F_{Lgrowth}$	Leaf growth	m^2 m^{-2}
GEP (F_{GEP})	Gross ecosystem production (positive is uptake)	µmol m^{-2} s^{-1} or gC m^{-2} $[time]^{-1}$
GPP (F_{GPP})	Gross primary productivity (negative is uptake)	µmol m^{-2} s^{-1} or gC m^{-2} $[time]^{-1}$
G_s	Surface conductance	mol m^{-2} s^{-1}
g_s	Leaf conductance	mol m^{-2} s^{-1}
k_f	Canopy turnover	$[time]^{-1}$
LAI (L)	Leaf area index	m^2 m^{-2}
NDVI	Normalized difference vegetation index	-
NEE (F_{NEE})	Net ecosystem exchange	µmol m^{-2} s^{-1} or gC m^{-2} $[time]^{-1}$
NEP (F_{NEP})	Net ecosystem production (positive is net uptake)	µmol m^{-2} s^{-1} or gC m^{-2} $[time]^{-1}$
NPP (F_{NPP})	Net primary productivity (negative is net uptake)	µmol m^{-2} s^{-1} or gC m^{-2} $[time]^{-1}$
PC	Photosynthetic capacity	µmol m^{-2} s^{-1} or gC m^{-2} $[time]^{-1}$
PPFD (F_{PPFD})	Photosynthetic photon flux density	µmol m^{-2} s^{-1} or gC m^{-2} $[time]^{-1}$
R_{AG}	Above-ground respiration	µmol m^{-2} s^{-1} or gC m^{-2} $[time]^{-1}$
R_{eco}	Ecosystem respiration	µmol m^{-2} s^{-1} or gC m^{-2} $[time]^{-1}$
R_{leaf}	Leaf respiration	µmol m^{-2} s^{-1}
R_{soil}	Soil respiration	µmol m^{-2} s^{-1} or gC m^{-2} $[time]^{-1}$
R_{stem}	Stem respiration	µmol m^{-2} s^{-1}
T_{air}	Air temperature	°C
T_{soil}	Soil temperature	°C
u_*	Friction velocity	m s^{-1}
WUE	Water use efficiency	µmol $mmol^{-1}$
θ	Soil water content	m^3 m^{-3}

2 Chapter 2. Upside-down fluxes Down Under: CO_2 net sink in winter and net source in summer in a temperate evergreen broadleaf forest

2.1 Abstract

Predicting the seasonal dynamics of ecosystem carbon fluxes is challenging in broadleaved evergreen forests because of their moderate climates and subtle changes in canopy phenology. I assessed the climatic and biotic drivers of the seasonality of net ecosystem-atmosphere CO_2 exchange (NEE) of a eucalyptus-dominated forest near Sydney, Australia, using the eddy covariance method. The climate is characterized by a mean annual precipitation of 800 mm and a mean annual temperature of 18 °C, hot summers and mild winters, with highly variable precipitation. In the four-year study, the ecosystem was a sink each year (-225 g C m^{-2} y^{-1} on average, with a year to year standard deviation of 108 g C m^{-2} y^{-1}); inter-annual variations were not related to meteorological conditions. Daily net C uptake was always detected during the cooler, drier winter months (June through August), while net C loss occurred during the warmer, wetter summer months (December through February). Gross primary productivity (GPP) seasonality was low, despite longer days with higher light intensity in summer, because vapour pressure deficit (D) and air temperature (T_a) restricted surface conductance during summer while winter temperatures were still high enough to support photosynthesis. Maximum GPP during ideal environmental conditions was significantly correlated with remotely sensed enhanced vegetation index (EVI, $r^2 = 0.46$) and with canopy leaf area index (LAI, $r^2 = 0.29$), which increased rapidly after mid-summer rainfall events. Ecosystem respiration (R_{eco}) was highest during summer in wet soils and lowest during winter months. R_{eco} had larger seasonal amplitude compared to GPP, and therefore drove the seasonal variation of NEE. Because summer carbon uptake may become

increasingly limited by atmospheric demand and high temperature, and ecosystem respiration could be enhanced by rising temperature, our results suggest the potential for large-scale seasonal shifts in NEE in sclerophyll vegetation under climate change.

2.2 Introduction

Forests and semi-arid biomes are responsible for the majority of global carbon storage by terrestrial ecosystems (Dixon et al. 1994, Schimel et al. 2001, Pan et al. 2011, Poulter et al. 2014). Photosynthesis and respiration by these biomes strongly influence the seasonal cycle of atmospheric CO_2 (Keeling et al. 2001, Baldocchi et al. 2016). Continuous measurements of land-atmosphere exchanges of carbon, energy and water provide insights into the seasonality of forest ecosystem processes, which are driven by the interactions of climate, plant physiology and forest composition and structure (Xia et al. 2015). Net ecosystem exchange (NEE) seasonality is relatively well understood in cool-temperate ecosystems; deciduous trees can only photosynthesize when they have leaves and NEE dynamics are thus principally influenced by the phenology of canopy processes. NEE of deciduous forests thus has a more pronounced seasonality than that of evergreen conifer forests at similar latitudes (Novick et al. 2015). For high-latitude evergreen conifer forests, NEE seasonality is strongly limited by cold temperature limitation of photosynthesis (Kolari et al. 2007) and respiration. In contrast, seasonality of NEE in evergreen broadleaf forests, typically occurring in warm-temperate and tropical regions, is much less well understood (Wu et al. 2016b, Restrepo-Coupe et al. 2017a).

The seasonality of gross primary productivity (GPP) in evergreen broadleaf forests may be driven by climate (e.g. dry/wet seasons) and/or by canopy dynamics (Wu et al. 2016b). In tropical evergreen forests, air temperature and day length are similar seasonally, but precipitation seasonality can be strong, with higher radiation and temperature (1 or 2 °C higher) in the dry season (Trenberth 1983, Windsor 1990). Counter-intuitively, GPP can be higher during the dry season, as cloud cover may limit productivity in the wet season (Graham et al. 2003, Saleska et al. 2003, Hutyra et al. 2007). Canopy dynamics can be an important determinant of GPP seasonality in evergreen broadleaf forests; although leaves are

present in the canopy year-round in evergreen canopies, LAI may show considerable temporal variability seasonally as new leaves are produced and old leaves die, especially during leaf flush and senescence periods (Duursma et al. 2016, Wu et al. 2016b). The leaf light use efficiency and water use efficiency may both vary as leaves age: young leaves and old leaves are less efficient than mature leaves, reflecting changes in photosynthetic capacity (Wilson et al. 2001, Wu et al. 2016b). The timing of leaf flush and senescence can depend on the environment and on species; environmental stress, such as drought, can induce the process of senescence (Munné-Bosch and Alegre 2004, Lim et al. 2007).

In temperate evergreen broadleaved forests, such as eucalypt-dominated sclerophyll vegetation in Australia, precipitation can be seasonal or aseasonal; furthermore, day length and temperature vary significantly between winter and summer. GPP can be limited by frost during winter and by drought during summer. Atmospheric demand indicated by high vapor pressure deficit (D) and soil drought have different impacts on GPP, but they can interact to impact surface conductance (G_s) (Medlyn et al. 2011, Novick et al. 2016). In Australia's temperate eucalypt forests, canopy rejuvenation takes place in summer and is linked to heavy rainfall events (Duursma et al. 2016). However, since leaf flushing and shedding occur simultaneously in eucalypt canopies (Pook 1984b, Duursma et al. 2016), the overall canopy volume can remain stable while the distribution of canopy volume changes with height (Griebel et al. 2015). Eucalypt forests in southeast Australia have been found to act as carbon sinks all year long, with greater uptake in summer (van Gorsel et al. 2013, Hinko-Najera et al. 2017a). Although canopy characteristics are key to understanding ecosystem fluxes, their dynamics in Australian ecosystems can be particularly challenging to detect using standard vegetation indices (Moore et al. 2016). Nevertheless, the normalized difference vegetation index (NDVI) has successfully explained variability in photosynthetic capacity in Mediterranean, mulga and savanna ecosystems (Restrepo-Coupe et al. 2016).

The environmental and biotic controls on the seasonal dynamics of ecosystem fluxes in broadleaved evergreen forests are still poorly understood. Our objective was to determine the seasonality of ecosystem CO_2 and H_2O fluxes in a dry sclerophyll Eucalyptus forest; I evaluated the role of environmental drivers (PPFD, T_a, SWC and D) and canopy dynamics (as measured with EVI, LAI, litter fall and leaf age) in regulating the seasonal patterns of net ecosystem exchange (NEE), gross primary productivity (GPP), ecosystem respiration (R_{eco}), evapotranspiration (ET) and surface conductance (G_s) in an evergreen forest near Sydney, Australia. I also compared leaf-level to ecosystem-level water and carbon exchange in response to drivers, in order to gain confidence in our results and gain insights about the emergent properties from leaf to ecosystem scale. I hypothesised that canopy phenology (LAI and leaf age) explains temporal variation in photosynthetic capacity (PC) and G_s. I anticipated that the ecosystem would be a carbon sink all year long.

2.3 Material and methods

2.3.1 Site description

The field site is the Cumberland Plain (AU-Cum in Fluxnet) forest SuperSite (Resco de Dios et al. 2015) of the Australian Terrestrial Ecosystem Research Network (http://www.ozflux.org.au), located 50 km west of Sydney, Australia, at 19 m elevation, on a nearly flat floodplain of the Nepean-Hawkesbury River (latitude -33.61518; longitude 150.72362). Mean mid-afternoon (3 pm) temperature is 18 °C (max. 28.5 °C in January and min. 16.5 °C in July) and average precipitation is 801 mm year^{-1} (mean monthly max. is 96 mm in January, and min. is 42 mm in September). The soil is classified as a Kandosol and consists of a fine sandy loam A horizon (0-8 cm) over clay to clay loam subsoil (8-40 cm), with pH of 5 to 6 and up to 5% organic C in the top 10 cm (Karan et al. 2016). The flux tower is in a mature dry sclerophyll forest, with 140 Mg C ha^{-1} aboveground biomass and stand density of ~500 trees ha^{-1}. The stand hosts a large population of mistletoe (*Amyema miquelii*), which decreases in abundance with increasing distance to the flux tower. The canopy structure comprises three strata, and the predominant canopy tree species are *Eucalyptus moluccana* and *E. fibrosa*. While individual trees can exceed 25 m height, an airborne LiDAR survey from November 2015 indicates an average canopy height of ~24 m within a 300 m radius of the flux tower (supplement Figure S2. 1). The mid-canopy stratum (5-12 m) is dominated by *Melaleuca decora* and the understory is dominated by *Bursaria spinosa* with various shrubs, forbs, grasses and ferns present in lower abundance.

2.3.2 Environmental measurements

Air temperature (T_a) and relative humidity (RH) were measured using HMP45C and HMP155A (Vaisala, Vantaa, Finland) sensors at 7 m and 29 m heights, respectively. Vapour pressure deficit (D) was estimated from T_a and RH. Photosynthetic photon flux density above the canopy (PPFD, µmol m^{-2} s^{-1}) was measured using an LI190SB (Licor Inc., Lincoln NE,

USA), and incoming and outgoing short and longwave radiation were measured using a CNR4 radiometer (Kipp & Zonen, Delft, Netherlands). Ancillary data were logged on CR1000 or CR3000 dataloggers (Campbell Scientific, Logan UT, USA) at 30 min intervals. Mixing ratios of CO_2 in air were also measured at 0.5 m, 1 m, 2 m, 3.5 m, 7 m, 12 m, 20 m, and 29 m above the soil surface using a LI840A Gas Analyzer (Licor Inc., Lincoln NE, USA); data from each height were logged on a CR1000 datalogger once every 30 minutes (1 minute air sampling per height).

Ground heat flux and soil moisture were averaged between two locations to represent the variable shading in the tower footprint. One location had a HFP01 heat flux plate and the other had a self-calibrating heat flux plate (HFP01SC) (Hukseflux, XJ Delft, Netherlands) installed at 8 cm below the soil surface. The heat flux plates were paired with a CS616 water content reflectometer (Campbell Scientific, Logan UT) installed horizontally at 5 cm below the soil surface and a TCAV averaging thermocouple (Campbell Scientific, Logan UT) installed with thermocouples at 2 cm and 6 cm below the soil surface for each pair. Another CS616 was installed vertically measured average soil water content from 7 to 37 cm (CS616). Rainfall was measured at an open area with a tipping bucket 2 km away from the study site.

2.3.3 Net ecosystem exchange

Continuous land-atmosphere exchange of CO_2 mass (net ecosystem exchange, NEE) was quantified from direct measurements of the different components of the theoretical mass balance of CO_2 in a control volume:

$$\mathrm{NEE} = \mathrm{F_{CT}} + \mathrm{F_{CS}} \tag{2.1}$$

where F_{CT} is the vertical turbulent exchange flux, and F_{CS} is the rate of change in storage flux. Advection fluxes are assumed negligible when atmospheric turbulence is sufficient (Baldocchi et al. 1988, Aubinet et al. 2012), and when quality flags of stationarity and

turbulence development test were good (Foken et al. 2004). I used change-point detection of the friction velocity (u_*) threshold (Barr et al. 2013) to determine the turbulence threshold above which NEE (the sum of F_{CT} and F_{CS}) is independent of u_*. However, I found no clear dependence of NEE on u_* hence no clear threshold (Figure S2. 2), so I used a threshold of 0.2 m s^{-1} to be conservative.

The calculation of each term, and the assumptions required for them to be representative of each half-hour flux are detailed below.

2.3.4 Vertical turbulent flux (F_{CT})

The vertical turbulent fluxes of CO_2 (F_{CT}, µmol m^{-2} s^{-1}) and water (F_{WT}, mmol m^{-2} s^{-1}) were measured using the eddy-covariance method (Baldocchi et al. 1988). Density of CO_2 or water vapor (open-path IRGA (LI-7500A, LI-COR Inc., Lincoln NE, USA)) and vertical wind speed (w) (CSAT 3D sonic anemometer (Campbell Scientific Inc., Logan UT, USA)) were measured at 10 Hz frequency at 29 m above the ground, and logged on a CR-3000 datalogger (Campbell Scientific, Logan UT, USA). Vertical turbulent fluxes were calculated from the 10 Hz data, using Eddy-Pro© software. Statistical tests for raw data screening included spike count/removal, amplitude resolution, drop-outs, absolute limits and skewness and kurtosis tests (Vickers and Mahrt 1997). Low and high frequency spectral correction followed (Moncrieff et al. 2004), and (Moncrieff et al. 1997). The calculation allowed for up to 10% of missing 10 Hz data. Fluxes were rotated into the natural wind coordinate system using the double rotation method (Wilczak et al. 2001). Time lags between the sonic and IRGA were compensated using covariance maximization, within a window of plausible time lags (Fan et al. 1990). I applied the block averaging method to calculate each half-hour average and fluctuation relative to the average, to calculate the covariance (Gash and Culf 1996). Density fluctuations in the air volume were corrected using the WPL terms (Webb et al. 1980). Each half-hourly flux was associated with a quality flag (0: good quality, 1: keep for integrations,

discard for empirical relationships, 2: remove from the data); these flags accounted for stationarity tests and turbulence development tests which are required for good turbulent flux measurements (Foken et al. 2004). In our 4-year record, 51% of F_{CT} fluxes had a flag of 0, 32% had a flag of 1 and 17% had a flag of 2. Although the tower height (29 m) is rather close to the average canopy height (24 m), cospectra analysis showed good quality turbulent fluxes (the high frequency followed the -4/3 slope, thus I did not find any indications of systematic dampening in the cospectra, see Figure S2. 3).

2.3.5 Storage flux (F_{CS})

The change in storage flux (F_{CS}, µmol m^{-2} s^{-1}) was measured using a CO_2 profiler system, such that change of storage flux timestamp was the same as the turbulent flux timestamp. The change in storage flux was calculated as (Aubinet et al. 2001):

$$F_{CS} = \frac{P_a}{R\,T_a}\int_0^h \frac{dC(z)}{dt}dz \tag{2.2}$$

where P_a is the atmospheric pressure (P_a), T_a is the temperature (K), R is the molar gas constant, and C(z) is CO_2 (µmol m^{-3}) at the height z. CO_2 is measured in ppm and converted to µmol m^{-3} using ideal gas law equation, where the air temperature and air pressure at each inlet is estimated from a linear interpolation between sensors at the top of the tower (29m) and sensors at the bottom of the tower (7m). As I only measure a limited number of heights, this equation becomes, in practice:

$$F_{CS} = \left(\frac{\Delta C}{\Delta t}\right)_{k=1} \times z_{k=1} + \sum_{k=2}^{n}\left\{\left[\left(\frac{\Delta C}{\Delta t}\right)_k + \left(\frac{\Delta C}{\Delta t}\right)_{k-1}\right] \times \frac{z_k - z_{k-1}}{2}\right\} \tag{2.3}$$

where C is CO_2 (µmol m^{-3}) and t is time (s) ($\Delta C/\Delta t$ is the variation of C over 30 minutes), z is the height (m), k [1 to n = 8] represents each inlet. I flagged and replaced the storage flux with a one-point approximation during profiler outages (25% of the 4-year record), using the

change in CO_2 at 29 m height over 30 minutes as derived in EddyPro (Aubinet et al. 2001). These data were not used for empirical relationships, but kept for annual sum calculations. Storage flux of water vapour was assumed to be negligible. For visualisation of the diurnal course of storage flux and turbulent flux, see Figure S2. 4.

2.3.6 Gap-filling of environmental variables and NEE separation into gross fluxes

I used the PyFluxPro software for gap-filling climatic variables and fluxes, and for partitioning the NEE into gross primary productivity (GPP) and ecosystem respiration (R_{eco}) (Isaac et al. 2017). I only used observational data that passed the steady state and developed turbulence tests for gap-filling and for partitioning (QC flags of 0 and 1; (Foken et al. 2004)). In brief, gaps in climate variables were filled following the hierarchy of using variables provided from 1) automatic weather stations from the closest weather station, 2) numerical weather prediction model outputs (ACCESS regional, 12.5 km grid size provided by the Bureau of Meteorology) and lastly 3) monthly mean values from the site-specific climatology. In a next step the continuous climate variables were used to fill all fluxes by utilizing the embedded SOLO neural network with 25 nodes and 500 iterations on monthly windows. I used 'Random Forest' (Breiman 2001) to determine and rank potential explanatory variables for explaining latent heat flux (λE), sensible heat flux (H) and NEE. I then selected the five variables with the highest feature importance for each flux and compared the gap-filling performance of the neural network for each flux with the performance based on an educated guess of potential relevant drivers. I selected the variable array with the highest Pearson correlation coefficient and lowest root mean square error (RMSE) for gap-filling in PyFluxPro, which identified net radiation (R_n), soil water content (SWC), soil temperature (T_s), wind speed (w_s) and vapor pressure deficit (D) for λE (r = 0.93, RMSE = 32.0); down-welling shortwave radiation (F_{sd}), air temperature (T_a), T_s, w_s , SWC and D for H (r = 0.97, RMSE = 23.1) and F_{sd}, D, T_a, T_s and SWC for NEE (r = 0.87, RMSE =

4.04). To gap-fill R_{eco}, all nocturnal observational data (at night, I assume GPP = 0 so NEE = R_{eco}) that passed all quality control checks and the u*-filter were modelled using T_s, T_a and SWC as drivers in SOLO on the full dataset with 10 nodes and 500 iterations. Lastly, this gap-filled R_{eco} was used to infer GPP as the result of NEE – R_{eco}.

2.3.7 Flux footprint

I analysed the footprint climatology of AU-Cum site according to (Kormann and Meixner 2001), using the R-Package "FREddyPro' (Figure S2. 5). I assumed that the ecosystem within the footprint was homogeneous for the purpose of this study.

2.3.8 Energy balance

I evaluated the energy balance closure with the ratio of available energy (R_n – soil heat flux (G)) to the sum of turbulent heat fluxes (λE + H). On a daily basis, the energy balance closure was 70% (Figure S2. 6), consistent with the well-known and common issue of a lack of closure (Wilson et al. 2002, Foken et al. 2006, Foken 2008). I did not use the criteria that closure had to be met for the reported fluxes.

2.3.9 Surface conductance

Surface conductance (G_s) was derived by inverting the Penman-Monteith equation (Monteith 1965):

$$G_s = \frac{\gamma\, \lambda E\, g_a}{\Delta\, R_n + \rho\, C_p\, D\, g_a - \lambda E\, (\Delta + \gamma)} \tag{2.4}$$

where γ is the temperature dependent psychrometric constant (kPa K^{-1}), λE is the latent heat flux (W m^{-2}), Δ is the temperature dependent slope of the saturation-vapor pressure curve (kPa K^{-1}), R_n is the net radiation (W m^{-2}), ρ is the air density (kg m^{-3}), D is the vapor pressure deficit (kPa), C_p is the specific heat of air (J kg^{-1} K^{-1}), and g_a is the bulk aerodynamic

conductance, formulated as an empirical relation of mean horizontal wind speed (U, m s^{-1}) and friction velocity (u_*, m s^{-1}) (Thom 1972):

$$g_a = \frac{1}{\frac{U}{u_*^2} + 6.2\, u_*^{-0.67}} \tag{2.5}$$

In the analysis for G_s, I was interested in transpiration (T) rather than evaporation (E), so I excluded data if precipitation exceeded 1 mm in the past 2 days, 0.5 mm in the past 24 hours, and 0.2 mm in the past 12 hours (Knauer et al. 2015). I assumed that evaporation (E) is negligible using these criteria (Knauer et al. 2017), which excluded 40% of the data.

2.3.10 Dynamics of canopy phenology (leaf area index, litter and leaf production) and photosynthetic capacity

I evaluated the dynamics of canopy leaf area index (LAI) by measuring canopy light transmittance with three under-canopy PPFD sensors and one above canopy PPFD sensor LI190SB (LI-COR Inc., Lincoln NE, USA) following the methods presented in (Duursma et al. 2016). Although I use the term LAI, this estimate does include non-leaf surface area (stems, branches). I collected litterfall (L_f, g m^2 $month^{-1}$) in the tower footprint approximately once per month, from nine litter traps (0.14 m^{-2} ground area) located near the understory PPFD sensors. I estimated specific leaf area (SLA) of eucalyptus and mistletoe leaves by sampling approximately 50 fresh leaves of each, in June 2017 (SLA = 56.4 cm^2 g^{-1} for eucalyptus, 40.3 cm^2 g^{-1} for mistletoe). For each month, I partitioned the litter into eucalyptus leaves, mistletoe leaves, and other (mostly woody) components. I used this SLA to estimate leaf litter production (L_p) in m^2 m^{-2} $month^{-1}$ of eucalyptus, mistletoe, and total as the sum of both. Then, I estimated leaf growth (L_g, m^2 $month^{-2}$) as the sum of the net change in LAI (ΔL) and L_p. Photosynthetic capacity (PC) is defined as median GPP when PPFD is 800-1200 μmol m^{-2} s^{-1} and D is 1.0 to 1.5 kPa.

2.3.11 Analysis of light-response of NEE

I evaluated the light response of NEE using a saturating exponential function (Eq. 2.6) to test whether parameters varied between seasons (Mitscherlich 1909, Aubinet et al. 2001, Lindroth et al. 2008).

$$\mathrm{NEE} = -(\mathrm{NEE_{sat}} + \mathrm{R_d})\left(1 - \exp\left[\frac{-\alpha\ \mathrm{PPFD}}{\mathrm{NEE_{sat}} + \mathrm{R_d}}\right]\right) + \mathrm{R_d} \tag{2.6}$$

where the parameter R_d is the intercept, or NEE in the absence of light, often called dark respiration; NEE_{sat} is NEE at light saturation and α is the initial slope of the curve, expressed in µmol CO_2 µmol photon^{-1} and representing light use efficiency when photosynthetic photon flux density (PPFD) is close to 0. I only used daytime quality checked NEE data to fit the model (qc = 0; (Foken et al. 2004), LI-7500 signal strength = max, all inlets of profiler system data available and $u_* > 0.2$ m s^{-1}), see Figure S2. 7.

2.3.12 Leaf gas exchange spot measurements

I used previously published data of spot leaf gas exchange measurements in a nearby site for comparison with ecosystem values (Gimeno et al. 2016).

2.3.13 Remotely sensed land surface greenness

Normalized difference vegetation index (NDVI) and Enhanced Vegetation Index (EVI) values were derived from the MODIS Terra Vegetation Indices 16-Day L3 Global 250m product (MOD13Q1), which uses atmospherically corrected surface reflectance masked for water, clouds, heavy aerosols, and cloud shadows (Didan 2015a). At 250 m spatial resolution, the pixel containing Cumberland Plain was assumed to be representative for the footprint and values of that pixel between 1.1.2014 and 31.12.2017 were extracted.

2.4 Results

2.4.1 Seasonality of environmental drivers and leaf area index

Climatic conditions were favourable for growth at the site year-round. The monthly average of daily maximum air temperature was 16.3 °C during the coldest month (July 2015), and the lowest monthly average of daily maximum PPFD was 878 µmol m^{-2} s^{-1} in the winter (June 2015; Figure 2.1c). Although less rainfall occurred during winter months compared to summer months, precipitation occurred throughout the year (Figure 2.1b). Soil volumetric water content (SWC) in the shallow (0-8 cm) layer was about 10% except immediately following rain events (Figure 2.1b). In contrast, SWC in the clay layer (8 -38 cm) remained above 30% for the duration of the study (data not shown). Monthly average of daily maximum air temperature ranged from 16.3 °C in July 2015 to 32.7 °C in January 2017; monthly average of daily maximum D ranged from 0.9 kPa in June 2015 to 3.4 kPa in January 2017 (Figure 2.1c). For visualisation of seasonal and diurnal trends of radiation, air temperature, D and SWC, see supplement Figure S2. 8.

Canopy leaf area index varied between 0.7 (in December 2014) and 1.15 m^2 m^{-2} (in March 2016 and June 2017) (Figure 2.1d). LAI followed a distinct pattern: it peaked in late summer (around February), and then continuously decreased until the new leaves emerged the following year. A late leaf flush was observed in 2017 (May). Litter production also peaked in summer, before and during the leaf flush, and was lower in winter (Figure 2.1d). EVI followed the time dynamic of LAI.

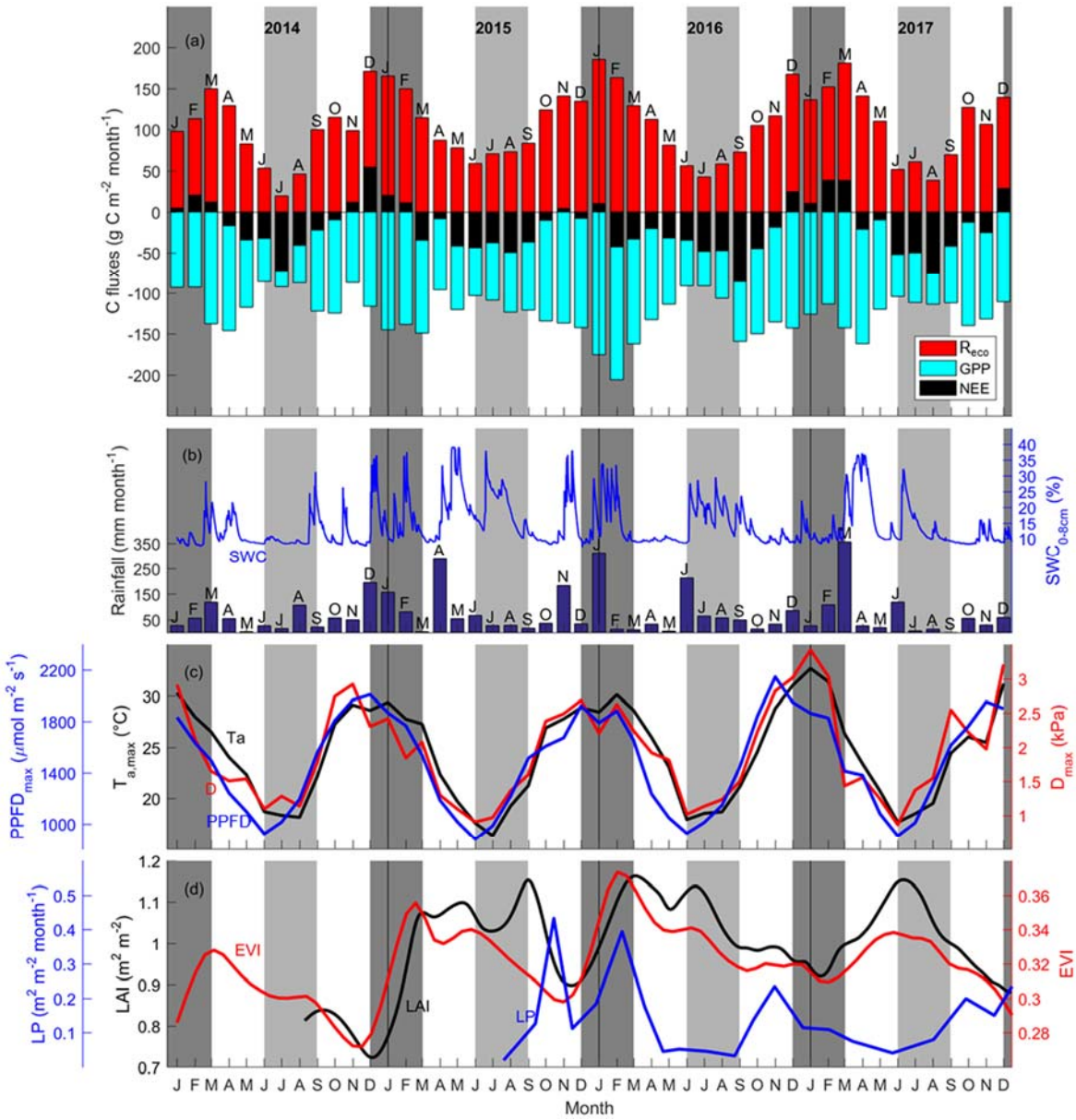

Figure 2.1 Time series of fluxes and weather a) Time series of monthly carbon flux (net ecosystem exchange (NEE), ecosystem respiration (R_{eco}) and gross primary productivity (GPP), g C m^{-2} $month^{-1}$) (negative indicates ecosystem uptake); b) rainfall, mm $month^{-1}$; soil water content from 0 to 8 cm (SWC0-8cm, %); c) average of daily maximum for each month photosynthetically active radiation (PPFDmax, µmol m^{-2} s^{-1}), air temperature (Ta_{max} , °C) and vapour pressure deficit (Dmax, kPa). D) Canopy dynamics trends: enhanced vegetation index (EVI, unitless); leaf area index (LAI, m^2 m^{-2}) and litter production (LP, m^2 m^{-2} $month^{-1}$). Shaded areas shows summer (dark grey) and winter (light grey). Note Ta_{max} and $PPFD_{max}$ remained above 15 °C and 800 µmol m^{-2} s^{-1}.

2.4.2 Seasonality of carbon and water fluxes

Contrary to expectations, the ecosystem was always a sink for carbon in winter (-146 g C m^{-2} on average, with a standard deviation of 22 g C m^{-2}), and usually a carbon source or close to neutral in summer (+ 44 g C m^{-2} on average, with a standard deviation of 43 g C m^{-2}) (Table 2.1). On average, summer GPP was lower – i.e. more uptake (-400 ± 97 g C m^{-2}) compared to winter GPP (-282 ± 41 g C m^{-2}) (Table 2.1), that is a difference of ~ 118 g C m^{-2}. However, average summer R_{eco} was much higher (444 ± 56 g C m^{-2}) compared to winter R_{eco} (159 ± 35 g C m^{-2}) (Table 2.1), a difference of ~ 285 g C m^{-2}. The summer vs. winter R_{eco} difference was more than double the GPP difference; thus, R_{eco} had a relatively larger effect over the seasonality of NEE.

2.4.3 Diurnal trend of CO_2 flux and drivers in winter and summer

The diurnal pattern of NEE in clear-sky conditions differed between summer and winter (Figure 2.2). Relatively speaking, diurnal NEE was more symmetric in the winter than in summer. That is, morning and afternoon NEE pattern resembled a mirror image and total integrated morning NEE was similar to integrated afternoon NEE during the winter, but strong hysteresis occurred in the summer (Figure 2.2). This pattern also translated into hysteresis in the NEE light response curve in summer, but to a lesser degree in winter (Figure 2.3).

Table 2.1 Annual fluxes and weather over the 2014-2017 period. Precipitation (P, mm y^{-1}), evapotranspiration (ET, mm y^{-1}), air temperature T_a (°C), net ecosystem exchange (NEE, g C m^{-2} y^{-1}), gross ecosystem production (GPP, g C m^{-2} y^{-1}) and ecosystem respiration (R_{eco}, g C m^{-2} y^{-1}) for the four year study period.

Period	P (mm y^{-1})	ET (mm y^{-1})	T_a (°C)	NEE (g C m^{-2} y^{-1})	GPP (g C m^{-2} y^{-1})	R_{eco} (g C m^{-2} y^{-1})
2014 all	**733**	**797**	**18**	**-124**	**-1301**	**1177**
Winter	149	142	13	-145	-265	120
Spring	129	189	19	-20	-333	313
Summer	279	275	23	80	-302	382
Autumn	176	190	19	-39	-401	362
2015 all	**978**	**938**	**18**	**-234**	**-1517**	**1283**
Winter	122	160	12	-131	-335	204
Spring	237	223	19	-43	-392	349
Summer	273	318	23	24	-426	449
Autumn	345	238	18	-84	-365	280
2016 all	**893**	**852**	**19**	**-372**	**-1664**	**1292**
Winter	335	164	13	-130	-288	158
Spring	96	207	19	-149	-444	295
Summer	412	311	24	-8	-524	516
Autumn	50	171	20	-85	-408	323
2017 all	**821**	**798**	**19**	**-171**	**-1486**	**1315**
Winter	139	148	13	-177	-329	152
Spring	85	178	19	-80	-383	303
Summer	194	236	25	78	-350	428
Autumn	403	237	18	8	-424	432

2.4.4 Analysis of NEE light response curve

The parameters of the NEE light response in summer and winter are shown in Figure 2.4 (see methods, Eq. 5). The initial slope of NEE with light (α) showed no clear dependence on T_{soil} in winter but exhibited sensitivity during summer, dropping precipitously at soil temperature above 23 °C (Figure 2.4a). α increased with SWC in winter and summer by a factor of 1.5 (Figure 2.4b). In both winter and summer α decreased with D (D > 1 kPa) and in a similar fashion, approaching a saturating value of 0.01 (µmol μmol^{-1}) at a D of about 2 kPa (Figure 2.4c). The fitted NEE at saturating light (NEE_{sat}) was not related to T_{soil} in winter but decreased with increasing T_{soil} in summer (Figure 2.4d). NEE_{sat} was higher in winter than in summer for a given SWC. The relationship with D was more complicated, tending to increase

with D in winter, but decreasing with increased D in summer, dropping from 9 to 3 (µmol m^{-2} s^{-1}) as D increased from 1 to 4 kPa. R_d was significantly higher in summer than winter across all conditions of T_{soil}, SWC and D (Figure 2.4g-h-i). R_d increased with T_{soil} in winter and less so in summer. In winter, R_d increased up to SWC of 11%; in summer, R_d was more sensitive to SWC, doubling from a rate of ~ 4 to ~ 8 µmol m^{-2} s^{-1} as SWC increased from about 8 to 20%.

2.4.5 Atmospheric demand (D) and soil drought control on GPP, ET, G_s and WUE

I evaluated the effect of SWC and vapour pressure deficit (D) on GPP, ET, water use efficiency (WUE) and surface conductance (G_s) under high radiation ("light-saturated"; PPFD > 1000 µmol m^{-2} s^{-1}), after filtering periods following rain events in order to minimise the contribution of evaporation to ET (see Methods) (Figure 2.5). In summer, light-saturated GPP decreased above D ~ 1.3 kPa, but in winter, GPP did not vary with D. In summer and in winter, GPP increased with SWC (Figure 2.5a). This is consistent with Figure 2.4, where R_d and NEE_{sat} both increased with SWC. In summer, light-saturated ET increased with D up to ~1.3 kPa, above which it reached a plateau. In winter, ET kept increasing with D, as D rarely exceeded 2 kPa. In both seasons, ET increased with SWC (Figure 2.5b). Surface conductance decreased with D and SWC especially in summer, indicating strong stomatal regulation (Figure 2.5d). WUE decreased with increasing D in summer and in winter, because ET increased but -GPP declined (Figure 2.5c).

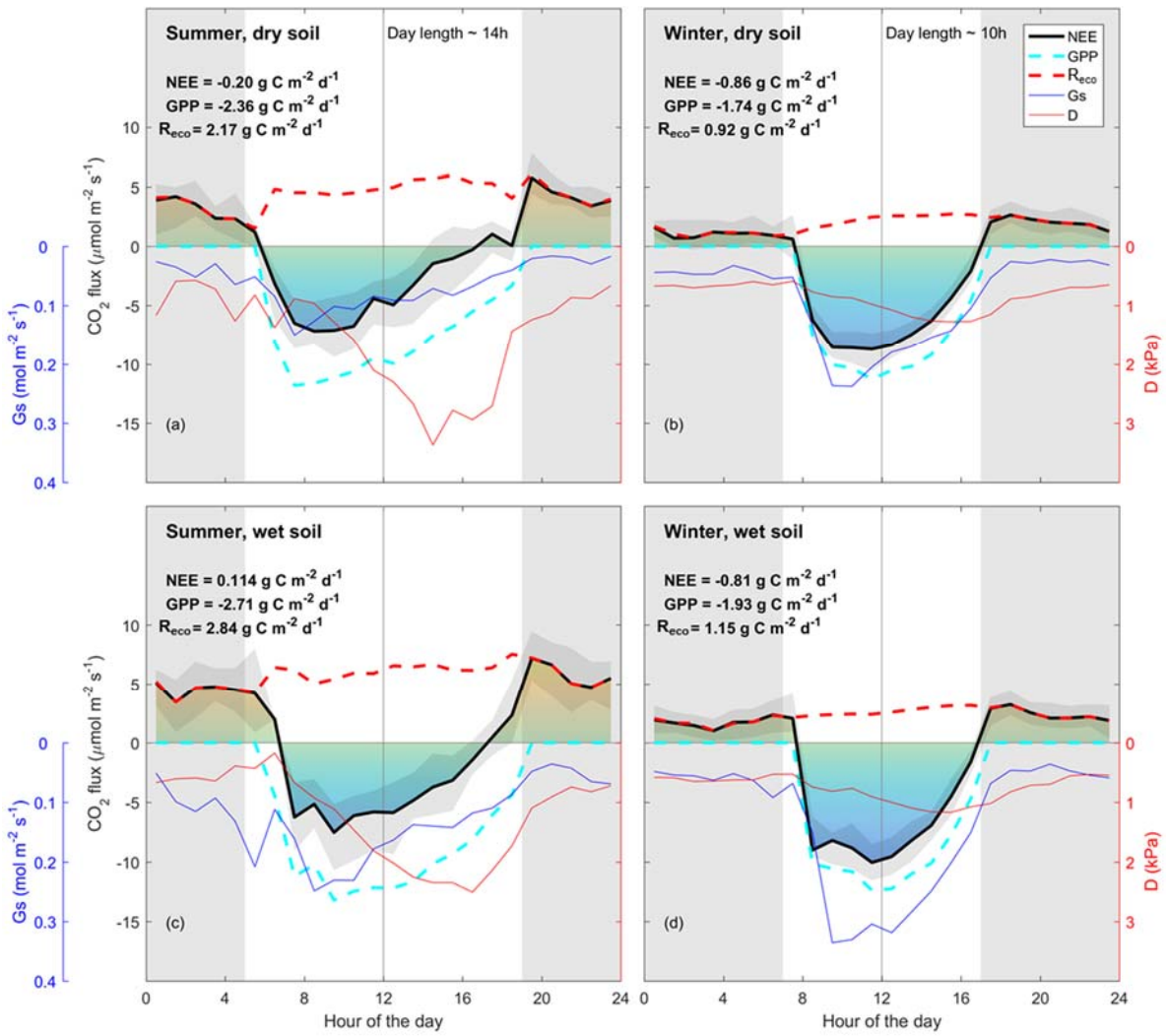

Figure 2.2 Diurnal trend of fluxes, surface conductance and vapour pressure deficit. line: median and shade: quartile of clear-sky measured net ecosystem exchange (NEE, thick black line, µmol m^{-2} s^{-1}); estimated daytime ecosystem respiration (R_{eco}, inferred from a neural network fitted on nighttime NEE, thick dotted red line, µmol m^{-2} s^{-1}); estimated gross primary productivity (GPP, inferred as NEE – estimated daytime R_{eco}, thick dotted cyan line, µmol m^{-2} s^{-1}); measured vapour pressure deficit (D, thin red line, kPa); and estimated surface conductance (G_s, inferred from Penman-Monteith, blue line, mmol m^{-2} s^{-1}). Grey shade shows night-time (sunset to sunrise). NEE, GPP and R_{eco} are calculated by integrating the diurnal fluxes as shown in the figure. "Wet" and "dry" soil is defined as below or above the median of soil water content during summer or winter. Summer is December through February. Winter is June through August, as defined by the Sydney bureau of meteorology. Colours under NEE line are shown for visualisation. Note that there is an asymmetry between morning and afternoon NEE in summer, less so in winter. Note that ecosystem respiration (nighttime NEE) is enhanced by SWC in summer, less so in winter. Data used in this figure correspond to clear-sky half-hour values, where high quality measured data for NEE were available.

I compared these ecosystem-scale results to the equivalent at the leaf-scale, which are net photosynthesis at light saturation A_{max} (PPFD ~ 1800 µmol m^{-2} s^{-1}), leaf transpiration T, leaf water use efficiency, and stomatal conductance g_s (Figure 2.5, black lines). These leaf level measurements are expressed on a leaf-area basis, as compared to ground area for ecosystem scale. I observed that A_{max}, T and g_s were more sensitive to D than corresponding ecosystem-scale responses. A_{max} was much higher than GPP_{max} at D ~ 1 kPa, while g_s was comparable in magnitude to G_s in the same condition. Leaf transpiration peaked around D = 1.2 kPa, while ET plateaued. Leaf water use efficiency was overall higher than ecosystem WUE.

2.4.6 Canopy phenology control of GPP

Monthly average photosynthetic capacity (PC) varied by a factor of ~2 across the study period, ranging from 8.4 µmol m^{-2} s^{-1} before the leaf flush in November 2014 to 15 µmol m^{-2} s^{-1} after the leaf flush occurred in March 2016. I expected that PC could be predicted by LAI, EVI and G_s. Leaf area index (LAI) and photosynthetic capacity (PC) were significantly correlated; the slope was significantly different from zero ($r^2 = 0.29$, $p < 0.005$, PC = 8.3 LAI + 3.0, Figure 2.6). EVI was even more significantly correlated with PC ($r^2 = 0.46$, $p < 0.005$, PC = 52 EVI – 5.3, **Error! Reference source not found.**). $G_{s,max}$ was significantly correlated with PC ($r^2 = 0.2$, $p < 0.005$, PC = 9 $G_{s,max}$ + 9) and LAI ($r^2 = 0.30$, $p < 0.005$, $G_{s,max}$ = 0.45 LAI – 0.18) and with EVI ($r^2 = 0.29$, $p < 0.005$, $G_{s,max}$ = 2.3 EVI – 0.45). The correlations with NDVI were less significant than with EVI (see Figure S2. 9).

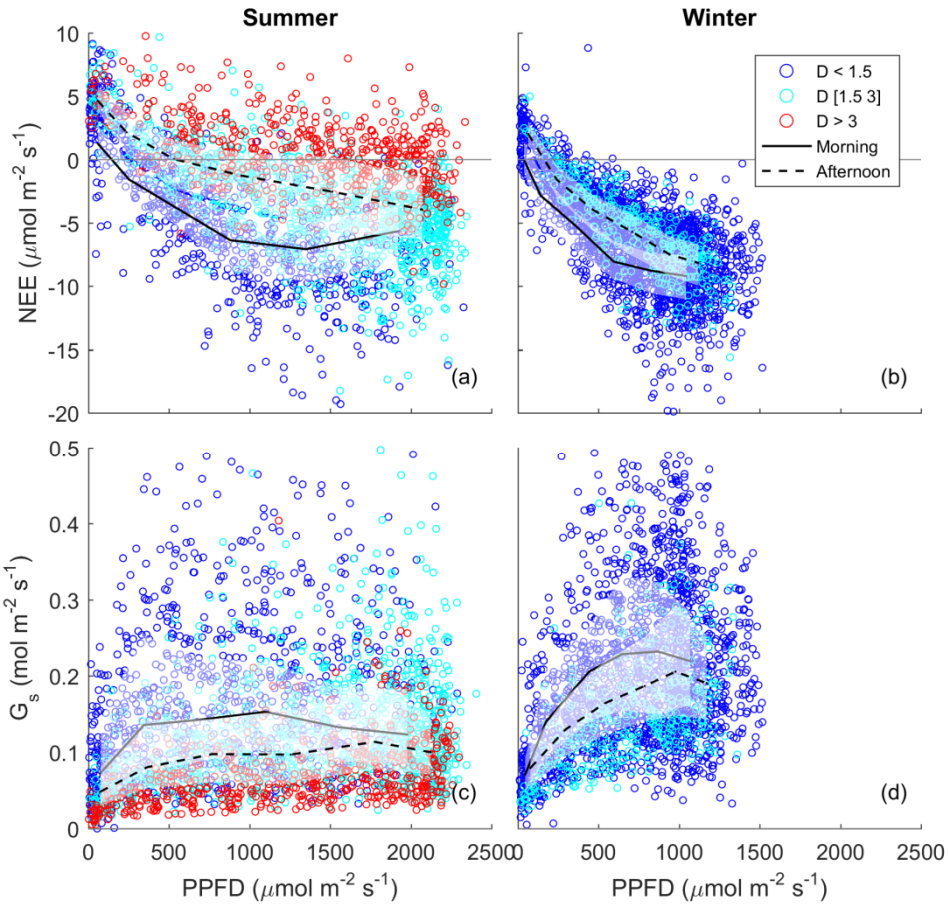

Figure 2.3 Half-hourly measured NEE vs. PPFD, coloured by D (blue, D < 1.5 kPa, cyan: D [1.5-3] kPa, red: D > 3 kPa) for (a) summer, and (b) winter periods. Raw data are binned by light levels to show median (lines) and quartiles (white shades) for morning (continuous lines) and afternoon (dotted lines) hours separately.

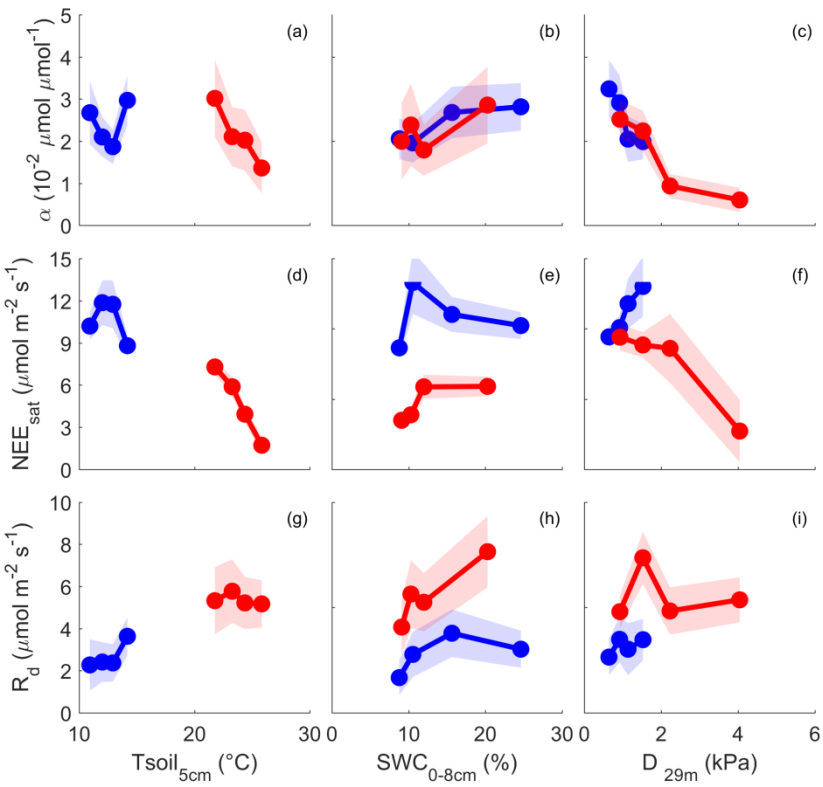

Figure 2.4 NEE µmol m^{-2} s^{-1} light response parameters, calculated for different bins of climatic drivers (soil temperature (T_{soil}, °C) at 5cm depth, soil water content (SWC, %) from 0 cm to 8 cm depth, and atmospheric demand (D, kPa) at 29 m height), only raw, qc filtered daytime data are used. Light response curve was fitted using Mitscherlich equation (see methods), α is the initial slope, near PPFD = 0 (µmol $µmol^{-1}$), NEE_{sat} µmol m^{-2} s^{-1} is NEE at light saturation, and R_d µmol m^{-2} s^{-1} is the dark respiration (NEE when PPFD = 0). Blue indicates winter months, Red indicates summer months. Dots are parameters value for each quartile of driver, plotted at x = median of driver for each bin. Shading is 95% confidence interval of the parameter fit.

2.5 Discussion

I measured four consecutive years of carbon, water and energy fluxes in a native evergreen broadleaf eucalyptus forest, including canopy dynamics and environmental drivers (photosynthetically active radiation, air and soil temperature, precipitation, soil water content, and atmospheric demand). I hypothesised that the Cumberland Plain forest would be a carbon sink all year-round, similar to other eucalypt forests (Keith et al. 2012, Beringer et al. 2016, Hinko-Najera et al. 2017a). I also hypothesised higher net carbon uptake during summer, due to warmer temperatures, higher light and longer day length contributing to higher photosynthesis, compared to winter. However, the site was a net source of carbon during summer, and a net sink of carbon during winter.

The seasonal pattern of NEE was driven mostly by R_{eco}, as the seasonal amplitude of R_{eco} was larger than the seasonal amplitude of GPP. The seasonality of R_{eco} may be explained by the positive effects of higher temperatures on the rates of autotrophic respiration (Tjoelker et al. 2001), and on the activity of microbes to increase soil organic matter decomposition (Lloyd and Taylor 1994); low soil moisture in the shallow layers sometimes limited decomposition (January and February 2014, January and December 2015, February and December 2017, see Figure 2.1), but often regular rainfall maintained adequate soil moisture. The relatively low seasonality of GPP may be partly explained by lower photosynthetic capacity in early summer (before January) when LAI was at its lowest, and the leaves have reached maximum age because new leaves have not yet emerged. The R_{eco}-driven seasonality of NEE is in sharp contrast with cold temperate forests where GPP drives the seasonality of NEE. R_{eco}-driven NEE seasonality was also observed in an Asian tropical rain forest, as R_{eco} was higher than GPP in the rainy season leading to net ecosystem carbon loss, while in the dry season, ecosystem carbon uptake was positive (Zhang et al. 2010). This pattern was also observed in an Amazon tropical forest (Saleska et al. 2003).

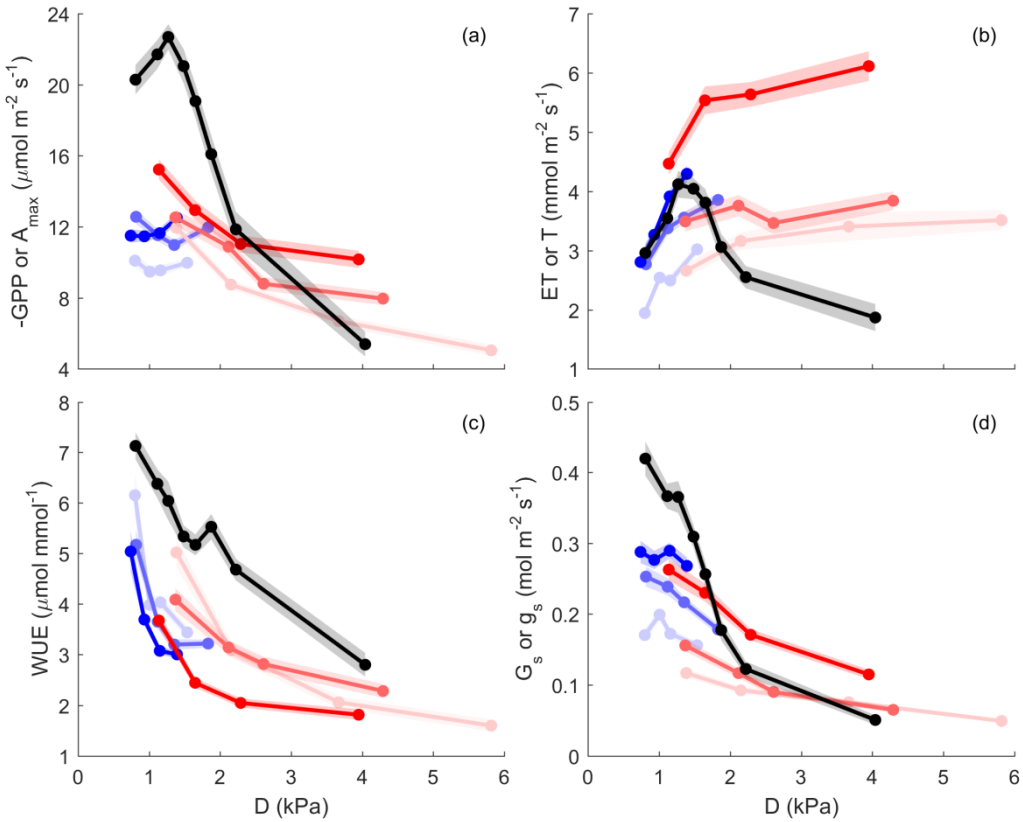

Figure 2.5 Light saturated GPP or A_{max}, ET or T, WUE, G_s or g_s responses to D and SWC. Gross primary productivity or net assimilation (GPP or Amax, µmol m^{-2} [ground or leaf] s^{-1}), evapotranspiration or leaf transpiration (ET or T, mmol m^{-2} [ground or leaf] s^{-1}), water use efficiency (WUE = GPP/ET or A_{max}/T, µmol mmol^{-1}) and surface conductance or leaf conductance (G_s or g_s, mmol m^{-2} s^{-1}) vs. vapour pressure deficit (D). Leaf level is shown in black, ecosystem scale is shown in color; summer (red) and winter (blue), at saturated PPFD (>1000 µmol m^{-2} s^{-1}). D is binned into 4 quartiles for ecosystem and 8 for leaf; Y is mean value for each D bins, plotted at the median of D bin. Shaded area indicates the standard error of the mean. The three color intensity show SWC quantiles (SWC < 0.33, SWC [0.33-0.67] and SWC [0.67-1.00] More intense the colour the higher the SWC).

A strong morning-afternoon hysteresis of NEE response to PPFD occurred in summer, and less so in winter (Figure 2.3). In winter, low D and moderately warm daytime air temperatures and high PPFD were sufficient to maintain high photosynthesis rates throughout most of the day (Figure 2.1). In summer, two possible explanations of the diurnal hysteresis of NEE are (1) R_{eco} is greater in the afternoon compared to morning or (2) GPP is lower in the afternoon compared to morning. Explanation (1) is plausible, as temperature drives autotrophic and heterotrophic respiration; however, it is unlikely to explain the hysteresis magnitude which is higher in summer compared to winter. Explanation (2) could arise from lower afternoon stomatal conductance or lower photosynthetic capacity (e.g. the maximum rate of carboxylation (Vcmax) decreases at high T_a), or a combination of both or even circadian regulation (Jones et al. 1998, Resco de Dios et al. 2015). An analysis of surface conductance showed strong stomatal regulation (Figure 2.2, Figure 2.3, Figure 2.5), induced by high atmospheric demand and high air temperature (Duursma et al. 2014), limiting photosynthesis during the afternoon of warm months (see Figure S2. 10). These diurnal patterns of NEE, GPP and R_{eco} play a strong role in regulating the seasonal carbon cycling dynamics in this ecosystem. A wavelet coherence analysis between D and GPP showed strong coherence at seasonal time scale (periods of three months), see Figure S2. 11.

I observed comparable responses of leaf-level and ecosystem-level gas exchange to environmental drivers (Figure 2.5). The larger magnitude of A_{max} than GPP at high D may be explained by the proportion of shaded leaves in the ecosystem. The similar magnitude for G_s and g_s was also expected, as LAI is close to 1 and R_n is not a driver for stomatal conductance. The peaked pattern of T versus D, as opposite to saturating pattern of ET, may be explained by (1) the contribution of soil evaporation to ET or (2) the presence of mistletoe, known for not regulating their stomata (Griebel et al. 2017). The higher magnitude of leaf water use

efficiency results from the combination of higher A_{max} and similar or lower leaf transpiration compared to ET. Furthermore, I compared leaf level g_1 and ecosystem level G_1, using the optimal stomatal conductance model (Medlyn et al. 2011): G_1 was lower than g_1 (1.6 ± 0.06 for G_1, 4.4 ± 0.2 for g_1, see Figure S2. 12).

Our study demonstrated that canopy dynamics (specifically, LAI in our study) play an important role in regulating seasonal variations in GPP even in evergreen forests. Similar observations emerged from a tropical forest, where leaf area index and leaf age explained the seasonal variability of GPP (Wilson et al. 2001, Wu et al. 2016b), as the photosynthetic capacity (PC, the maximum rate of GPP in optimal environmental condition) varied with leaf age. In Australian woodlands, PC (A_{max}) of leaves was also found to decrease with leaf age: A_{max} declined by 30% on average between young and old leaves, for 10 different species (Reich et al. 2009). In the Cumberland Plain forest, periods with high LAI co-occur with mature, efficient leaves, and periods with low LAI co-occur with old, less efficient leaves. LAI was correlated with PC, which was probably the result of both a greater number of leaves and more efficient leaves. Remotely sensed vegetation indices such as EVI or NDVI assess whether the target being observed contains live green vegetation. In Australia, NDVI and EVI were good predictors of photosynthetic capacity in savanna, mulga and Mediterranean-mallee ecosystems (Restrepo-Coupe et al. 2016). For our site, EVI was a good predictor of PC, which was surprising as satellite-derived LAI values have been found to be typically inaccurate in open forests and forests in southeast Australia (Hill et al. 2006). NDVI was a poor predictor of PC (see Figure S2. 9).

In a global study, it was shown that mean annual NEE decreased with increasing dryness index (PET/P) in sites located below 45° N latitude (Yi et al. 2010). It has also been shown that *Eucalyptus* grow more slowly in warm environments (Prior and Bowman 2014). At our site, and in a previous study in eucalyptus forest (van Gorsel et al. 2013), GPP decreased with

D above a threshold of ~ 1.3 kPa. Our results indicate that surface conductance (G_s) decreased above that threshold, suggesting that the decrease in GPP is caused by stomatal regulation. As D correlates with air temperature, it is difficult to distinguish the relative contribution of D and T_a to the decrease of G_s, but they are thought to both impact G_s (Duursma et al. 2014). Cumberland Plain has the highest mean annual temperature and the highest dryness index among the four eucalyptus forest eddy-covariance sites in south-east Australia (Beringer et al. 2016), which could explain its strong sensitivity to D and hence its unique seasonality.

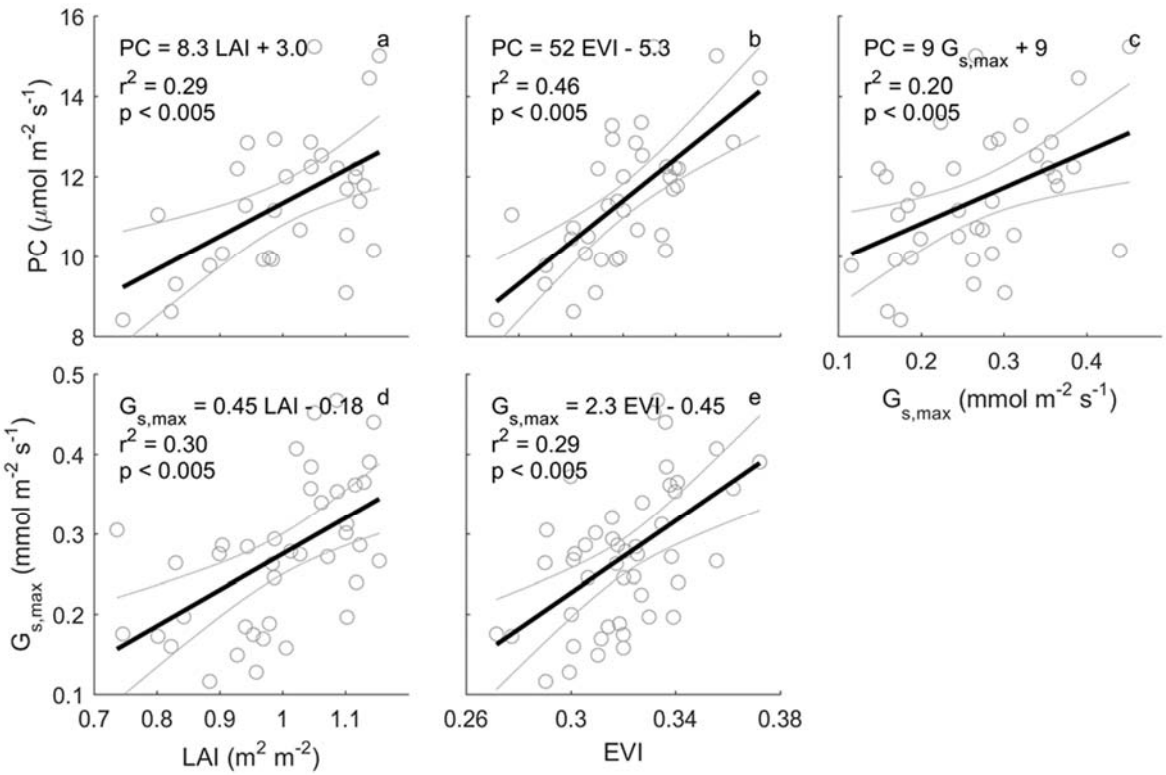

Figure 2.6 Photosynthetic capacity and surface conductance response to leaf area index and enhanced vegetation index. Relationships between monthly photosynthetic capacity (PC, µmol m^{-2} s^{-1}), leaf area index (LAI, m^2 m^{-2}), enhanced vegetation index (EVI), and maximum surface conductance ($G_{s,max}$). Monthly PC and monthly $G_{s,max}$ are calculated as the median of half-hourly GPP and half-hourly G_s when PPFD [800-1200 µmol m^{-2} s^{-1}] and D [1-1.5 kPa]; rain events are filtered for $G_{s,max}$ estimation, to minimise evaporation contribution to evapotranspiration (see methods). Monthly LAI is calculated as mean of LAI smoothed by a spline. Thick black line shows a linear regression. For PC calculation, GPP data is only used when quality-checked NEE is available (GPP = NEE measured – R_{eco} estimated by a neural network, see method).

2.6 Conclusions

The Cumberland Plain forest was a net C source in summer and a net C sink in winter, in contrast to other Australian eucalypt forests which were net C sinks year-round. R_{eco} drove NEE seasonality, as the seasonal amplitude of R_{eco} was greater than GPP. R_{eco} was high in the warmer, wetter months of summer, when environmental conditions supported high autotrophic respiration and heterotrophic decomposition. Meanwhile, GPP was limited by lower LAI and probably older leaves in early summer, and by high D which limited G_s throughout the summer. Despite being evergreen, there was significant temporal variation in LAI, which was correlated with monthly photosynthetic capacity and monthly surface conductance. Understanding LAI dynamics and its response to precipitation regimes will play a key-role in climate change feedback.

3 Chapter 3. Phenology of canopy dynamics and carbon fluxes in a temperate evergreen broadleaved forest: a data-model comparison

3.1 Abstract

Forest carbon and water exchange with the atmosphere is regulated by forest structure as well as climate. Forest structure can vary seasonally and inter-annually in evergreen as well as deciduous forests, but the importance of these variations for carbon and water fluxes in evergreen forests is poorly understood. In global land surface models, leaf area index (LAI) for evergreen forests is typically considered either to be seasonally constant or to vary in tune with net primary productivity (F_{NPP}). I analysed the phenology of LAI in a temperate evergreen eucalypt forest in Southeast Australia, where LAI varied seasonally from 1.2 to 1.5 m^2 m^{-2}, and from 1.1 to 1.6 m^2 m^{-2} inter-annually. I applied the Community Atmosphere Biosphere Land Exchange (CABLE) model to explore the importance of variable LAI for ecosystem carbon and water fluxes. I compared the seasonal and inter-annual amplitude of fluxes, and the timing of peak growth, between simulations where LAI was held constant, and simulations where LAI was forced by observations. I further estimated leaf growth from temporal variation in LAI and litter fall and inferred the time-course of allocation of net primary productivity (F_{NPP}) to leaf growth to improve understanding of carbon allocation dynamics. I found seasonal and interannual variability in LAI. The peak of LAI occurred in late summer-early autumn, with a higher peak occurring earlier in years when summer rainfall was greater. The CABLE model correctly reproduced the observed response of photosynthetic capacity to LAI only in the simulation using variable LAI. Surprisingly, variation in LAI dampened the seasonal amplitude of simulated gross ecosystem productivity (F_{GEP}) and net ecosystem productivity (F_{NEP}) but increased the inter-annual variability of simulated F_{GEP} and F_{NEP} (year to year variability of modelled F_{NEP} was 191 g C m^{-2} with

varying LAI, and 140 g C m^{-2} with constant LAI). Allocation of carbon to leaf growth was dynamic and peaked in summer. These results contribute to improved estimation of C uptake dynamics in response to seasonal and inter-annual variations in precipitation in temperate broadleaved evergreen forests.

3.2 Introduction

Forest functions, such as carbon, energy and water exchange with the atmosphere, are driven by both weather and stand structure (Keith et al. 2012). Understanding the interactions among forest canopy dynamics, carbon fluxes and weather will provide new insights that are required to improve land surface models for forecasting future changes in coupled climate – ecosystem behaviour.

In many temperate forests, especially deciduous ones, leaf area index (LAI) has a clear seasonal pattern, with a period of high LAI in the (summer) growing season, and a period of low LAI period in the (winter) dormant season. Deciduous canopy phenology has been studied extensively and shown to have been altered by recent climate change (White et al. 1999, Garonna et al. 2014, Reyes-Fox et al. 2014). For instance, growing season length is increasing with rising temperature (T_{air}) in temperate deciduous forests, playing a key role in interannual variability of carbon fluxes (Richardson et al. 2012, Tang et al. 2013). Lengthening of the growing season is also linked to enhanced seasonal exchange as observed in the amplitude of the seasonal cycle of CO_2 (Forkel et al. 2016). In evergreen forests, in contrast, LAI can be relatively stable with leaf demography playing the dominant role to explain the seasonality of carbon, water and energy exchange (Wu et al. 2016a, Restrepo-Coupe et al. 2017b, Wu et al. 2017). However, in the Amazon tropical forests, both variations in LAI and leaf physiology were important to explain the seasonal variability of photosynthetic capacity and F_{GEP} (Wu et al. 2016a).

In Australia, a particularly large interannual variability of terrestrial net carbon exchange and LAI is observed and linked to periods of high or low rainfall, partly explained by the El Niño / Southern Oscillation (ENSO) (Bastos et al. 2013). For instance, the Millennium Drought in the early 2000's was exacerbated by El Niño conditions in south-eastern Australia that led to one of the driest and warmest summers on record in 2003. However, ENSO cannot always

explain drought events in Australia, which may be more related to the Indian Ocean Dipole (Ummenhofer et al. 2009).

Spectral vegetation indices, such as MODIS (Moderate Resolution Imaging Spectroradiometer) normalized difference vegetation index (NDVI) or MODIS enhanced vegetation index (EVI), are indices of canopy cover and greenness. These indices have been shown to be correlated with the fraction of absorbed PAR, which is related to photosynthetic activity, and time integrated MODIS NDVI or EVI are therefore used as proxy of ecosystem functions. Examples of ecosystem functions correlated with MODIS NDVI or EVI at flux towers are F_{GEP} (Huete et al. 2008, Maeda et al. 2014), net ecosystem production (F_{NEP}) (Olofsson et al. 2007) and photosynthetic capacity (PC, the maximum productivity of a canopy, i.e. F_{GEP} in optimal weather condition) (Restrepo-Coupe et al. 2016). Observations of time-integrated MODIS EVI product, at spatial resolution of 500m, are useful because it represents much larger measurements areas than flux towers. At the global scale, EVI is a good predictor of F_{GEP} in cropland and deciduous (grassland) biomes, but is typically less so in evergreen forests where EVI varies less seasonally (Restrepo-Coupe et al. 2016, Shi et al. 2017). In Australia, where high variability in precipitation leads to strong variations in soil water availability, EVI was a good predictor of F_{GEP} and PC in monsoonal savannas and in a semi-arid mulga woodland. However, the strength of the correlation varies among sclerophyll forests. There was a poor correlation at the Tumbarumba forest (Restrepo-Coupe et al. 2016), but EVI was a good predictor of PC and LAI at Cumberland Plain woodland (Renchon et al. 2018).

The change in LAI over time is driven by the timing of leaf growth and litter fall. Leaf growth depends on net primary productivity (F_{NPP}) and allocation of carbon to leaves, while litter fall depends on leaf age and environmental stress (such as heat and drought stress, wind and insect attacks). Leaf abscission can be triggered by water stress in response to production

of abscisic acid (Pierce and Raschke 1980); increased leaf life span is linked to soil nutrient limitation (Reich et al. 1991)). The underlying mechanisms controlling allocation in forests are not well understood (De Kauwe et al. 2014, Zuidema et al. 2018), leading to large discrepancies in simulated LAI among LSMs (Walker et al. 2014, Medlyn et al. 2016). Currently, LSMs use empirical relationships, such as fixed coefficients or allometric relations, or optimisation theory, to determine carbon allocation to leaf growth (Franklin et al. 2012).

In this study, I focus on the seasonal and inter-annual variability of weather and LAI of an evergreen broadleaf forest in southeast Australia. The Cumberland Plain site is equipped with a flux tower that provides quasi-direct measurement of forest-atmosphere net exchange of CO_2, water and energy (Baldocchi et al. 1996, Baldocchi et al. 2001b, Isaac et al. 2017, Renchon et al. 2018). From 2014 to 2017, the temperate forest acted as a carbon sink in winter and a source in summer, seasonal PC was significantly correlated with LAI ($r^2 = 0.29$) and remotely sensed EVI ($r^2 = 0.46$), and carbon uptake was limited by high T_{air} and atmospheric demand (vapor pressure deficit) in summer but remained high in winter (Renchon et al. 2018). Ecosystem respiration drove the seasonal cycle of net carbon exchange, as its seasonal variation was more important than that of gross primary productivity. However, inter-annual variations in F_{NEP}, F_{GEP} and F_{ER} were not related to meteorological conditions, perhaps because the four-year record was too short, or because canopy dynamics obscured the climate effects on fluxes.

Our objectives are to quantify (1) seasonal and interannual variations in LAI and the dominant drivers of LAI variations, and (2) the contributions of seasonal and interannual variations in LAI and weather on gross and net CO_2 fluxes using the CABLE land surface model over the past 18 years. In CABLE-POP, LAI is assumed to be constant within a year in broadleaf evergreen forest (but vary year to year). Also, I use modelled F_{NPP} along with

measurements of LAI and litter fall to evaluate the seasonality of carbon allocation to leaf growth and the proportion of the canopy senescing over time.

Table 3.1 List of symbols and acronyms

Acronym	Short definition (see methods #)	Unit
EC	Eddy-covariance (3.3.1.5)	-
Cv	CABLE varying LAI_{EVI} (3.3.1.6)	-
Cc	CABLE constant LAI_{EVI} (3.3.1.6)	-
F_{NEP}	Net ecosystem production	Monthly or annual: (g C m^{-2}) Half-hourly: (µmol m^{-2} s^{-1})
F_{ET}	Evapotranspiration	Monthly or annual: (g C m^{-2}) Half-hourly: (µmol m^{-2} s^{-1})
F_{GEP}	Gross ecosystem productivity	Monthly or annual: (g C m^{-2}) Half-hourly: (µmol m^{-2} s^{-1})
F_{ER}	Ecosystem respiration	Monthly or annual: (g C m^{-2}) Half-hourly: (µmol m^{-2} s^{-1})
F_{NPP}	Net primary productivity	Monthly or annual: (g C m^{-2}) Half-hourly: (µmol m^{-2} s^{-1})
LAI_{EVI}	Leaf area index (3.3.1.3)	(m^2 m^{-2})
PC	Photosynthetic capacity	(µmol m^{-2} s^{-1})
F_{Lfall}	Litter fall (3.3.1.4)	(g C m^{-2})
$F_{Lgrowth}$	Leaf growth (3.3.1.4)	(g C m^{-2})
a_f	Allocation of NPP to leaves (3.3.3)	-
k_f	Canopy leaf turnover (3.3.3)	-
$G_{s,opt}$	Surface conductance	(mmol m^{-2} s^{-1})
F_{PPFD}	Photosynthetic Photon Flux Density (3.3.1.2)	(µmol m^{-2} s^{-1})
T_{air}	Air temperature (3.3.1.2)	(°C)
D	Vapour pressure deficit (3.3.1.2)	(kPa)
Precip	Precipitation (3.3.1.2)	(mm)
SWC	Soil water content (3.3.1.2)	(%)

3.3 Materials and methods

3.3.1 Site description, measurements and modelling

3.3.1.1 Site description

The Cumberland Plain site (AU-Cum in FLUXNET http://sites.fluxdata.org/AU-Cum/ and Ozflux http://www.ozflux.org.au/monitoringsites/cumberlandplain/index.html) located near Sydney, Australia, (latitude – 33.61518; longitude 150.72362) has a mean annual air temperature (T_{air}) of 18°C and mean annual precipitation of 800 mm yr^{-1}. The soil is classified as a Kandosol and consists of a fine sandy loam A horizon (0–8 cm) over clay to clay loam subsoil (8–40 cm), with pH of 5 to 6 and up to 5% organic C in the top 10 cm (Karan et al. 2016). The dry-sclerophyll forest is dominated by *Eucalyptus moluccana* and *E. fibrosa*, both commonly infected by mistletoe (*Amyema miquelii*); the forest also has a mid-canopy stratum of *Melaleuca decora*, a shrub layer dominated by *Bursaria spinosa*, and a sparse understory composed of forbs, grasses and ferns. The canopy height is ~ 24 m, with individual taller trees (airborne lidar survey, November 2015). A 30-m tall flux tower, with instruments at 29 m height, was installed near the geographical centre of the remnant Cumberland Plain woodland.

3.3.1.2 Meteorological and remote sensing data

Environmental conditions were measured on site from 2014 to 2017. The detail of the methods can be found in (Renchon et al. 2018). In brief, meteorological data were logged every 30 minutes to match the time step of the tower flux data, including T_{air} and relative humidity (HMP155A, Vaisala, Vantaa, Finland sensors at 29m), photosynthetic photon flux density (F_{PPFD}, LI190SB, LI-COR Inc., Lincoln, NE, USA), incoming and outgoing shortwave and longwave radiation (CNR4 radiometer, Kipp & Zonen, Delft, the Netherlands). Rainfall was measured at an open area with a tipping bucket, ~2 km away from

the studied forest site. SWC was measured using a CS616 water content reflectometer (Campbell Scientific Inc., Logan UT) installed horizontally at 5 cm below the soil surface.

Forcing data for the CABLE model simulations for the period 2000-2017 comprised gridded rainfall, T_{air}, vapour pressure deficit and solar irradiance surfaces. Daily means of meteorological data gridded at 0.05° spatial resolution were retrieved from the Bureau of Meteorology's Australian Water Availability Project data set (BoM AWAP) (Grant et al. 2008, Jones et al. 2009). Data for the study site were extracted and then down-scaled to hourly time resolution (Haverd et al. 2013).

3.3.1.3 Leaf area index

I used 4 different approaches to estimate LAI, LAI_{PPFD}, LAI_{photo}, LAI_{scaled} and LAI_{EVI}. LAI_{PPFD} was estimated continuously at the site from 2014 to 2017 using the methods presented in (Duursma et al. 2016). In brief, canopy light transmittance was measured as the ratio between a PPFD sensor (LI-190SB, LI-COR Inc, Lincoln, NE, USA) above the canopy, at 23.5 m height, installed at a nearby site (within 2 km), and three PPFD sensors below the canopy (on metal posts at 1 m height). The diffuse fraction of PPFD (F_{diff}) was measured using a BF5 Sunshine sensor (Delta-T Instruments, Cambridge UK) installed on the flux tower at 29 m. Only diffuse conditions ($F_{diff} > 0.98$) were used to calculate canopy transmittance (τ_d) for every 30-min time step, which were then resampled to daily means. LAI_{PPFD} was then estimated from τ_d following (Campbell and Norman 2012).

$$\tau_d = F_{PPFD,below}/F_{PPFD,above} \tag{3.1}$$

$$\tau_d = 2\int_0^{\pi/2} e^{-LG(\theta)/\cos(\theta)} \sin(\theta)\cos(\theta)\, d\theta \tag{3.2}$$

where $F_{PPFD,below}$ (μmol m^{-2} s^{-1}) is the average of PPFD of the three sensors below the canopy, and $F_{PPFD,above}$ is above canopy PPFD, θ is the solar zenith angle, G(θ) is the foliage projection function in the direction of the beam (I assumed a spherical leaf angle distribution,

so G(θ) = 0.5) (Stenberg 2006, Campbell and Norman 2012), and L is LAI. LAI (L in the equation) was solved numerically.

Because measurements of canopy light transmittance include non-leaf elements of the canopy (stem, branches), the magnitude of LAI_{PPFD} is highly uncertain. However, non-leaf elements are relatively constant in time compared to leaves, therefore I focus on the time dynamic of estimated LAI_{PPFD}.

In parallel, I estimated LAI_{photo} using the methods presented in (Macfarlane et al. 2007, Macfarlane et al. 2014). Upward canopy cover photographs were taken at 1 m height at 121 points on a 10 m x 10 m grid on 6 dates (see Figure S3. 1), using a Nikon D90 camera with a Nikon AF 50 mm lens (Nikon Corporation, Tokyo, Japan). For the calculation of LAI_{photo}, I used an extinction coefficient (k) of 0.5, as recommended by (Macfarlane et al. 2007).

LAI_{PPFD} and LAI_{photo} were correlated, but LAI_{photo} was higher than LAI_{PPFD}. Linear regression between the methods yielded the equation:

$$\mathrm{LAI_{photo}} = 2.65\mathrm{LAI_{PPFD}} - 1.13 \tag{3.3}$$

($r^2 = 0.6$, $p = 0.07$, $n = 6$, see Figure S3. 1). The difference in magnitude between the two methods highlights the uncertainties of LAI magnitude, however the correlation between the two methods strengthens our confidence in the validity of the time dynamic. I assumed that our estimated LAI_{photo} reflects the actual magnitude of LAI that is relevant for ecosystem carbon and water exchange (Macfarlane et al. 2007), and thus used equation 3.3 to scale the more detailed time series of LAI_{PPFD}, obtaining LAI_{scaled}.

I also estimated LAI_{EVI} for the years 2001-2017 as the result of a linear regression between enhanced vegetation index (EVI) and LAI_{scaled}, which gave $LAI_{EVI} = 11.95EVI - 2.34$, $r^2 = 0.68$. EVI was obtained from the years 2000-2017 from the MODIS Vegetation Indices 16-day L3 Global 250 m product (MOD13Q1), using the pixel centred on the tower,

atmospherically corrected for surface reflectance masked for water, clouds, heavy aerosols and cloud shadows (Didan 2015b).

3.3.1.4 Litterfall and leaf growth

I collected litterfall (F_{Lfall}, g m^2 $month^{-1}$) in the tower footprint approximately once per month, using nine litter traps (0.14 m^{-2} ground area) located within 5 m of the understory F_{PPFD} sensors. For each month, I partitioned the litter into eucalypt leaves, mistletoe leaves and other (mostly woody) components. I estimated leaf mass per area (L_{MA}) of eucalyptus and mistletoe leaves by sampling approximately 50 fresh leaves of each, in June 2017 (177 g m^{-2} for eucalypt, 248 g m^{-2} for mistletoe). I used this L_{MA} to estimate leaf litter production (P_{leaf}) in m^2 m^{-2} $month^{-1}$ of eucalypt, mistletoe and total as the sum of both. Then, I estimated leaf growth ($F_{Lgrowth}$, m^2 m^{-2} $month^{-2}$) as the sum of the net change in LAI (ΔL) and P_{leaf}.

I also estimated canopy leaf carbon pool (C_{leaf}, g C m^{-2}), as

$$C_{leaf} = LAI \cdot L_{MA} \cdot 0.5 \tag{3.4}$$

where L_{MA} is leaf mass per area (g m^{-2}), and 0.5 converts dry mass of leaves to carbon mass. L_{MA} is approximated as the average of eucalypt and mistletoe L_{MA}, based on the observed equal contributions of each to total leaf litterfall (not shown).

3.3.1.5 Net ecosystem exchange of CO_2 and H_2O: observation

Exchanges of carbon and water were continuously measured, every 30 minutes, from 2014 to 2017 (4 years) at the study site, using the eddy-covariance method, as described by Renchon et al. (2018). In brief, ecosystem-atmosphere exchanges of water (F_W) were measured as the vertical turbulent exchange (change in storage of water were negligible), and exchanges CO_2 (F_{NEE}) were measured as the sum of vertical turbulent exchange (F_{CT}) and rate of change in storage (F_{CS}):

$$F_{NEE} = F_{CT} + F_{CS} \quad (3.5)$$

where F_{NEE} is the net ecosystem exchange of CO_2, F_{CT} is the vertical turbulent flux and F_{CS} is the change in storage. F_{NEP} was estimated as – F_{NEE}.

Density of CO_2 or water vapour (open-path IRGA (LI-7500A, LI-COR Inc., Lincoln NE, USA)) and vertical wind speed (CSAT 3D sonic anemometer (Campbell Scientific Inc., Logan UT, USA)) were measured at 29 m height, 5 m above the canopy, at high frequency (10 Hz) and processed using EddyPro (EddyPro® Software (Version 6.2). LI-COR, Inc., Lincoln NE) to process the raw signal and calculate F_{CT} and F_W and a quality check (qc) flag (0: best quality) of F_{CT} accounting for stationarity tests and turbulence development tests as presented in (Foken et al. 2004). Furthermore, data with a friction velocity (u_*) below 0.2 m s^{-1} were discarded (Renchon et al. 2018).

The change in storage of CO_2 is calculated using data from a profiler system (CO_2 measured at 8 heights), following the equation (Aubinet et al. 2001):

$$F_{CS} = \left(\frac{\Delta C}{\Delta t}\right)_{k=1} \times z_{k=1} + \sum_{k=2}^{n}\left\{\left[\left(\frac{\Delta C}{\Delta t}\right)_{k} + \left(\frac{\Delta C}{\Delta t}\right)_{k-1}\right] \times \frac{z_k - z_{k-1}}{2}\right\} \quad (3.6)$$

where F_{CS} is the change in storage flux of CO_2, C is the CO_2 concentration (µmol m^{-3}) measured at the height z or k (m), t (s) is the time between two measurements (1800 s or 30 min), and z or k is the height of a layer (between two inlets sampling CO_2).

Missing and discarded F_{NEP} were filled with a neural-network in PyFluxPro (Isaac et al. 2017), allowing for monthly and annual budget by integration. The neural network predicted F_{NEP} as a function of short-wave radiation, vapour pressure deficit, T_{air}, soil temperature and soil water content. F_{NEP} was partitioned into F_{GEP} and F_{ER} using a neural-network with 10 nodes and 500 iterations to predict ecosystem respiration (F_{ER}) as a function of soil temperature, T_{air} and SWC (Isaac et al. 2017, Renchon et al. 2018). F_{GEP} was calculated as $F_{NEP} + F_{ER}$.

3.3.1.6 Net ecosystem exchange of CO_2 and H_2O: modelling

I used the CABLE-POP terrestrial biosphere model (Haverd et al. 2017, Haverd et al. 2018), parameterised using flux data (F_{NEP}, F_{ET} and R_{soil} quality filtered observations from 2014-2017) with PEST (model-independent Parameter Estimation and Uncertainty Analysis, http://www.pesthomepage.org/), on site measured environmental data and varying LAI_{EVI}. CABLE-POP uses the following environmental inputs: T_{air}, rainfall, short-wave downwelling radiation, long-wave down radiation, surface specific humidity, wind speed, surface air pressure, and CO_2 concentration. I enabled the option to use LAI_{EVI} as either a prescribed times series or a fixed value to test the effects of weather separately from the effects of LAI_{EVI} dynamics on the fluxes.

I conducted two different runs of CABLE: one simulation with fixed LAI_{EVI} (equal to the average of observed LAI_{EVI}) and the other simulation with observed, varying LAI_{EVI}, and compared model outputs to the measured data (quality filtered F_{NEP} and F_{ET}) over the 2014-2017 period.

I also used model outputs of F_{NPP}, F_{GEP} and F_{NEP} to assess if these fluxes had a similar dynamic as LAI over the period 2001-2017.

Table 3.2 CABLE-POP parameters fitted to measured data (net ecosystem production and evapo-transpiration (F_{ET}) from eddy-covariance data and soil respiration (F_{SR}) from auto-chambers).

Parameter	Description
α (mol mol^{-1})	Quantum yield of electron transport (Farquhar and Wong 1984)
k_n (dimensionless)	Extinction coefficient for leaf nitrogen with canopy depth
g_1 (kPa$^{0.5}$)	Stomatal conductance parameter (Medlyn et al 2011)
γ (dimensionless)	Sensitivity of stomatal conductance and root water uptake to SWC (Haverd et al. 2016)
Vcmax_scalar (dimensionless)	Scaling factor on prior estimate of maximum catalytic activity of Rubisco, as prescribed by Walker et al. 2014

3.3.2 Photosynthetic capacity

I used the two simulations of CABLE (with varying LAI or fixed LAI) to estimate the seasonal and interannual variability of modelled gross ecosystem productivity (F_{GEP}). This allows us to quantify how much variation in LAI and weather contribute, either alone or combined, to anomalies in modelled F_{GEP}.

I defined monthly photosynthetic capacity (PC) as the average of F_{GEP} under "optimal" environmental conditions (F_{PPFD} > 1000 umol m^{-2} s^{-1}, D < 1.3 kPa, SWC > median(SWC)) (Renchon et al. 2018). For the period 2014-2017, I calculated PC in the flux data, and in the model with constant LAI and the model with varying LAI to compare observed seasonal and interannual variation of PC with simulations from both model versions.

3.3.3 Seasonal allocation of F_{NPP} to leaf growth

In CABLE, F_{NPP} is estimated as the difference of F_{GEP} and autotrophic respiration (Haverd et al. 2018). To estimate the allocation of (predicted) F_{NPP} to leaf growth, I used a simple difference model of leaf biomass (C_{leaf}) (Battaglia and Sands 1997), which assumes that the variation of C_{leaf} over a period of time is equal to the initial leaf biomass plus leaf growth minus litter fall (F_{Lfall}) (equation 3.7 and 3.8). I assumed that leaf growth ($F_{Lgrowth}$) is equal to the allocation to leaves times F_{NPP} and F_{Lfall} is equal to the fraction of the initial C_{leaf} senescing over this period of time (equation 3.9).

$$C_{leaf_{t+1}} = C_{leaf_t} + \frac{dC_{leaf}}{dt} \tag{3.7}$$

$$\frac{dC_{leaf}}{dt} = F_{Lgrowth} - F_{Lfall} \tag{3.8}$$

$$\frac{dC_{leaf}}{dt} = a_f F_{NPP} - k_f C_{leaf} \tag{3.9}$$

where $F_{Lgrowth}$ is leaf growth (gC m^{-2} day^{-1}), F_{Lfall} is litter fall (gC m^{-2} day^{-1}), C_{leaf} is leaf biomass (gC m^{-2}), t is time (day), a_f is the allocation of F_{NPP} to leaf growth (fraction, 0 to 1), and k_f is the turnover rate of leaf biomass due to senescence (day^{-1}).

The only unknowns in these equations are the allocation of F_{NPP} to leaf growth ($a_f = F_{Lgrowth} / F_{NPP}$) and the turnover rate due to senescence ($k_f = C_{leaf} / F_{Lfall}$), which can be calculated directly using the measured estimates of $F_{Lgrowth}$ and F_{Lfall}, and the modelled estimate of F_{NPP}.

3.4 Results

3.4.1 Environmental drivers and phenology of LAI_{EVI}

Over the 17-year simulation period (2001-2017), annual precipitation averaged 763 mm, T_{air} averaged 17.6 °C and LAI_{EVI} averaged 1.34 m^2 m^{-2} (Table 3.3). Monthly precipitation was highly variable and ranged from 0 mm (June 2001) to 325 mm (March 2017) (Figure 3.1), with summer months generally wetter than winter months (average of 100 mm $month^{-1}$ in December through February, and average of 40 mm $month^{-1}$ in June through August, Figure 3.1). Monthly mean T_{air} ranged from 9.1 °C in July 2002 to 26.9 °C in January 2017 (Figure 3.1). Monthly mean of LAI_{EVI} ranged from 0.8 to 2.0 m^2 m^{-2} over the 4-year period of record with measurements (2014-2017) and peaked each year between February and April (Figure 3.1, Figure 3.2). Monthly LAI_{EVI} increased most rapidly during wet summer months; the rate of increase correlated significantly with precipitation ($r^2 = 0.20$, $p < 0.005$, $n = 204$) and T_{air} ($r^2 = 0.24$, $p < 0.005$, $n = 204$), but was most strongly predicted by the combination of T_{air} and precipitation ($r^2 = 0.29$, $p < 0.005$, $n= 204$) (Figure S3. 2). Mean annual LAI_{EVI} varied from 1.03 m^2 m^{-2} in 2003 to 1.64 m^2 m^{-2} in 2016 (Table 3.3). The magnitude of the yearly LAI_{EVI} max was negatively correlated with the day of year on which the max occurred (i.e. years with a low LAI_{EVI} max had a late LAI_{EVI} max, $r^2 = 0.3$, $p = 0.04$, $n = 14$, Figure 3.2). Precipitation in summer was negatively correlated with day of the year with maximum LAI_{EVI} (e.g. if summer precipitation was low, the day of the year with maximum LAI_{EVI} occurred later $r^2 = 0.35$, $p = 0.025$, $n = 14$, Figure 3.2). Overall, high summer precipitation led to a high and early LAI_{EVI} max whereas low summer precipitation led to a low and late LAI_{EVI} max. On a longer time-scale, LAI_{EVI} had a high coherence with precipitation on an annual period, with no lag (Figure S3. 3), and the yearly max of LAI_{EVI} was correlated with precipitation over the previous 13 months ($r^2 = 0.47$, $n = 14$, Figure S3. 4).

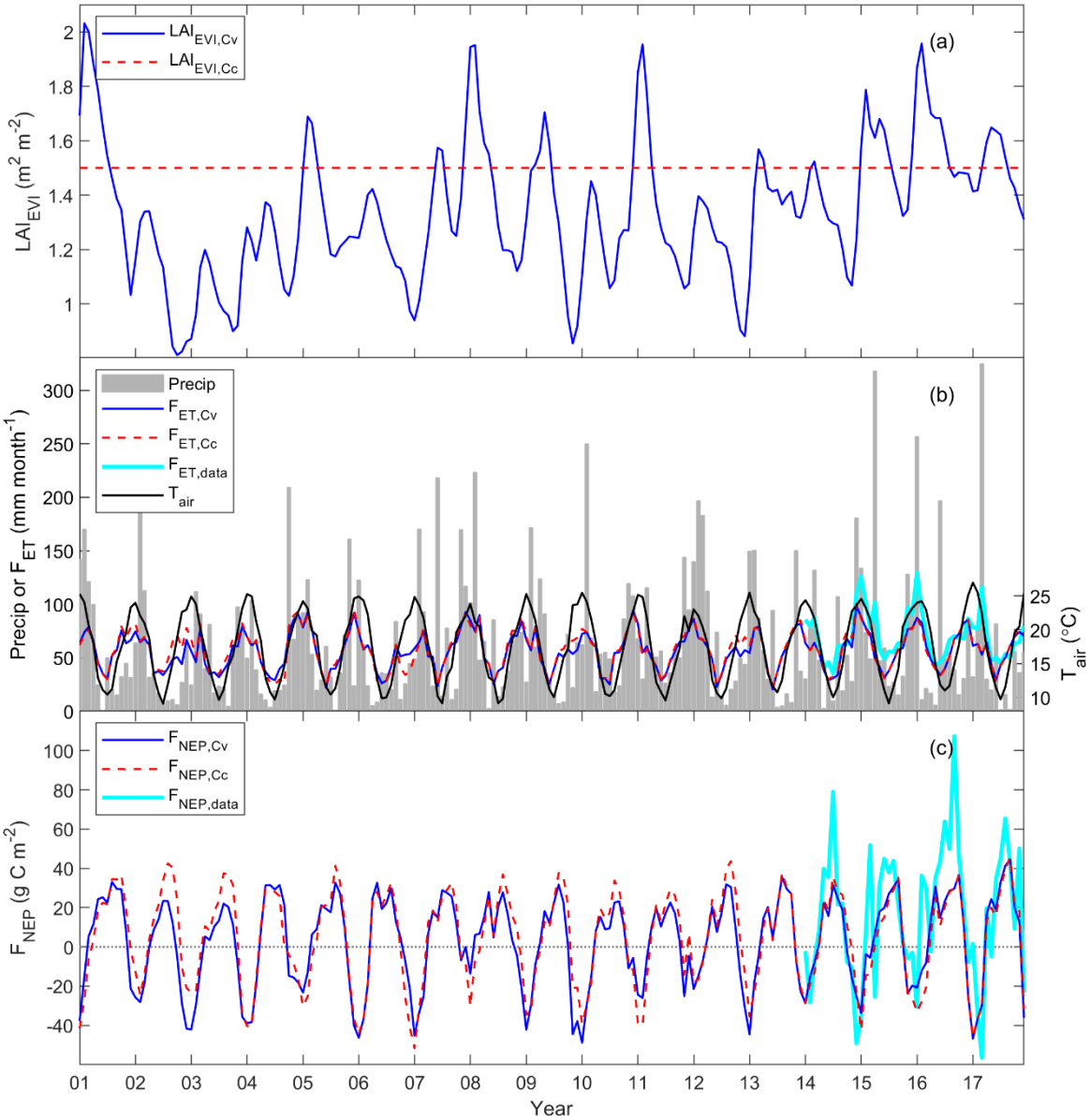

Figure 3.1 Time series of leaf area index, precipitation, air temperature, net ecosystem productivity and evapotranspiration over the 2001-2017 period. (a) Time series over the 17-year period (2001-2017) of leaf area index estimated from enhanced vegetation index (LAI_{EVI} as in 3.3.1.3). Continuous blue line: varying LAI used as input for CABLE (Cv). Dotted red line: constant LAI used as input for CABLE (Cc). (b) Time series of precipitation, evapotranspiration and air temperature (T_{air}, °C). Grey bars: precipitation (Precip, mm month^{-1}). Black line, monthly mean T_{air}. Precipitation and T_{air} are estimated from BIOS climate, see methods section 3.3.1.2. Continuous blue line: Cv evapo-transpiration (F_{ET}, mm month^{-1}). Dotted red line: $F_{ET,Cc}$. Thick continuous cyan line: F_{ET} observation (c) Time series of monthly net ecosystem productivity (F_{NEP}, g C m^{-2}). Continuous blue line: $F_{NEP,Cv}$. Dotted red line: $F_{NEP,Cc}$. Thick continuous cyan line: F_{NEP} observations.

3.4.2 Phenology of climate, canopy and observed fluxes

The timing of maximum and minimum F_{PPFD}, T_{air} and D followed the expected seasonal pattern, i.e. maximum in summer, minimum in winter (Figure 3.4k-m). Monthly average precipitation was maximum in summer and autumn, while SWC was maximum in autumn and winter (Figure 3.4n-o). As noted above, LAI peaked in late-summer (Figure 3.4f). PC, estimated using eddy-covariance data, generally followed LAI_{EVI} with a time lag, peaking in autumn, one or two months after LAI_{EVI} max, but also showed a second peak in spring (Figure 3.4f-g). Eddy-covariance optimal surface conductance had a seasonal pattern similar to those of LAI_{EVI} and SWC (Figure 3.4f, j, o). Annual mean F_{Lfall} was 157 g C m^{-2} or 1.57 m^2 m^{-2} of leaves, which is close to mean LAI for the site, implying a leaf life span of about a year. $F_{Lgrowth}$ and F_{Lfall} both showed peaks in spring and autumn and reduced to near-zero values during winter.

High LAI and high PC in autumn led to a maximum of $F_{GEP,EC}$ in autumn, with a lower peak in spring, and minimum values in summer and winter (Figure 3.4c). $F_{ER,EC}$ peaked in summer, and had a larger seasonal amplitude compared to $F_{GEP,EC}$. As a result, $F_{NEP,EC}$ was positive in winter and negative in summer (Figure 3.4a-c-d). Interestingly, $F_{ET,EC}$ was in anti-phase with $F_{NEP,EC}$, as $F_{ET,EC}$ was maximum in summer and minimum in winter, and the opposite for F_{NEP} (Figure 3.1b-c). This surprising pattern resulted from seasonal F_{NEP} following the seasonality of F_{ER}, which was bigger than the seasonality of F_{GEP}.

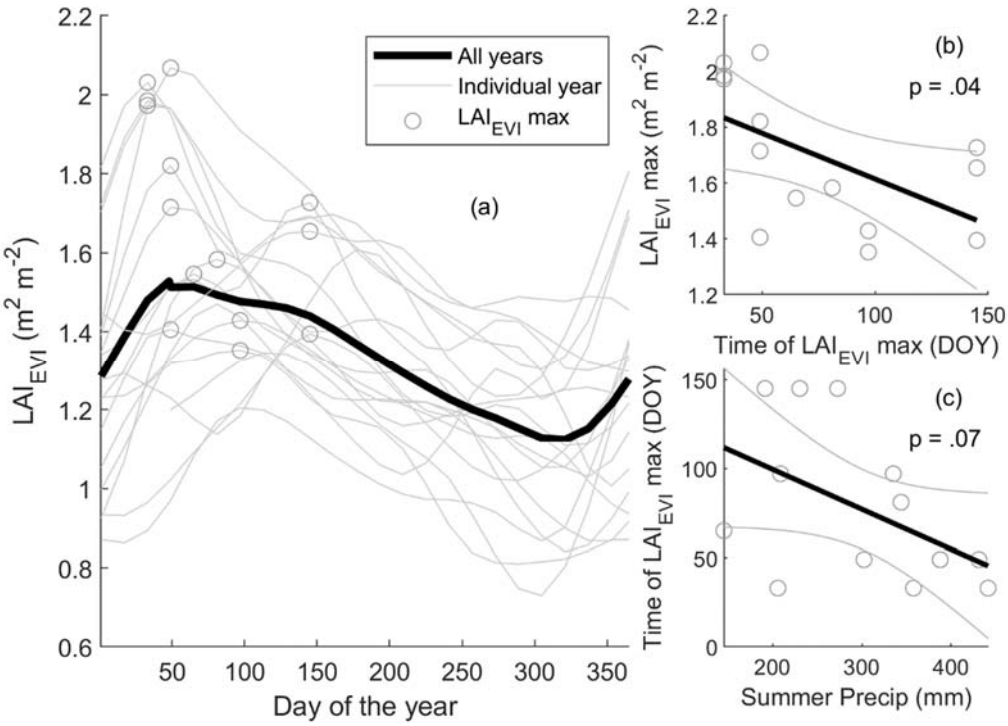

Figure 3.2 Phenology of leaf area index. (a) Seasonality of leaf area index estimated from enhanced vegetation index (LAI_{EVI}, as in 3.3.1.3) over the 17-year period (2001-2017). Black line: daily average for all years. Grey lines: daily value for individual years. Dots show yearly maxima. (b) Linear regression of LAI_{EVI} max (m^2 m^{-2}) vs. time of LAI_{EVI} max (day of the year, DOY), $r^2 = 0.3$, $p = 0.039$, $n = 14$. (c) Linear regression of time of LAI_{EVI} max (DOY) vs. summer (Dec-Jan-Feb) precipitation (mm), $r^2 = 0.35$, $p = 0.026$, $n = 14$. Higher LAI_{EVI} max tended to occur earlier in the year (a), and the DOY of LAI_{EVI} max occurred earlier when summer precipitation was high (b).

3.4.3 Model results

3.4.3.1 Model simulation vs. observations

After parameterisation using PEST (see Table S3. 1 for parameter values, and Table S3. 2 for parameter correlation matrix), I simulated the fluxes using CABLE (see Figure S3. 5 for a linear regression of observation (non-gap-filled) vs. model over the period 2014-2017). CABLE correctly simulated the sensitivity of F_{NEP} to D and SWC: the slope of light saturated F_{NEP} versus D was similar between the model and the observations, although the modelled F_{NEP} was slightly lower at low D (Figure 3.3).

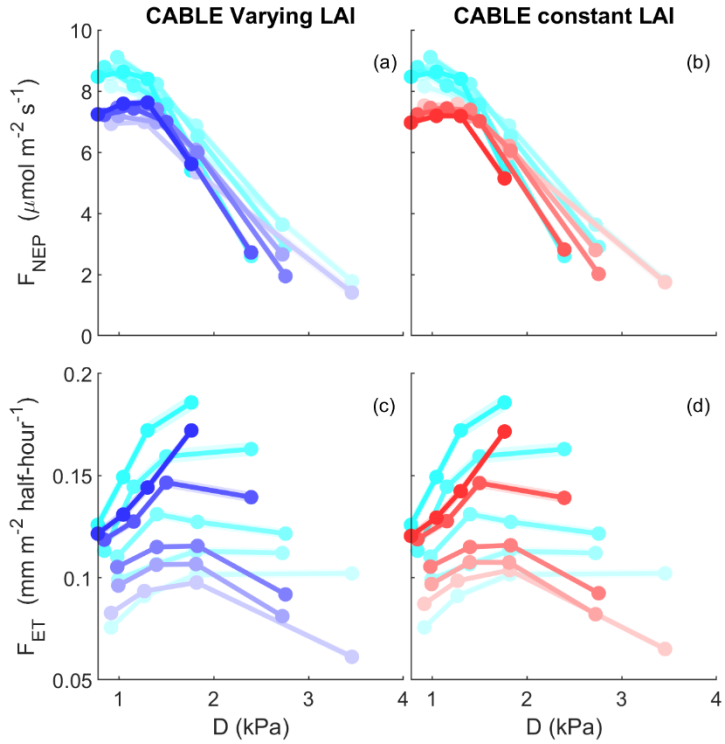

Figure 3.3 Response of light saturated (F_{PPFD} > 1000) net ecosystem productivity (F_{NEP}, µmol m^{-2} s^{-1}) and evapotranspiration (F_{ET}, mm half-hour^{-1}) to vapor pressure deficit (D, kPa) and soil water content (SWC, brightness indicates SWC, for 5 quantiles, from wet (dark) to dry (bright)). Dots indicates average of y value for 4 quartiles of x, shading indicates standard error. Blue line: CABLE with varying LAI. Red line: CABLE with constant LAI. Cyan line: eddy-covariance observation.

Seasonal cycles of CABLE F_{ET} and F_{NEP} were similar to those in eddy-covariance observations (anti-phase, with maximum F_{ET} in summer and maximum F_{NEP} in winter (Figure 3.4a-b)), but CABLE did not entirely reproduce the observed variability in the data. Extremes, particularly in summer, were not reproduced by the model (Figure 3.1b-c).

The simulated seasonal cycles of the component fluxes F_{ER} and F_{GEP} were generally similar to those observed in eddy-covariance data, but the eddy-covariance derived values $F_{GEP,EC}$ and $F_{ER,EC}$ were generally higher in magnitude than the modelled values, particularly in autumn (Figure 3.4c-d). For example, in March, $F_{GEP,EC}$ was 147.7 g C m^{-2} on average, while $F_{GEP,Cv}$ was only 103.8 g C m^{-2}. Modelled F_{GEP} also produced a dual peak, in spring and autumn, but monthly $F_{GEP,EC}$ was maximum in March, shortly after LAI_{EVI} peaked, while $F_{GEP,Cv}$ was maximum in September, coinciding with one of the lowest monthly LAI_{EVI}

(Figure 3.4c-f). The magnitude of PC_{Cv} was lower than the magnitude of PC_{EC}, and the variability of monthly PC_{Cv} (1.5 µmol m^{-2} s^{-1}) was much lower than that of PC_{EC} (4.9 µmol m^{-2} s^{-1}). In contrast, the variability and seasonal patterns of measured and modelled $G_{s,opt}$ were similar, albeit lagged in time (Figure 3.4g-j).

$F_{NPP,Cv}$ and $F_{NPP,Cc}$ both had two peaks during the year, a first peak in spring and a second, lower peak in autumn (Figure 3.4e), as autotrophic respiration was high during the summer owing to the high temperatures. The peak of $F_{NPP,Cv}$ differed from the peak of $F_{Lgrowth}$, which was maximum in summer (Figure 3.4h). As a result, a_f was not constant throughout the year, but peaked in summer, ranging from 0.009 in August to 0.57 in January (Figure 3.4i).

3.4.4 Comparison between simulations with constant and varying LAI

There were differences between simulations with constant and variable LAI. For F_{NEP}, the variable LAI simulation had a lower seasonal amplitude compared to the constant LAI simulation (27.8 vs. 33.1 g C m^{-2}, Figure 3.4a), but it also had a markedly larger inter-annual variability (Figure 3.5, Table 3.3). $F_{NEP,Cc}$ ranged from -18.8 to 120.8 g C m^{-2} yr^{-1} while $F_{NEP,Cv}$ ranged from -66 to 125.1 g C m^{-2} yr^{-1}. On an annual timescale, none of $F_{NEP,Cv}$, $F_{NEP,Cc}$ or $F_{NEP,EC}$ correlated with climate variables (annual precipitation or average T_{air}), but both $F_{NEP,Cv}$ and $F_{NEP,EC}$ were correlated with mean annual LAI_{EVI} (Figure 3.5, $F_{NEP,Cv}$ vs. LAI_{EVI}: $r^2 = 0.72$, n = 17 $F_{NEP,EC}$ vs. LAI_{EVI}: $r^2 = 0.68$, n = 4).

Over the four-year period 2014-2017, PC_{EC} was significantly correlated with LAI_{EVI} on monthly time scale (slope = 8.0 ± 1.4, $r^2 = 0.40$, $p < 0.001$, n = 48) (Figure S3. 5). PC_{Cv} was also significantly correlated with LAI_{EVI}, but with a lower slope (slope = 3.5 ± 0.4, $r^2 = 0.65$, $p < 0.001$, n = 48). $PC_{,Cc}$ was not correlated with LAI_{EVI}, suggesting that variable LAI is a major contributor to the observed variability in PC.

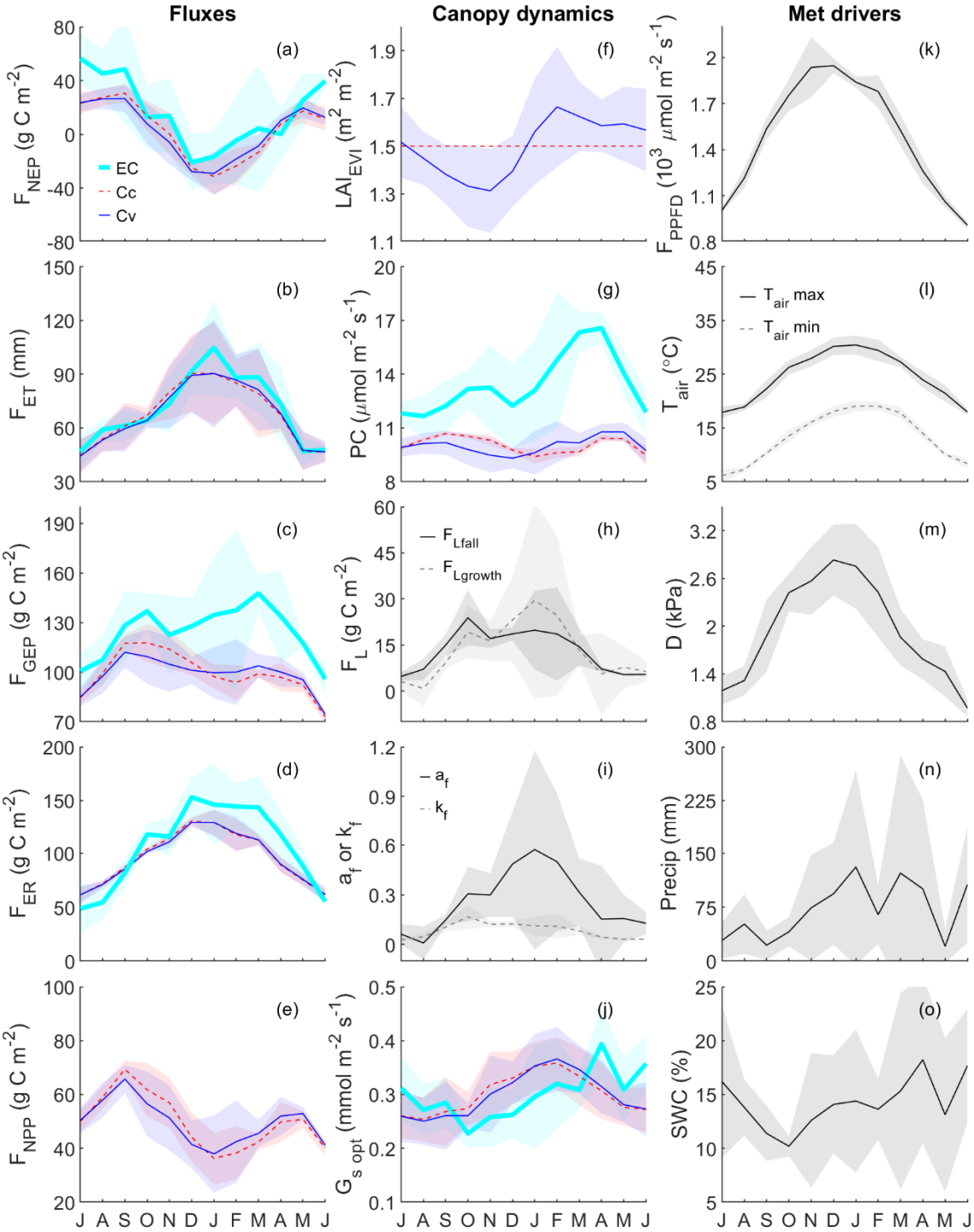

Figure 3.4 Monthly fluxes, canopy dynamic and meteorological drivers. Average monthly measured and modelled fluxes (left column), canopy dynamics (middle column), and meteorological drivers (right column) at the Cumberland Plain woodland, during the 4-year period 2014-2017. Lines indicate monthly mean values, averaged over four years. Shading indicates standard deviation calculated for four years (n = 4). (a) Net ecosystem productivity (F_{NEP}, gC m^{-2} month^{-1}), (b) Evapotranspiration (F_{ET}, mm month^{-1}), (c) Gross ecosystem productivity (F_{GEP}, gC m^{-2} month^{-1}), (d) Ecosystem respiration (F_{ER}, gC m^{-2} month^{-1}), (e) Net primary productivity (F_{NPP}, gC m^{-2} month^{-1}), (f) Monthly leaf area index (LAI_{EVI}, m^2 m^{-2}), (g) Photosynthetic capacity (PC, µmol m^{-2} s^{-}1, F_{GEP} under optimal conditions: F_{PPFD} > 1000 &

D < 1.3 kPa), (h) Litter fall and leaf growth (F_{Lfall} and $F_{Lgrowth}$, gC m^{-2} $month^{-1}$), (i) Allocation of F_{NPP} to leaf growth and canopy turnover (a_f and k_f, fraction and $month^{-1}$), (j) Surface conductance ($G_{s,opt}$, mmol m^{-2} s^{-1}), (k) Daily maximum photosynthetic photon flux density (F_{PPFD}, µmol m^{-2} s^{-1}), (l) Daily maximum and minimum air temperature (T_{air} max and T_{air} min, °C), (m) Daily maximum atmospheric demand (D, kPa), (n) Monthly precipitation (Precip, mm $month^{-1}$), (o) Soil moisture content (SWC, %). Continuous blue line is for CABLE simulation with varying LAI. Dotted red line is CABLE simulation with constant LAI. Thick continuous cyan line is for eddy-covariance estimates. Black line shows canopy dynamics or meteorological variables. Note that the x-axis, the month of the year, is centred on December-January, which are summer months in Australia.

Table 3.3 Annual precipitation, air temperature, leaf area index, and net ecosystem productivity over the period 2001-2017. Inter-annual variability of meteorology (precipitation and T_{air}) and leaf area index estimated from enhanced vegetation index over the 17-year period 2000-2017. Note the large inter annual range (max – min) of leaf area index relative to its average magnitude (0.6 compared to 1.3). Bold values indicate maxima and minima.

Year	Precipitation (mm)	T_{air} (°C)	LAI_{EVI} (m^2 m^{-2})	$F_{NEP,Cv}$ (g C m^{-2})	$F_{NEP,Cc}$ (g C m^{-2})	$F_{NEP,data}$ (g C m^{-2})
2001	752.5	17.4	1.58	114.3	114.4	NA
2002	626.3	17.5	**1.09**	**-66.0**	97.0	NA
2003	651.1	17.2	1.03	-42.0	84.5	NA
2004	648.8	17.6	1.21	8.3	-1.6	NA
2005	702.4	17.7	1.36	48.6	42.6	NA
2006	**479.2**	17.6	1.23	15.8	**-18.8**	NA
2007	**1022.4**	17.7	1.32	23.7	38.0	NA
2008	810.6	**16.8**	1.44	90.1	112.1	NA
2009	691.5	18.0	1.31	-53.7	18.1	NA
2010	911.4	17.5	1.26	-11.8	29.5	NA
2011	782.9	17.2	1.38	14.6	30.2	NA
2012	880.8	17.0	1.19	33.3	**120.8**	NA
2013	789.2	18.0	1.39	54.6	50.1	NA
2014	714.2	18.0	1.31	19.1	58.9	**101.4**
2015	996.9	17.7	1.55	51.9	0.8	171.2
2016	779.5	**18.3**	**1.64**	**125.1**	61.9	**392.7**
2017	731.0	18.2	1.49	62.0	58.9	148.9
Average	763.0	17.6	1.34	28.7	52.8	203.5
Max – min	543.2	1.5	0.62	191.1	139.6	291.3

3.5 Discussion

3.5.1 Environmental drivers and phenology of LAI_{EVI}

The seasonality of leaf growth and LAI in evergreen broadleaved forests is often assumed to be constant throughout the year in LSMs, because observed changes can be subtle. The dynamic of leaf growth of Australian eucalypt forests is often seasonal – increasing in summer – rather than responding to climate drivers (Pook 1984a, Pook et al. 1997, Williams et al. 1997, Bach 2002, England and Attiwill 2008). In this analysis, I found that leaf growth occurred in summer months (December through February), which also happened to be the period of higher precipitation and high T_{air}.

I further found that the timing and magnitude of LAI_{EVI} yearly maxima were driven by summer precipitation, with high and early peak when summer precipitation was high (Figure 3.2). However, the range of LAI_{EVI} was low in comparison to ecosystems with larger ranges in temperature or precipitation (Moore et al. 2016).

Change in LAI is related to carbon allocation to leaves, and turnover rate. Understanding the dynamics of carbon allocation is a key challenge to improve vegetation modelling (Zuidema et al. 2018). Identifying the mechanisms regulating this observed pattern will be important to improve land surface modelling of evergreen forests. I attempted to infer the allocation pattern by comparing modelled F_{NPP} with the growth pattern. The estimate of F_{NPP} allocation to leaf growth was high in summer and low in winter (Figure 3.4i). Another interpretation of this result may be that trees are using carbon reserves for leaf growth in summer, rather than changing F_{NPP} allocation to leaf growth, as estimated F_{NPP} allocation relied on the assumption that only carbon from F_{NPP} could be allocated to leaves. Further study is required to specifically address this question and would require estimates over time of carbon allocation to different pools (leaves, roots, wood, storage), and what carbon is used to grow tissue (recently acquired carbon or old carbon stored).

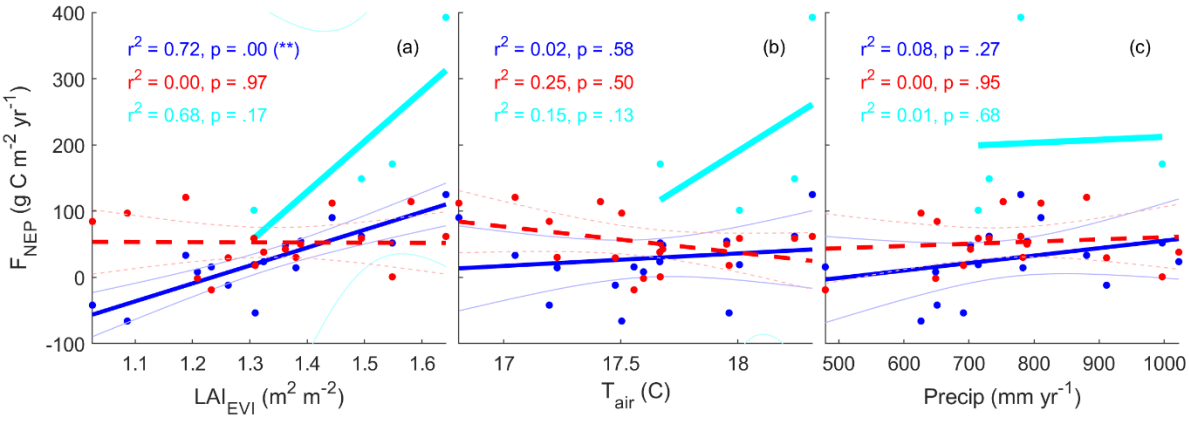

Figure 3.5 Annual net ecosystem productivity vs. LAI, T_{air} and precipitation. Linear regression of annual net ecosystem productivity (F_{NEP}, g C m^{-2} yr^{-1}) vs. (a) annual mean leaf area index estimated from enhanced vegetation index (LAI_{EVI}, m^2 m^{-2}), (b) annual mean air temperature (T_{air}, °C), and (c) annual mean precipitation (Precip, mm yr^{-1}). In all panels, continuous blue line and dots are for F_{NEP} estimated from CABLE with varying LAI_{EVI} input. Dashed red line and dots are for F_{NEP} estimated from CABLE with constant LAI_{EVI} input. Continuous thick cyan line and dots are for F_{NEP} estimated from eddy-covariance observations. Thin lines show the 95% confidence interval of the regression lines (often out of borders for the eddy-covariance regression). (**) indicates that the slope is significantly different from 0 at the 0.01 level.

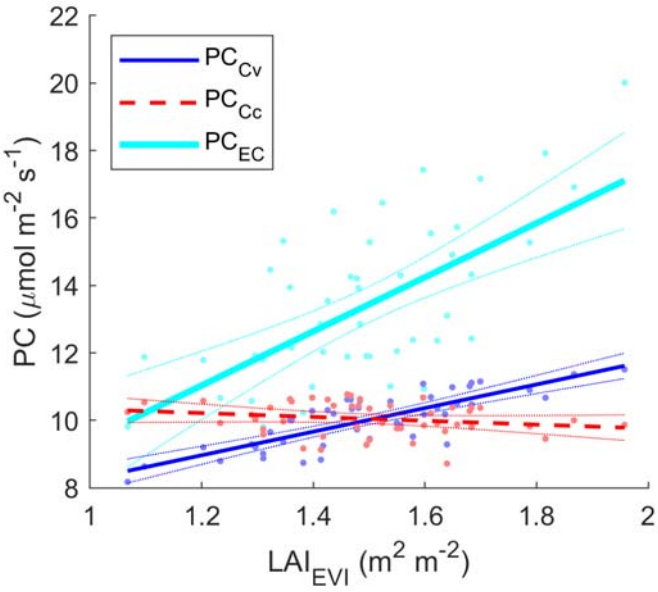

Figure 3.6 Monthly photosynthetic capacity vs. leaf area index. Whole canopy photosynthetic capacity estimated as monthly mean of F_{GEP} under optimal conditions (F_{PPFD} > 1000 & D < 1.3), versus monthly estimated LAI_{EVI} ("seen" by the data and the model with varying LAI_{EVI} only), over the 4-year period 2014-2017 (n = 48 months). Cyan dots and thick continuous cyan line: eddy-covariance (EC) estimated values of PC. Slope of the fitted line is 8.0 ± 1.4 (r^2 = 0.40, p < 0.001). Red points and dashed red line: CABLE PC, estimated with constant LAI_{EVI} (Cc), against observed LAI_{EVI}. Slope of the fitted line is -0.6 ± 0.4 (r^2 = 0.05, p = 0.14). Blue points and continuous blue line: CABLE PC, estimated with varying LAI_{EVI} (Cv), against observed LAI_{EVI}. Slope of the fitted line is 3.5 ± 0.4 (r^2 = 0.65, p < 0.001).

Previous studies in other sclerophyll forests in South-East Australia were found to be a net carbon sink all year long, but particularly in summer (Keith et al. 2012, Hinko-Najera et al. 2017b). The Cumberland Plain site contrasted with other sclerophyll forests (Tumbarumba and Wombat) with its unusual seasonality, acting as a net source of CO_2 in summer, and as a net sink in winter (Renchon et al. 2018). The ability of LSMs to reproduce this unusual pattern was not known. Model-data comparison allows the mechanisms to be identified that may be lacking in the model (Restrepo-Coupe et al. 2017b).

3.5.2 Model results

3.5.2.1 Simulation vs. observations

After parameterisation, CABLE successfully reproduced the seasonal F_{NEP} pattern of the Cumberland Plain site (Figure 3.4a). Half-hourly F_{NEP} and F_{ET} responses to D and SWC were similar between observation and model (Figure 3.3), albeit a small underestimation by the model at low D (< 1.3 kPa). This model result showed the capacity of the optimal stomatal conductance model to capture these responses (Medlyn et al. 2011). However, there were some important discrepancies between the data and the model during specific seasons, in autumn in particular, with F_{GEP} being underestimated by the model (Figure 3.4c). This seemed to be caused by a variation in PC not captured in the model (Figure 3.4g and Figure 3.6). A possible, reasonable explanation would be the absence of age-dependent leaf level photosynthetic capacity, which was observed to be highest in late summer when leaves were mature at a site within 2 km of the flux tower (Wujeska-Klause et al. 2019). The importance of age-dependent physiology of leaves to determine F_{GEP} seasonality also contributed to seasonal variations in carbon fluxes in a tropical evergreen forest (Wu et al. 2016a). Understanding and incorporating this age dependence of leaf physiology could potentially improve land surface models (Bauerle et al. 2012).

3.5.2.2 Comparison between simulations with constant and varying LAI

Varying LAI_{EVI} was key to understanding inter-annual variability of F_{NEP} in the model (Figure 3.5). Annual F_{NEP}, modelled with both varying and constant LAI, was not correlated with precipitation or T_{air}, but only F_{NEP} modelled with varying LAI was correlated with LAI_{EVI}. The four years of observation had similar results, albeit with lower significance due to the restricted number of annual eddy-covariance observations. The stronger slope of annual $F_{NEP,EC}$ vs LAI_{EVI} was consistent with the higher slope of PC_{EC} vs LAI_{EVI} (Figure 3.6) and may result from age-dependent leaf physiology parameters not incorporated in the model (Prior et al. 2004, Reich et al. 2009, Wu et al. 2016a).

Varying LAI_{EVI} also had an impact on F_{NEP} seasonality, albeit to a lesser degree than for inter-annual variability of F_{NEP}. Surprisingly, $F_{NEP,Cv}$ had a lower seasonality (lower range of values) than $F_{NEP,Cc}$ (Figure 3.4a). In general, plants optimise their PC during optimal growth period, and thus variation in LAI increases F_{NEP} seasonality.

3.6 Conclusions

I observed that LAI_{EVI} peaked each year between February and April, driven by precipitation in summer months. Litter fall and leaf growth were both maximum during summer months, leading to a renewal of the canopy and associated high values of F_{GEP} and PC in late summer or early autumn.

The CABLE model was able to reproduce observed F_{NEP} and F_{ET} responses to drivers such as D and SWC, however it underestimated F_{GEP} in autumn by a large amount. It appeared that variation in LAI_{EVI} were not sufficient to reproduce PC_{EC} (Figure 3.6). Leaf-level gas exchange has been shown to vary with leaf age in a nearby similar forest (Wujeska-Klause et al. 2019), and may explain ecosystem scale PC variability. Accounting for this effect will improve modelled PC.

Inter-annual variability of observed and simulated F_{NEP} were positively correlated with mean annual LAI_{EVI}. Observed variation in LAI_{EVI} slightly dampened the modelled seasonality of F_{GEP} and F_{NEP}. Including varying LAI_{EVI} in the model therefore improved the ability of the model to capture seasonal and inter-annual variability of fluxes. This promises an applicable improvement of modelling for these ecosystems, when seasonal variation in LAI is known.

4 Chapter 4. Contribution of soil CO_2 efflux to seasonal and diurnal dynamics of ecosystem respiration in a dry sclerophyll forest

4.1 Abstract

Understanding seasonal and diurnal dynamics of ecosystem respiration (R_{eco}) in forests is challenging, because it can only be measured directly during nighttime by eddy-covariance flux towers. R_{eco} is the sum of soil respiration (R_{soil}) and above-ground respiration (R_{AG}). I assessed the temporal patterns and climatic drivers of R_{soil} and R_{eco} in a mature eucalypt woodland, using continuous measurements (only at night for R_{eco}) at the half-hourly resolution over 4 years (2014-2017), from which I inferred R_{AG} as $R_{eco} - R_{soil}$. Over the 4-year period, R_{soil} accounted for about 77% of R_{eco}. I observed large seasonal and diurnal (overnight) variation of R_{eco}, while R_{soil} had a low diurnal amplitude and R_{AG} had a low seasonal amplitude. This result implies that seasonal variation of R_{eco} was mainly influenced by R_{soil} while its diurnal variation was mainly influenced by R_{AG}. R_{soil} was well explained by a semi-mechanistic heterotrophic respiration model, the Dual Arrhenius Michaelis Menten model (DAMM, $r^2 \sim 0.6$ at the half-hourly and the daily time scale). DAMM also predicted well daily (night median, $r^2 = 0.64$) R_{eco} but performed poorly to reproduce half-hourly R_{eco} ($r^2 = 0.08$). Prediction of R_{eco} with an artificial neural network (ANN) was improved slightly when half-hourly R_{soil} values were included with soil temperature and moisture contents. Our results call for up-scaling of R_{eco} from chamber measurements of components at hourly time resolution, to verify if the consistent decline of R_{eco} overnight and its magnitude could result from the decline of leaf respiration and/or stem respiration, or if a missing advection term is creating a systematic bias in R_{eco} measurements. Our findings contribute to reconciling bottom-up and top-down estimates of ecosystem respiration.

4.2 Introduction

Ecosystem respiration (R_{eco}) is the largest terrestrial carbon dioxide (CO_2) source, ten times larger than anthropogenic emissions (Le Quéré et al. 2018). R_{eco} is the sum of all CO_2 efflux from an ecosystem, i.e. from soil (R_{soil}), plants, and animals. Soil CO_2 efflux comprises heterotrophic sources (microbial decomposition) and autotrophic sources (root respiration); both are sensitive to soil temperature (T_{soil}) (Lloyd and Taylor 1994) and soil moisture (θ) (Davidson et al. 2012). Aboveground CO_2 efflux (R_{AG}) comprises leaf and stem sources, which respond to air temperature (T_{air}), or more directly to leaf or stem temperature. Leaf respiration is known to acclimate seasonally to temperature, with a lower short term temperature sensitivity compared to long term apparent temperature sensitivity (Atkin et al. 2000, King et al. 2006, Crous et al. 2011). Leaf respiration is also known to be inhibited by light (Kok 1949, Crous et al. 2012, Heskel et al. 2013).

Measuring R_{eco} is challenging in tall canopy ecosystems. Indirect, bottom-up approaches consist of separately measuring different components (R_{soil}, leaf respiration, and stem respiration), scaling-up in space using structural information (bare ground area, stem area, leaf area), and eventually scaling-up in time using non-linear regressions to drivers (Law et al. 1999, Ohkubo et al. 2007, Wang et al. 2017). Direct estimation method (eddy-covariance) is based on solving an equation of conservation of CO_2 mass in a volume, to infer the net ecosystem exchange of CO_2 between an ecosystem and the atmosphere. This method measures R_{eco} during nighttime, when there is no photosynthesis, as the sum of vertical turbulent flux (F_{CT}) and change in storage (F_{CS}) in a control volume (Aubinet et al. 2012).

The most readily available datasets of R_{eco} are provided by eddy-covariance networks such as Fluxnet (http://fluxnet.fluxdata.org/data/fluxnet2015-dataset/). In these datasets, daytime R_{eco} is mostly estimated from one of two methods which use nighttime R_{eco} measurement (i.e. NEE at night) responses to drivers to infer daytime R_{eco}. One common method (Reichstein et

al. 2005), based on a R_{soil} temperature sensitivity study (Lloyd and Taylor 1994), relies on a non-linear regression between night-time R_{eco} and T_{soil} or T_{air} on 15-day windows. This method assumes that soil moisture does not vary during those short 15-day time windows. A popular alternative is an artificial neural network (ANN) (Moffat et al. 2007) based on a machine learning algorithm, allowing the use of many input variables (such as T_{soil}, T_{air}, θ, and potentially others), and which does not pre-suppose the form of the relationship between the dependent and independent variables. Both methods rely on similar assumptions: (1) the response of R_{eco} to drivers is similar between day and night, (2) the response of night R_{eco} can be extrapolated to a range beyond the measurements (e.g. a common issue is that T_{air} is higher during the day than during the night), and (3) the apparent temperature sensitivity estimated over a large time window (e.g., weeks) can be used to estimate short-term temperature sensitivity (e.g. hours). Assumption (1) has the known issue of light inhibition of leaf respiration, as leaf-level studies have shown that leaf CO_2 release in light is lower than leaf CO_2 release in the dark, and that inhibition ranges from 0 to 100% (Farquhar et al. 1980, Tcherkez et al. 2010, Crous et al. 2012). R_{soil} is also subject to bias errors related to chambers, such as the Venturi effect (Bain et al. 2005).

R_{soil} has been measured continuously at an increasing number of sites and can provide a constraint on R_{eco} (Phillips et al. 2017, Wang et al. 2017, Barba et al. 2018). However, mismatches between such bottom-up approaches and eddy covariance based R_{eco} estimates are common, leading to large uncertainty in R_{eco} estimates (Giasson et al. 2013, Thomas et al. 2013, Speckman et al. 2015, Phillips et al. 2017). These uncertainties may arise from different footprints or spatial scale, as the spatial resolution of R_{soil} is much smaller than R_{eco} (~ 0.01 m^2 vs. ~ 1km^2, a scaling factor of 10^6) as well as the time resolution of the measurement (2-5 minutes of sampling for R_{soil} and 30-60 minutes for R_{eco}). R_{soil} is also subject to measurement errors, which are mostly random (Pumpanen et al. 2004, Heinemeyer

et al. 2007, Cueva et al. 2015). In contrast, R_{eco} measurements may be affected by a systematic error (or bias), and have large random error. Night-time measurement of R_{eco} from flux towers has been a longstanding problem because of weak turbulence and advection leading to a potential bias in night data (Aubinet et al. 2000, Van Gorsel et al. 2007). In theory, advection can be positive or negative, as CO_2 may flow horizontally in (positive advection, for example at the bottom of a valley) or out (negative advection, for example at the top of a mountain) of the control volume, however in observations advection is more often negative and occur late at night, as turbulence decreases and the CO_2 build up early night in the canopy flows out of the volume by gravity. Daytime R_{eco} estimation may also be biased from poorly constrained relationships (noisy data or biased relationship), invalid assumptions or incorrect algorithms (Desai et al. 2008).

The objectives of this chapter are to better understand and constrain the diurnal and seasonal patterns of R_{eco} using continuous measurements of R_{soil}. I estimate the contribution of R_{soil} to R_{eco}. I analyse the diurnal (overnight for R_{eco}) and seasonal dynamics of R_{eco}, R_{soil} and R_{AG} ($R_{eco} – R_{soil}$), and their response to environmental drivers (T_{soil}, T_{air}, and θ) over short (half-hourly) and daily time scales. I also investigate if R_{soil} can help improve ANN predictions of R_{eco}, which can be useful to constrain noisy nighttime R_{eco} and fill large gaps of R_{eco}, which often occur with nighttime NEE. Understanding soil respiration and above-ground respiration patterns and response to drivers is an important tool to reconcile the long lasting debate of nighttime and daytime R_{eco} estimates, and hence to improving accuracy of GPP.

4.3 Materials and methods

4.3.1 Site description

The Cumberland Plain Terrestrial Ecosystem Research Network (TERN) OzFlux site (Fluxnet code: AU-Cum), located near Sydney, Australia (latitude: – 33.61518; longitude: 150.72462), is a mature dry sclerophyll woodland, with a stand density of ~ 500 trees ha^{-1}, 140 Mg C ha^{-1} aboveground biomass, a canopy of various ages and up to 25 m in height composed of two main species, *Eucalyptus moluccana* and *E. fibrosa*, with a mid-canopy dominated by *Melaleuca decora* and an understory dominated by *Bursaria spinosa* and various shrubs, forbs, grasses and ferns. This site is equipped with a 30 m high eddy-covariance tower with instrumentations at 29 m height measuring net ecosystem exchange of CO_2 (NEE).

The EucFACE study site is a similar mature woodland within 2 km of AU-Cum, and has a canopy of *E. tereticornis*, and understory dominated by *Microlaena stipoides*, and various shrubs, forbs, and grasses. This site is equipped with six auto-chambers measuring R_{soil} (see section 4.3.4.1 for details on R_{soil} measurements).

The average 3pm temperature is 22.9 °C (1993-2010) and average precipitation is 728.4 mm yr^{-1} (1994-2019) (Bureau of Meteorology, station 067105 in Richmond, NSW Australia, http://www.bom.gov.au). The soil at both sites comprises Holocene alluvium soil, with loamy sand in the upper 10-40 cm, underlain by sandy clay loam to clay (> 30% silt and clay) horizons, and permanent groundwater at 11 m below the soil surface.

4.3.2 Meteorological drivers

At AU-Cum, T_{air} and relative humidity were measured half-hourly using a HMP45C (Vaisala, Vantaa, Finland) sensor at 29 m height. T_{soil} was measured within 20 m of the flux tower half-hourly using a thermocouple buried at 5 cm depth (model TCAV, Campbell

Scientific, Logan, UT, USA). θ was monitored half-hourly at 5 cm depth using a CS616 probe (Campbell Scientific, Logan, UT, USA) installed horizontally.

At EucFACE, T_{soil} and θ were measured at six locations, within 1 m of auto-chambers measuring R_{soil}. T_{soil} and θ were measured every 15 minutes using a time-domain reflectometry probe (CS650-L; Campbell Scientific, Logan, UT, USA), and then averaged to 30 minutes to match the rest of the dataset timestamp. The 30 cm probe was inserted at 45° in the soil at the surface, measuring θ at 0 to 21 cm depth and T_{soil} was measured at 5 cm depth.

Rainfall was measured every half-hour using a tipping bucket (Tipping Bucket Rain gauge TB4; Hydrological Services Pty Ltd, Liverpool, NSW, Australia), located within 2 km of AU-Cum and EucFACE.

4.3.3 R_{eco} data

4.3.3.1 Night-time R_{eco} observations

R_{eco} was measured at night (sunset to sunrise) as:

$$R_{eco} = F_{CT} + F_{CS} \tag{4.1}$$

where F_{CT} is the vertical turbulent exchange of CO_2 (eddy-covariance method, (Baldocchi et al. 1988)), and F_{CS} is the change in storage of CO_2. The processing of high-frequency data to calculate F_{CT} was done with the EddyPro® open source software (LI-COR, Inc., Lincoln, NE, USA), keeping data that passed the quality control tests for stationarity and turbulence development (Foken et al. 2004) and met adequate signal strength for the infrared gas analyser (Renchon et al. 2018). The calculation of F_{CS} was done using a profiler system data, measuring CO_2 at 8 heights (Renchon et al. 2018); data were discarded if any of the inlets was not working. No clear friction velocity (u_*) threshold was found at the site (Figure S4. 1, R_{eco} was independent of u_* for a variety of T_{air} and θ bins). I further filtered out outliers, data

points above the 95% quantile (9.9 µmol m^{-2} s^{-1}) and below the 5% quantile (-3.3 µmol m^{-2} s^{-1}) of filtered data.

Using these quality checked criteria, I collected 15,686 R_{eco} observations over the 4-year period 2014-2017, out of a potential of 35,271 half-hourly night data (~45% of potential night data was kept). Of total night data, 17% had bad F_{CS} (problem with the pump, or with one or more inlets, or other issue), 17% had poor signal strength, 29% had bad qc.

4.3.3.2 R_{eco} gap-filling

Missing half-hourly R_{eco} data were filled using an ANN (using Levenberg-Marquardt algorithm and 15 hidden layers) built on high quality data (when qc = 0 or 1, signal strength is above threshold, and profiler data is available), with T_{air} and θ as drivers.

4.3.3.3 Nightly R_{eco}

I generated a gap-filled daily estimate of R_{eco} dataset by first estimating daily R_{eco} as the median of night half-hourly observations of R_{eco}, when at least 10 high quality half-hour measurements were available for a night. Then, to gap-fill missing days, if F_{CS} was missing, but 10 half-hourly observations of F_{CT} were available, daily R_{eco} was filled using an ANN with daily R_{eco} as target (calculated as described above) and F_{CT}, T_{soil}, θ, R_{soil}, and u_* as drivers (r^2 = 0.67). If F_{CS} and F_{CT} were missing, or <10 F_{CT} half-hourly observations were available, nightly R_{eco} was filled using an ANN with nightly R_{eco} as target and T_{soil}, θ, and R_{soil} as drivers (r^2 = 0.50).

4.3.4 R_{soil} data

4.3.4.1 Observations

I measured soil CO_2 efflux, hereafter referred to as R_{soil}, using automated chambers (20-cm diameter chamber, LI-8100-104 model and LI-8100A infra-red gas analyzers (IRGAs), LI-COR Environmental, Lincoln, NE, USA), at six different locations at EucFACE. The IRGAs

measured CO_2 concentration during 4.5 minutes, with a 30-s deadband and a postpurge, every half-hour during the 4-year period 2014-2017. The raw data were quality control (qc) checked with a threshold criterion of coefficient of variation (CV < 1.3) and coefficient of determination of the fit ($r^2 > 0.97$). Due to unavoidable mechanical issues, data collection was interrupted during some periods. In total, during the 4-years period, I collected 250 936 quality checked R_{soil} observations, out of a potential total of 420 768 (I kept 60 % of the data, 40% were missed due to mechanical interruption or qc check). From chamber one to chamber six, I collected 59%, 74%, 63%, 65%, 42% and 53% of potential data, respectively. Although three of the soil chambers were exposed to Free-Air CO_2 Enrichment (FACE), R_{soil} rates were not significantly affected by elevated CO_2 (Drake et al. 2018), so I included all six chambers in this analysis.

4.3.4.2 R_{soil} gap-filling

In order to get one continuous dataset of R_{soil}, I gap-filled the data for each of the six chamber separately, using a semi-mechanistic model (Dual Arrhenius Michaelis Menten or DAMM, (Davidson et al. 2012, Drake et al. 2018)).

The DAMM model is composed of a maximum potential rate of heterotrophic respiration, V_{max}, which is an exponential function of soil temperature, which is then potentially limited by the availability of C substrate (MM_{Sx}) or by oxygen (MM_{O2}). Those two limiting terms vary between 0 and 1, and are dependent on θ.

$$R_{soil} = V_{max}\, MM_{Sx}\, MM_{O2} \tag{4.2}$$

Vmax is a function of activation energy and soil temperature,

$$V_{max} = \alpha_{Sx}\, e^{-E_a/RT} \tag{4.3}$$

Were α_{Sx} is a pre-exponential factor, Ea is the activation energy, R is the universal gas constant (8.314), and T is soil temperature in Kelvins.

MM_{Sx}, the availability of C substrate, is a function of θ (m^3 m^{-3}).

$$MM_{Sx} = \frac{[S_x]}{kM_{Sx} + [S_x]} \tag{4.4}$$

$$[S_x] = [S_{xsoluble}]\ D_{liq}\ \theta^3 \tag{4.5}$$

$$[S_{xsoluble}] = p\ [S_{xtotal}] \tag{4.6}$$

Where kM_{Sx} is a Michaelis constant, $[S_{xsoluble}]$ is the amount of C substrate potentially soluble, which I assume to be a fraction (p = 0.024) of total soil C ($[S_{xtotal}]$= 0.0125 g cm^{-3}) (Drake et al. 2018), and D_{liq} is a diffusion coefficient of the substrate in liquid phase (D_{liq} = 3.17, dimensionless).

MM_{O2}, the oxygen limitation factor, is also a function of θ.

$$MM_{O2} = \frac{[O_2]}{kM_{O2} + [O_2]} \tag{4.7}$$

$$[O_2] = D_{gas}\ O_{2_{airfrac}}\ a^{4/3} \tag{4.8}$$

$$a = 1 - \frac{D_b}{D_p} - \theta \tag{4.9}$$

Where $[O_2]$ is oxygen concentration, kM_{O2} is a Michaelis constant, D_{gas} is the diffusion coefficient for O_2 in the air (D_{gas} = 1.67, dimensionless), $O_{2airfrac}$ is the volume of O_2 in the air ($O_{2airfrac}$ = 0.209), a is the air-filled soil porosity, D_b is soil bulk density (D_b = 1.53 g cm^{-3}) and D_p is particle density (D_p = 2.52 g cm^{-3}).

R_{soil} is then converted from mgC g^{-1} hr^{-1} to the same units as the measurements (Eq. 4.10 convert R_{soil} from mgC g^{-1} hr^{-1} to mgC m^{-2} hr^{-1}, then Eq. 4.11 convert from mgC m^{-2} hr^{-1} to μmol CO_2 m^{-2} s^{-1}) following:

$$Area_{Cflux} = 10^4\ Soil_d\ R_{soil} \tag{4.10}$$

$$R_{soil2} = Area_{Cflux}/10^3/12 \times 10^6/60/60 \tag{4.11}$$

where $Soil_d$ is soil depth ($Soil_d$ = 10 cm). For each chamber, I fitted the model (R_{soil2} fitted to 4 parameters: αsx, E_a, kM_{Sx} and kM_{O2}) to all the available quality checked data. I then obtained 6 parameter sets for the model (4 parameters for each of the 6 collars). I then used the model to fill the gaps for each chamber, using their respective parameter sets. Finally, I calculated the average from the 6 locations, using quality checked observation when available or chamber-specific gap-filled estimates when observations were not available.

4.3.5 R_{AG} estimation

I calculated nighttime R_{AG} as the difference between R_{eco} observations and R_{soil} observations:

$$R_{AG} = R_{eco} - R_{soil} \tag{4.12}$$

4.3.6 Seasonal and diel apparent temperature sensitivity

I estimated the apparent temperature sensitivity of R_{eco}, R_{soil} and R_{AG} by fitting an Arrhenius equation on monthly averages (seasonal apparent temperature sensitivity) and hourly averages (hourly apparent temperature sensitivity). I used Lloyd & Taylor equation, firstly established on R_{soil} (Lloyd and Taylor 1994), and later on R_{eco} (Desai et al. 2008).

$$R = R_{10} e^{E_0\left(\frac{1}{10+46.02} - \frac{1}{T+46.02}\right)} \tag{4.13}$$

Where R is either R_{soil}, R_{eco} or R_{AG}; R_{10} is a parameter fitted to data normalized to 10 °C, E_0 is another parameter fitted on data, defining the steepness of the curve, and T is either T_{soil} or T_{air}.

4.3.7 Alternate predictions of R_{eco} using R_{soil}

I used an ANN (Moffat et al. 2007) to constrain R_{eco} as a function of drivers: T_{soil}, T_{air}, θ, and R_{soil}. I used Levenberg-Marquardt algorithm, 15 hidden layers, and trained the network on 100% of the target data. First, I created 4 ANN, with the following drivers: 1) T_{air}, 2) T_{soil}, 3) T_{soil} and θ, and 4) T_{soil}, T_{air} and θ. Then, I created 4 more ANN by adding R_{soil} to these

drivers. I tested if the r^2 and RMSE (residual mean square error) of the fits were improved by adding R_{soil} to the other environmental drivers.

4.4 Results

4.4.1 Temporal dynamics of soil and ecosystem respiration and their drivers

During the 4-year period 2014-2017, the mean annual precipitation was 856 mm yr^{-1} and the mean T_{air} was 18.5 °C. On average, precipitation was higher in summer (289 mm) than winter (186.5 mm), but precipitation was quite aseasonal, with some dry periods (e.g. first half of 2014, only 287 mm, or 50 mm in Autumn 2016) and wet periods (e.g. 345 mm in Autumn 2015 or 335 mm in Winter 2016). T_{soil} had a low spatial variability, as opposed to θ and R_{soil} (Figure 4.1c, grey shade barely visible). Average night-time T_{soil} varied between 10 °C (6 July 2015) and 27 °C (12 February 2017) (Figure 4.1c). Across the six locations, θ had a large spatial variability (Figure 4.1b, grey shade), with different locations drying faster after rain events, probably due to spatial variation in soil properties. Median nightly R_{soil} ranged from 1.6 µmol m^{-2} s^{-1} on average in winter (June through August) to 3.7 µmol m^{-2} s^{-1} in summer (December through February), while median nightly R_{eco} ranged from 2.0 µmol m^{-2} s^{-1} in winter to 4.6 µmol m^{-2} s^{-1} in summer (Figure 4.1a). R_{eco} and R_{soil} had a similar seasonal time dynamic, with R_{eco} being slightly higher than R_{soil} (Figure 4.1a). R_{soil} had a large spatial variability in warm, moist conditions (Figure 4.1a, grey shade shows range across six collars).

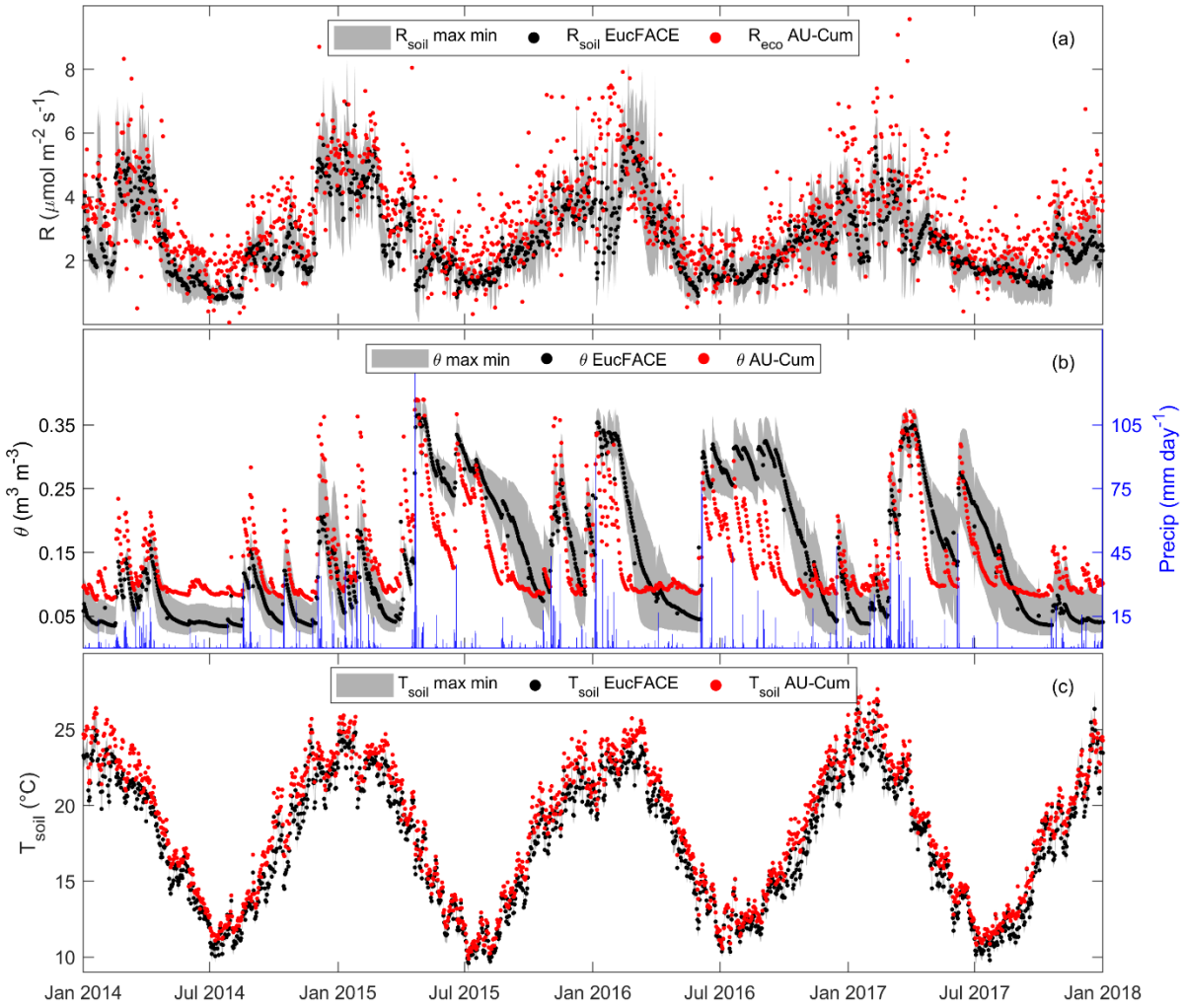

Figure 4.1 Time series of daily ecosystem respiration, soil respiration, soil moisture and soil temperature over the 2014-2017 period. Time series over the 4 years period 2014-2017 of nightly (n = 1462 days) (a) Median respiration fluxes: black dots: EucFACE soil respiration (R_{soil}, gap-filled as in 4.3.4.2), red dots: AU-Cum ecosystem respiration (R_{eco}, gap-filled as in 4.3.3.3), (b) soil moisture (θ) in shallow layer (5cm for the flux site and 0-21cm for EucFACE) and daily precipitation and (c) soil temperature (T_{soil}) at 5cm depth. Black dots are the average of the 6 chambers or sensor, grey shade indicates the range of values across six chambers or sensors. Red dots are the median of nighttime AU-Cum data.

4.4.2 R_{soil} and R_{eco} response to T_{soil} and θ with the DAMM model

Nightly median and half-hourly R_{soil} observations were both explained very well by the semi-mechanistic heterotrophic respiration DAMM model (half-hourly: $r^2 = 0.65$, RMSE = 0.86. Night median: $r^2 = 0.69$, RMSE = 0.82. Figure 4.2 and Table 4.1). R_{eco} night median was well explained by DAMM ($r^2 = 0.50$, RMSE = 1.05), but the fit quality was much lower against half-hourly observations (R_{eco}: $r^2 = 0.10$, RMSE = 2.43, (Table 4.1, Figure 4.2)). The DAMM model parameters for R_{eco} were similar to those determined for the individual soil chambers at both time scales (Figure 4.2, Table 4.1).

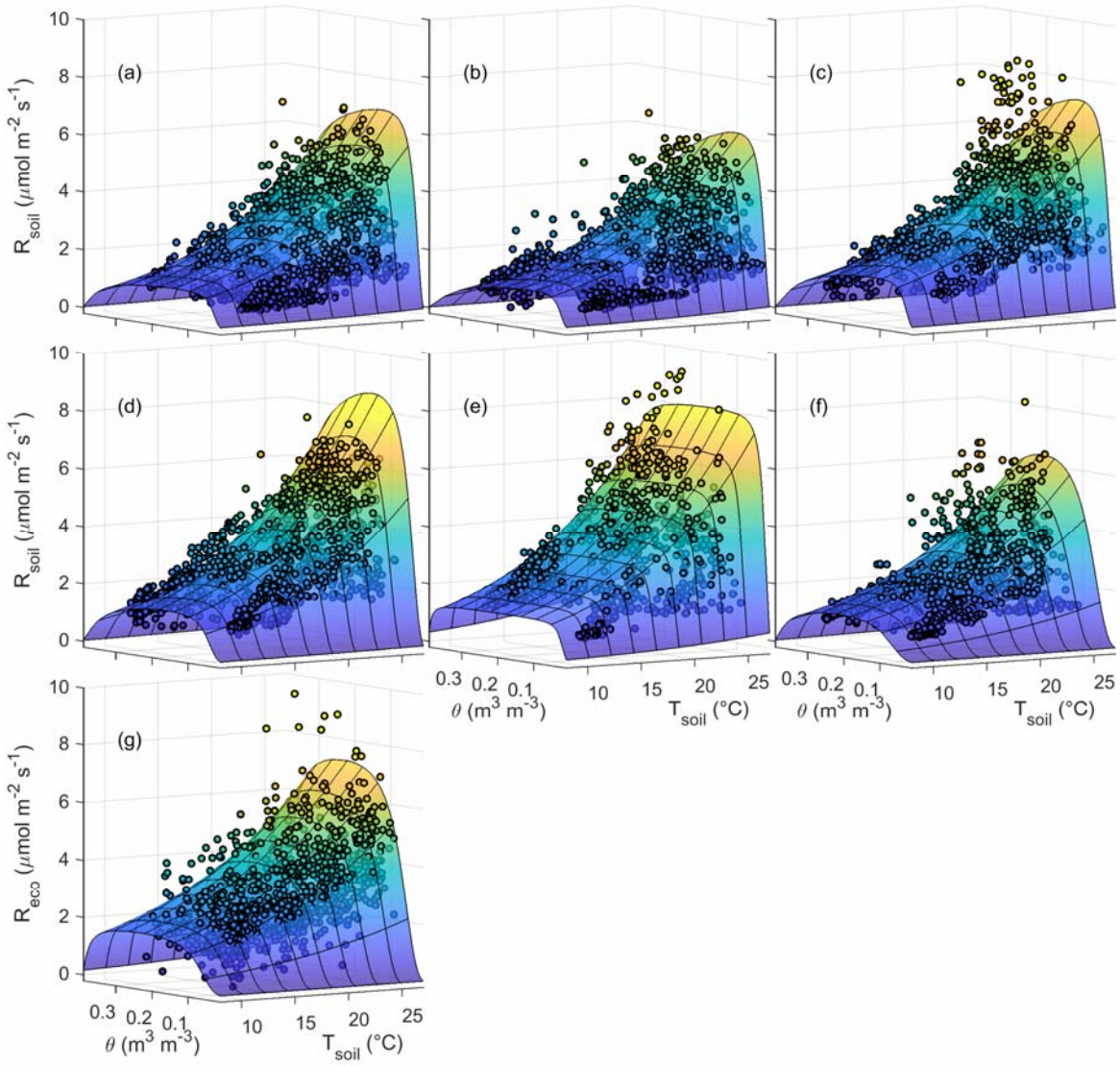

Figure 4.2 Daily (night median) response of soil respiration (a-f) and ecosystem respiration (g) to soil temperature and soil moisture, and Dual-Arrhenius Michaelis Menten (DAMM) model fit. Values of fitted parameters and quality of fit are reported in Table 4.1. Only measurements are used in to fit the model (no gap-filled data).

4.4.3 Seasonal and diurnal pattern of R_{soil}, R_{eco} and R_{AG}

R_{eco} and R_{soil} had a similar seasonal pattern and followed the seasonal pattern of T_{air} and T_{soil}, with R_{eco} have a higher magnitude (Figure 4.3a, Figure 4.4a,c). Note that because Figure 4.3a values were night monthly medians, T_{soil} was higher than T_{air}. R_{AG} had a lower seasonal amplitude, but also peaked in summer months (Figure 4.3a, Figure 4.4e). T_{soil} and T_{air} had a similar diurnal course (Figure 4.3b), reaching maximum values around 3 pm and minimum around 6 am, but the diurnal amplitude of T_{air} was much larger than diurnal amplitude of T_{soil} (1.6 °C for T_{soil} and 8.0 °C for T_{air}) (Figure 4.3b). R_{soil} was relatively flat diurnally, with a diurnal amplitude of 0.23 μmol m^{-2} s^{-1} for an average R_{soil} rate of 2.4 μmol m^{-2} s^{-1} (Figure 4.3b, Figure 4.4b). R_{eco} had a large amplitude over the available observation range (7pm to 6am), with an amplitude of ~ 1.8 μmol m^{-2} s^{-1} for an average R_{eco} rate of ~ 2.7 μmol m^{-2} s^{-1} (Figure 4.3b, Figure 4.4d). As a result, R_{AG} had a large diurnal amplitude too (Figure 4.3b, Figure 4.4f).

The apparent temperature response differed between monthly and hourly time resolution. For R_{soil}, the monthly apparent temperature response was higher than the hourly apparent temperature response (Figure 4.4a,b). For R_{eco}, the monthly apparent T_{soil} response was much lower than the hourly apparent T_{soil} response, but the monthly apparent T_{air} response was similar to the hourly apparent T_{air} response (Figure 4.4c,d). For R_{AG}, both T_{soil} and T_{air} monthly apparent response were much lower than hourly apparent temperature response (Figure 4.4e,f).

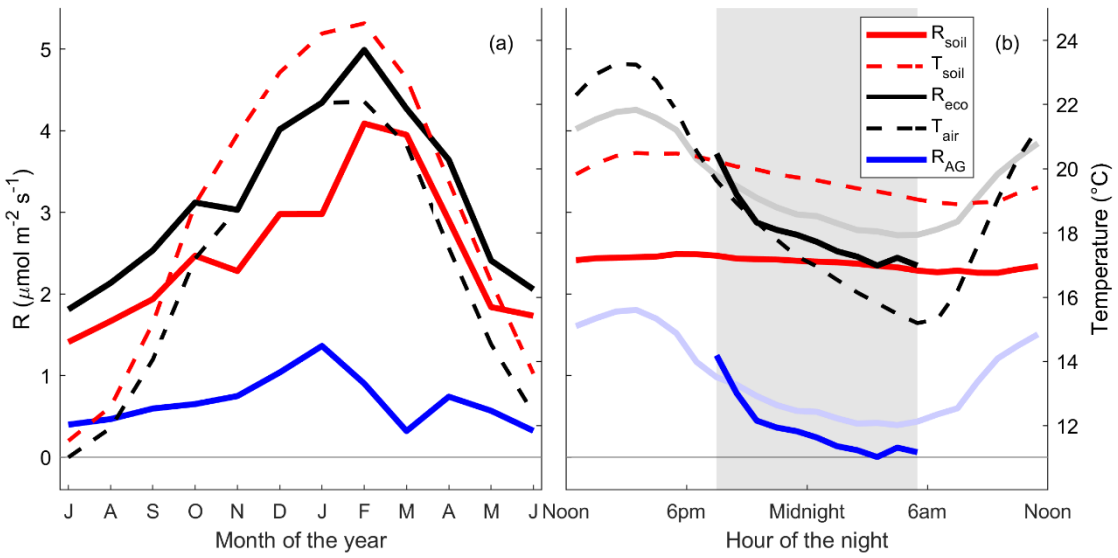

Figure 4.3 Seasonal and diurnal pattern of observed simultaneous soil respiration, ecosystem respiration, above-ground respiration, soil temperature and air temperature. Temporal patterns of (a), monthly median of half-hourly nighttime data (sunrise to sunset), and (b) diurnal pattern of hourly median of half-hourly data. Data shown: soil respiration (R_{soil}), ecosystem respiration (R_{eco}), above-ground respiration ($R_{AG} = R_{eco} – R_{soil}$), soil temperature ($T_{soil}$) and air temperature ($T_{air}$). Data over the 4-year period 2014-2017 were used. In (a), all half-hourly observation of quality controlled R_{eco} (see 4.3.3.1) and gap-filled R_{soil} for the same subset as R_{eco}. In (b), only observations of R_{soil} and R_{eco} are used to plot the bold colors (nighttime), the grey line is modelled R_{eco} (as in 4.3.3.2), day and night, and the light blue line is modelled R_{AG} (modelled R_{eco} – gap-filled R_{soil}). The grey shade represents nighttime.

.

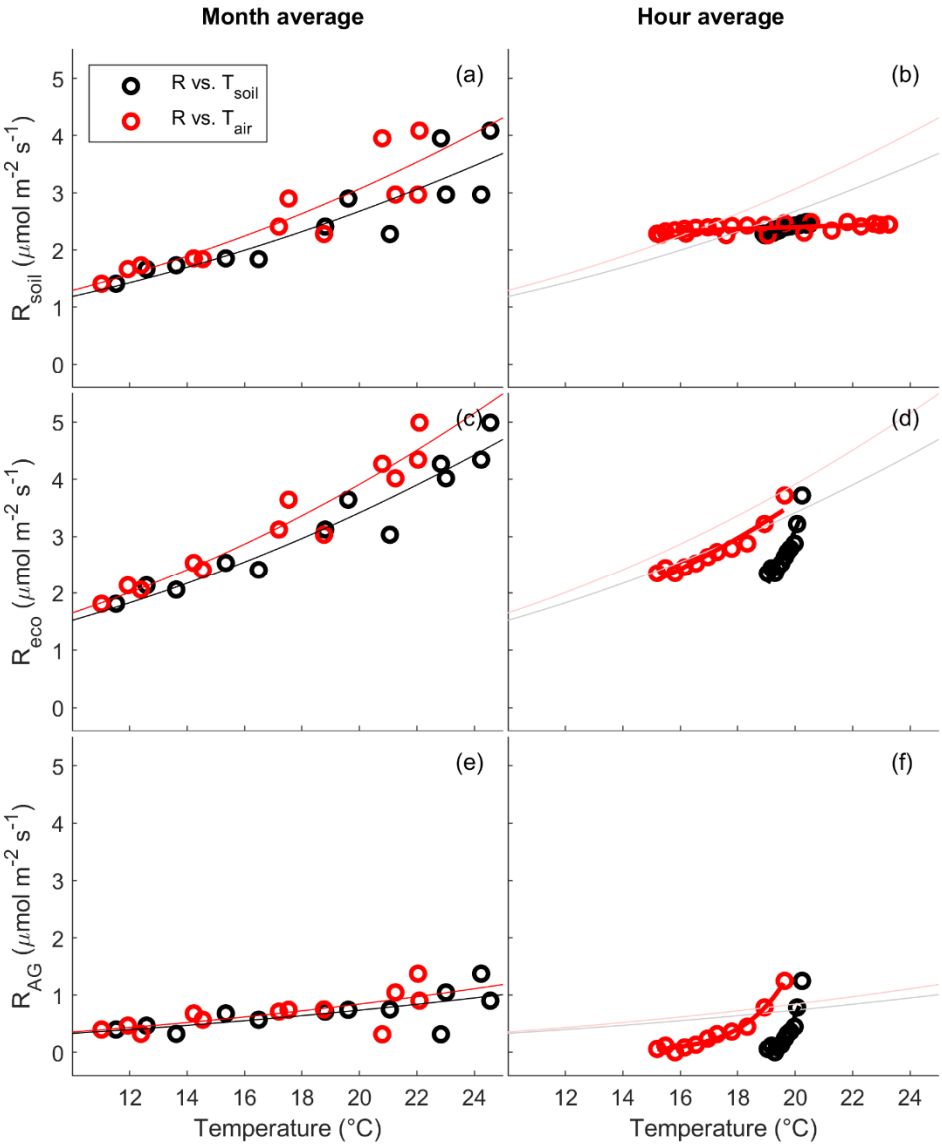

Figure 4.4 Apparent seasonal and diurnal temperature responses of observed ecosystem and soil respiration and estimated above-ground respiration, fitted to the Lloyd and Taylor (1994) equation. Apparent seasonal (monthly median, n=12) and diurnal (hourly median, n=11 (R_{eco}) or n=24 (R_{soil})) temperature responses (Lloyd and Taylor 1994) of ecosystem respiration (R_{eco}), soil respiration (R_{soil}), and above-ground respiration (R_{AG}). Hourly and monthly medians were calculated when both R_{soil} and R_{eco} observations were simultaneously available. (a, c, e) monthly average of soil temperature (T_{soil}) and air temperature (T_{air}) versus monthly median of R_{soil} (a), R_{eco} (c) and R_{AG} (e). (b, d, f) hourly median of T_{soil} and T_{air} versus hourly average of R_{soil} (b), R_{eco} (d) and R_{AG} (f). For comparison, lines from (a, c, e) and shown in panels (b, d, f) with lighter color. Parameter values and quality of fit are reported in Table 4.2.

4.4.4 Constraining R_{eco} using R_{soil} and implications for gap-filling

Predictions of R_{eco} based on half-hourly data were poor, with r^2 below 0.13 and RMSE above 2.4 µmol m^{-2} s^{-1}, but the predictions of daily R_{eco} (night median) were much more accurate (Table 4.3), with r^2 up to 0.58 and RMSE about 1 µmol m^{-2} s^{-1}. The ANN model including R_{soil} together with T_{air}, T_{soil} and θ predicted nighttime R_{eco} better than other models tested (Table 4.3). Using R_{soil} to inform ANN to constrain estimates of R_{eco} slightly improved estimates of R_{eco}, r^2 increased by up to 0.02 at half-hourly scale to 0.12 on daily scale (Table 4.3). The DAMM model predicted R_{eco} with similar skill as the best ANN models, whereas the LT model performed worse than models that incorporated θ. On daily time resolution, LT gave an r^2 of up 0.39 (with T_{soil}) and DAMM 0.50.

Annual R_{eco} (gap-filled as explained in 4.3.3.2) was 1329 ± 39 gC m^{-2} yr^{-1} over the 4-year period 2014-2017, and annual R_{soil} (gap-filled as explained in 4.3.4.2) was 986 ± 66 gC m^{-2} yr^{-1} over that same period. R_{soil} was 74% of R_{eco}. Using higher u_* threshold to filter R_{eco} data did not increase annual budget of gap-filled R_{eco} (Figure S4. 2). However, using only three hours after sunset of night data (as recommended in (Van Gorsel et al. 2007)) did increase annual budget of R_{eco} from 1300 gC m^{-2} yr^{-1} to 1520 gC m^{-2} yr^{-1} (calculated by gap-filling nightly R_{eco}, presented in 4.3.3.3, using an ANN with T_{soil} and θ as drivers).

Table 4.1 Fitted parameters values and quality of fit of the semi-mechanistic heterotrophic respiration model Dual Arrhenius Michaelis Menten (DAMM) fitted to night-time observation of R_{soil} and R_{eco}, using half-hourly night data or median of night data with at least 10 half-hours, over the 4-year period 2014-2017.

Data time resolution	Fit to	Fitted parameters				r^2	RMSE	n
		α_{Sx}	Ea	kM_{SX}	kM_{O2}			
half-hourly	R_{soil} 1	$5.1\ 10^{8}$	64	$3.5\ 10^{-8}$	$5.9\ 10^{-3}$	0.69	0.79	41462
	R_{soil} 2	$8.5\ 10^{6}$	54	$2.6\ 10^{-8}$	$1.2\ 10^{-2}$	0.62	0.80	52079
	R_{soil} 3	$1.3\ 10^{6}$	49	$3.2\ 10^{-8}$	$6.9\ 10^{-3}$	0.66	0.89	44283
	R_{soil} 4	$1.2\ 10^{8}$	60	$1.2\ 10^{-7}$	$6.2\ 10^{-3}$	0.72	0.84	46082
	R_{soil} 5	$3.8\ 10^{7}$	58	$3.0\ 10^{-8}$	$2.9\ 10^{-4}$	0.67	0.94	29569
	R_{soil} 6	$1.1\ 10^{6}$	49	$5.0\ 10^{-7}$	$4.0\ 10^{-3}$	0.53	0.89	37461
	R_{eco}	**$5.1\ 10^{4}$**	**42**	**$2.5\ 10^{-7}$**	**$1.2\ 10^{-3}$**	**0.10**	**2.43**	**15686**
Nightly average	R_{soil} 1	$1.2\ 10^{9}$	66	$3.3\ 10^{-8}$	$5.5\ 10^{-3}$	0.74	0.72	1073
	R_{soil} 2	$2.2\ 10^{8}$	62	$2.3\ 10^{-8}$	$1.1\ 10^{-2}$	0.69	0.71	1116
	R_{soil} 3	$2.7\ 10^{7}$	57	$3.1\ 10^{-8}$	$9.2\ 10^{-3}$	0.72	0.85	1037
	R_{soil} 4	$6.1\ 10^{8}$	64	$1.1\ 10^{-7}$	$6.5\ 10^{-3}$	0.78	0.72	1017
	R_{soil} 5	$1.1\ 10^{9}$	66	$1.3\ 10^{-8}$	$4.6\ 10^{-4}$	0.63	1.08	727
	R_{soil} 6	$6.9\ 10^{7}$	59	$5.0\ 10^{-7}$	$4.4\ 10^{-3}$	0.59	0.83	869
	R_{eco}	**$4.5\ 10^{6}$**	**52**	**$3.6\ 10^{-7}$**	**$1.5\ 10^{-3}$**	**0.50**	**1.05**	**933**

Table 4.2 Parameter values (E_0 and R_{10} and quality of fit (r-square)) of Lloyd and Taylor fitted on monthly or half-hourly ecosystem respiration, soil respiration and above-ground respiration. The monthly median and hourly median of R_{soil}, R_{eco} and R_{AG} vs. T_{soil} and T_{air}. Observations (not gapfilled estimates) over 2014-2017 were used to calculate medians.

Component	Temperature	**Month medians (n = 12)**			**Hour average (n = 24 or 11)**		
		E_0	**R_{10}**	**R^2**	**E_0**	**R_{10}**	**R^2**
R_{soil}	T_{soil}	301	1.19	0.80	235	1.28	0.93
	T_{air}	319	1.29	0.80	29	2.22	0.36
R_{eco}	T_{soil}	299	1.52	0.93	1626	0.04	0.86
	T_{air}	319	1.65	0.93	402	1.21	0.91
R_{AG}	T_{soil}	294	0.33	0.47	7459	0.00	0.84
	T_{air}	318	0.36	0.48	2836	0.00	0.98

Table 4.3 Quality of fit (R^2) of models fitted on night-time observation of ecosystem respiration (R_{eco}), using half-hourly night data or median of night data with at least 10 half-hours, for different driver sets. R-square Δ shows the improvement of models when using the same drivers and soil respiration (R_{soil}) as an additional driver.

	Model	Drivers	R^2	R^2 Δ	RMSE	RMSE Δ
half-hourly (n = 15686)	LT	T_{air}	0.08		2.45	
	LT	T_{soil}	0.08		2.46	
	DAMM	T_{soil}, θ	0.10		2.43	
	ANN	T_{air}	0.09		2.45	
	ANN	T_{soil}	0.09		2.45	
	ANN	T_{soil}, θ	0.10		2.43	
	ANN	T_{soil}, T_{air}, θ	0.11		2.41	
	ANN	R_{soil}	0.09		2.45	
	ANN	R_{soil}, T_{air}	0.11	0.02	2.42	-0.03
	ANN	R_{soil}, T_{soil}	0.10	0.01	2.43	-0.02
	ANN	R_{soil}, T_{soil}, θ	0.11	0.00	2.42	-0.01
	ANN	R_{soil}, T_{soil}, T_{air}, θ	0.12	0.00	2.41	-0.01
	ANN	6 R_{soil}, 6 θ, T_{soil}, T_{air}	0.12		2.40	
Average night-time (n = 933)	LT	T_{air}	0.36		1.18	
	LT	T_{soil}	0.39		1.16	
	DAMM	T_{soil}, θ	0.50		1.05	
	ANN	T_{air}	0.37		1.18	
	ANN	T_{soil}	0.41		1.13	
	ANN	T_{soil}, θ	0.53		1.01	
	ANN	T_{soil}, T_{air}, θ	0.55		0.99	
	ANN	R_{soil}	0.44		1.11	
	ANN	R_{soil}, T_{air}	0.50	0.13	1.05	-0.12
	ANN	R_{soil}, T_{soil}	0.49	0.08	1.06	-0.08
	ANN	R_{soil}, T_{soil}, θ	0.55	0.02	1.00	-0.02
	ANN	R_{soil}, T_{soil}, T_{air}, θ	0.57	0.01	0.98	-0.02
	ANN	6 R_{soil}, 6 θ, T_{soil}, T_{air}	0.58		0.96	

4.5 Discussion

4.5.1 Seasonal and diurnal patterns of R_{soil}, R_{eco} and R_{AG}

Over the period 2014-2017 at the Cumberland Plain TERN-OzFlux site, R_{soil} contributed to 76.9% of R_{eco}. The seasonal amplitude of R_{eco} was mostly influenced by R_{soil} via T_{soil}, and the diurnal amplitude of R_{eco} was mostly influenced by R_{AG} via T_{air} (Figure 4.3a,b). This result challenges the idea that R_{soil} can be used as a proxy of the diurnal pattern of R_{eco} (as suggested in (Reichstein et al. 2005) or (Desai et al. 2008)), at least in the warm, temperate ecosystem studied, where the diurnal amplitude of R_{soil} was often negligible. The diurnal amplitude of R_{soil} varies considerably between and within biomes and climate, from low to large diel variations of R_{soil} (Jian et al. 2018). Because R_{AG} was determined by difference, its diurnal pattern was similar to R_{eco}. This result calls for a better understanding of R_{AG} diurnal pattern, which is composed of stem respiration and leaf respiration.

4.5.2 Bias of nighttime and daytime ecosystem respiration by standard methods?

4.5.2.1 Nighttime

A known problem of eddy-covariance is the assumption of horizontal flux divergence (also named advection flux) being negligible in the mass balance (see equation 1). For this assumption to be reasonable, the standard method is to filter out data when advection is assumed to be important. This method is called u_* filter method (Aubinet et al. 2000), and relies on the idea that nighttime NEE should not depend on friction velocity, since it is not a driver for ecosystem respiration. It is usually observed that NEE within a narrow range of temperature and soil moisture increases or decreases with u_* at values below a certain threshold. This threshold can be determined with an algorithm such as the change point detection method (Barr et al. 2013). Data below this threshold should be discarded and then gap-filled.

Without applying this method, nighttime R_{eco} would usually be under-estimated, as advection may lead to loss of CO_2, however at AU-Cum, annual budget of Reco did not increase with increasing u_* threshold (Figure S4. 2). Studies still question if this method is reliable and suggest alternative methods, such as using early night data only (3 hours after sunset (Van Gorsel et al. 2007)), or using intercept of light response from daytime data (Lasslop et al. 2010), or attempting to quantify a missing flux from storage measurements and advection (Hayek et al. 2018).

At the Cumberland Plain site, there was no clear dependence of nighttime NEE with friction velocity (Figure S4. 1), and thus filtering and gap-filling nighttime data at low u_* did not change integrated R_{eco} (Figure S4. 2). This result could mean that there is no advection at our site, or that advection occurred but was not dependent on u_*. R_{eco} was, however, much larger early in the night compared to late at night, as shown in Figure 4.3b, and this high NEE early night was mostly the result of high F_{CS}, as F_{CS} decreased overnight while F_{CT} remained relatively flat (Figure S4. 5). Also, F_{CS} was larger than F_{CT} in magnitude. This result highlights the importance of F_{CS} in capturing both the magnitude and pattern of R_{eco} at night. As a result, using 3 hours after sunset data did change the annual budget of R_{eco} (from 1300 gC m^{-2} yr^{-1} on average when using all night data, to 1520 gC m^{-2} yr^{-1} on average when using only three hours after sunset). The importance of storage and advection fluxes is known to vary from site to site; although advection is usually low at sites such as ours with low slope (Aubinet et al. 2005), it can remain important at such sites: in a study (McHugh et al. 2017), advection accounted for 40% of the nighttime underestimation of R_{eco} by turbulent flux only (the remaining 60% being change in storage).

4.5.2.2 Daytime

Daytime R_{eco} is inferred from the apparent temperature response of nighttime NEE. This method assumes that R_{eco} nighttime temperature response is similar to its daytime response.

Wehr et al. (2016) attempted to directly measure daytime R_{eco} using stable isotopes and showed that daytime R_{eco} estimate from the standard LT temperature response method was over-estimated. The authors of the study suggested that the mismatch was likely caused by light inhibition of leaf respiration (Wehr et al. 2016). Light inhibition could cause an over-estimation of daytime R_{eco} by up to 25% in comparison to using standard methods (Keenan et al. 2018, Keenan et al. 2019).

Our analysis suggests another possibility (other than, or in addition to, light inhibition) causing an over-estimation of daytime R_{eco}. The apparent temperature response of R_{eco} may result from a systematic bias, as advection may co-vary with temperature, both decreasing overnight (Van Gorsel et al. 2007). This artefact would result in an over-estimation of daytime R_{eco} estimates even without inhibition of leaf respiration and must be considered.

The seasonal contribution of R_{eco} components has been estimated using low time resolution measurements (monthly) or using modelling (Law et al. 1999), but to our knowledge no study has attempted to measure continuously all R_{eco} components as the relative contribution of R_{soil}, stem respiration (R_{stem}) and leaf respiration (R_{leaf}) to R_{eco} at hourly temporal resolution. Such an analysis would be invaluable to reconcile estimates of daytime ecosystem respiration, by quantifying the potential over-estimation of R_{eco} by inhibition of R_{leaf} (for example, if R_{leaf} represents 10% of R_{eco}, light inhibition can only reduce R_{eco} by up to 10%). Moreover, R_{soil}, R_{stem} and R_{leaf} respond to different temperature (soil temperature, stem temperature and leaf temperature) and are lagged in time, and thus have distinct diurnal patterns. Improving understanding of component contributions to diurnal patterns of R_{eco} will improve ecosystem models, with important consequences for estimating ecosystem C uptake.

4.5.3 Modelling R_{eco} using the DAMM model

The good capacity of the DAMM to model R_{eco} encourages the use of this or similar models for eddy-covariance gap-filling and also for R_{eco} models, as it has the advantage of using mechanisms and is thus transferable and more insightful than a neural network. It was more skilful in predicting R_{eco} than the commonly used LT model, which is based only on temperature (albeit fitted to 15-day windows it incorporates some implicit moisture dependency; Reichstein et al. 2005). However, DAMM is based on assumptions relating to substrate diffusion to microbes in soils, and its applicability at the ecosystem scale is likely to depend on the relative importance of soil vs. aboveground respiration.

4.6 Conclusions

I evaluated the contribution of soil CO_2 efflux to seasonal and diurnal dynamics of ecosystem respiration. Our results showed large seasonal and diurnal amplitude of R_{eco}, and large seasonal but low diurnal amplitude of R_{soil}, implying that above-ground respiration was the key determinant of R_{eco} diurnal pattern.

I introduced the use of a semi-mechanistic heterotrophic respiration model (DAMM) to predict and gap-fill R_{eco} and show that its predictive power is similar to artificial neural network, encouraging its potential use for other sites. I showed that adding R_{soil} as a driver for ANN slightly improved its predictive power of R_{eco}. I also used with good results an ANN to gap-fill daily (night median) NEE when storage flux was missing and when both storage flux and turbulent flux were missing, by using R_{soil} measurements in addition to T_{air}, T_{soil} and θ. This shows valuable use of R_{soil} to gap-fill R_{eco}.

I discussed the possible over-estimation of daytime respiration estimates by standard methods as presented in the literature, possibly caused by light inhibition of leaf respiration, and introduced a new possible explanation as the result of a systematic bias, where advection may

covary with temperature, both decreasing overnight (Van Gorsel et al. 2007) and leading to a falsely large apparent temperature response.

5 Chapter 5. Conclusions

5.1 Most important results

In the second chapter, I showed how the Cumberland Plain woodland acted as a net sink of carbon in winter, and as a net source of carbon in summer. This unusual pattern contrasted with two flux tower sites in other Australian evergreen broadleaf forests, Tumbarumba and Wombat, where net uptake occurred all year long and particularly in summer (Keith et al. 2012, Hinko-Najera et al. 2017b). Cumberland Plain's seasonal pattern was the result of a larger seasonality of R_{eco} compared to GPP, therefore R_{eco} explained most of the seasonality of NEE. This, in turn, could be explained by large respiration rate in summer during wet and hot conditions, with lower respiration rate in winter, when conditions were colder and drier. GPP was limited in summer due to stomatal regulation at high D and remained quite high (albeit a bit lower) in winter with good photosynthesis conditions. I also found that seasonal variations in leaf area index were correlated with photosynthetic capacity variations. Leaf area index increased rapidly mid-summer, peaked late summer, and then decreased slowly until the next year, and the optimum canopy carbon assimilation followed these variations.

In the third chapter, I used CABLE, a land surface model, to test the ability of the model to reproduce the unusual seasonal pattern observed in the data, and to analyse the importance of leaf area index according to the model. I modified the model in order to force LAI to be either constant or variable. I also analysed the phenology of leaf area index and estimated the monthly allocation of NPP to leaf growth under the assumption that no stored carbon was used to grow leaves. I found that leaf area index annual maxima were bigger and occurred earlier when summer rainfall was important, and vice versa. The model was able to reproduce the seasonality of NEE (net sink in winter, net source in summer). In the model, NPP had two peaks, in autumn and in spring, as NPP was limited by radiation in winter and by stomatal regulation at high D in summer. The model GPP was lower than the flux tower estimate,

especially in autumn, when observed leaf area index and photosynthetic capacity were maximum. I think that this may result from not accounting for leaf demography in the model, as mature leaves are known to have a higher photosynthetic capacity than young or old leaves. Allocation of NPP to leaves was dynamic which could mean that trees used carbon reserves in summer if GPP was constrained by high VPD. According to the model, and also to the four-year data set, inter-annual variability of NEE was not related to mean temperature or annual precipitation but was positively correlated with mean LAI.

In the fourth chapter, I studied the contribution of soil CO_2 efflux to ecosystem respiration. I compared half-hourly nighttime data of R_{soil} and R_{eco} over a 4-year period (2014-2017). I tested the ability of a semi-mechanistic model of heterotrophic respiration (DAMM) to reproduce R_{soil} and R_{eco} as a function of soil or air temperature and soil moisture, as well as artificial neural network using similar drivers. The DAMM model was an excellent predictor of R_{eco} at daily (nightly) scale, as good as predicting daily R_{soil}. Overnight patterns of R_{eco} and R_{soil} were distinct; R_{soil} was relatively flat overnight compared to R_{eco}, which decreased overnight as temperature decreased. As a result, overnight pattern of R_{eco} had to be driven by above-ground respiration or could result from a systematic data bias (advection fluxes occurring later at night despite standard data filtering). R_{eco} seasonal pattern was similar to that of R_{soil}. The change in storage component of NEE CO_2 mass balance equation (see equation 1.1) was very important at our site, contributing to more than 50% of NEE measurement at night and in the morning, and about 20% during daytime.

5.2 Recommended measurements and analysis for better constraints of fluxes in evergreen broadleaf forests in Southeast Australia

Our analysis mostly relied on four years of data from a single site, which allowed us to study in detail the fluxes at hourly to seasonal time resolution. In the third chapter, I started to analyse inter-annual variability according to a model. More years of data will allow

evaluation of inter-annual variability in more detail (Aubinet et al. 2018, Baldocchi et al. 2018).

Our analysis identified leaf demography as an important factor of seasonal and inter-annual fluxes variability. I therefore encourage measurements of leaf-level gas-exchange, to obtain as leaf parameters as a function of leaf age (Reich et al. 2009, Wu et al. 2016a, Wujeska-Klause et al. 2019). The ability of leaf demography to improve modelling of observed fluxes could then be tested using the same methods as presented in chapter 3 with CABLE and LAI.

I showed how our estimate of monthly allocation of NPP to leaf growth was dynamic, which contrasts with usual assumptions in the CABLE LSM that this allocation factor is constant. I therefore encourage studies to analyse allocation patterns and the use of carbon reserves to grow leaves (Smith 2018, Furze et al. 2019).

I observed that overnight patterns of R_{soil} did not match those of R_{eco}, but due to known issues of nighttime measurements of net ecosystem exchange (Van Gorsel et al. 2007), I had to question whether this result was biological or a result of advection. I therefore encourage continuous high frequency (hourly) measurements of R_{eco} components, such as leaf respiration and stem respiration, to complement measurements of soil respiration, to observe if the decrease of R_{eco} overnight can be explained by a decrease of above-ground respiration overnight. Furthermore, the result of such an analysis would have implications as to the validity of the apparent temperature response of R_{eco} overnight, and therefore if estimates of daytime R_{eco} are over-estimated because of this bias. Recent studies suggest that we do over-estimate daytime R_{eco}, but suggest this is mostly the result of light inhibition of leaf respiration (Wehr et al. 2016, Keenan et al. 2018, Keenan et al. 2019). To decipher whether current daytime R_{eco} estimates are accurate, over-estimated due to night measurement bias, or over-estimated due to light inhibition of leaf respiration, I encourage continuous

measurements of component respiration at hourly frequency during day and night in the footprint of flux towers.

The long term (50 – 100 years) change of Cumberland Plain ecosystem services (such as carbon and water exchange) may be mainly caused by changes in mortality and species present in the forest, which our observations and modelling can't predict. Tracking tree mortality and what mechanism causes it will help. Also, tracking species shifts will allow to better understand what mechanism causes it. The nearby CO_2 enriched forest (EucFACE) experiment may be useful to understand the effect of increasing atmospheric CO_2 at the Cumberland Plain site.

I encourage the use of remotely sensed indices (NDVI, EVI, LAI, GRACE, …), and the use of indices of soil drought. Also, I encourage comparison of our measurements with other sites, particularly nearby similar forests (Tumbarumba, Wombat, Warra, Whroo), and modelling these sites, to understand how they differ and why. In general, I encourage the use of our dataset for broader synthesis and therefore have made it available on the OzFlux data portal (http://www.ozflux.org.au/).

6 Supplementary information

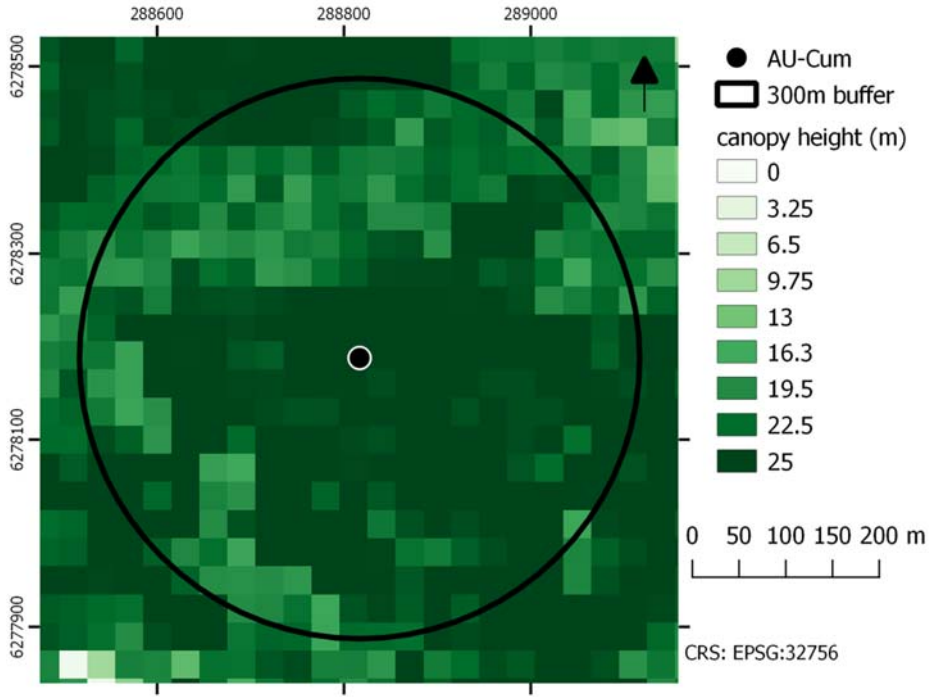

Figure S2. 1. Canopy height model at AU-Cum site, generated at 30m spatial resolution using LiDAR data. The average canopy height was calculated to be 24.01m. Credits: Daniel Metzen

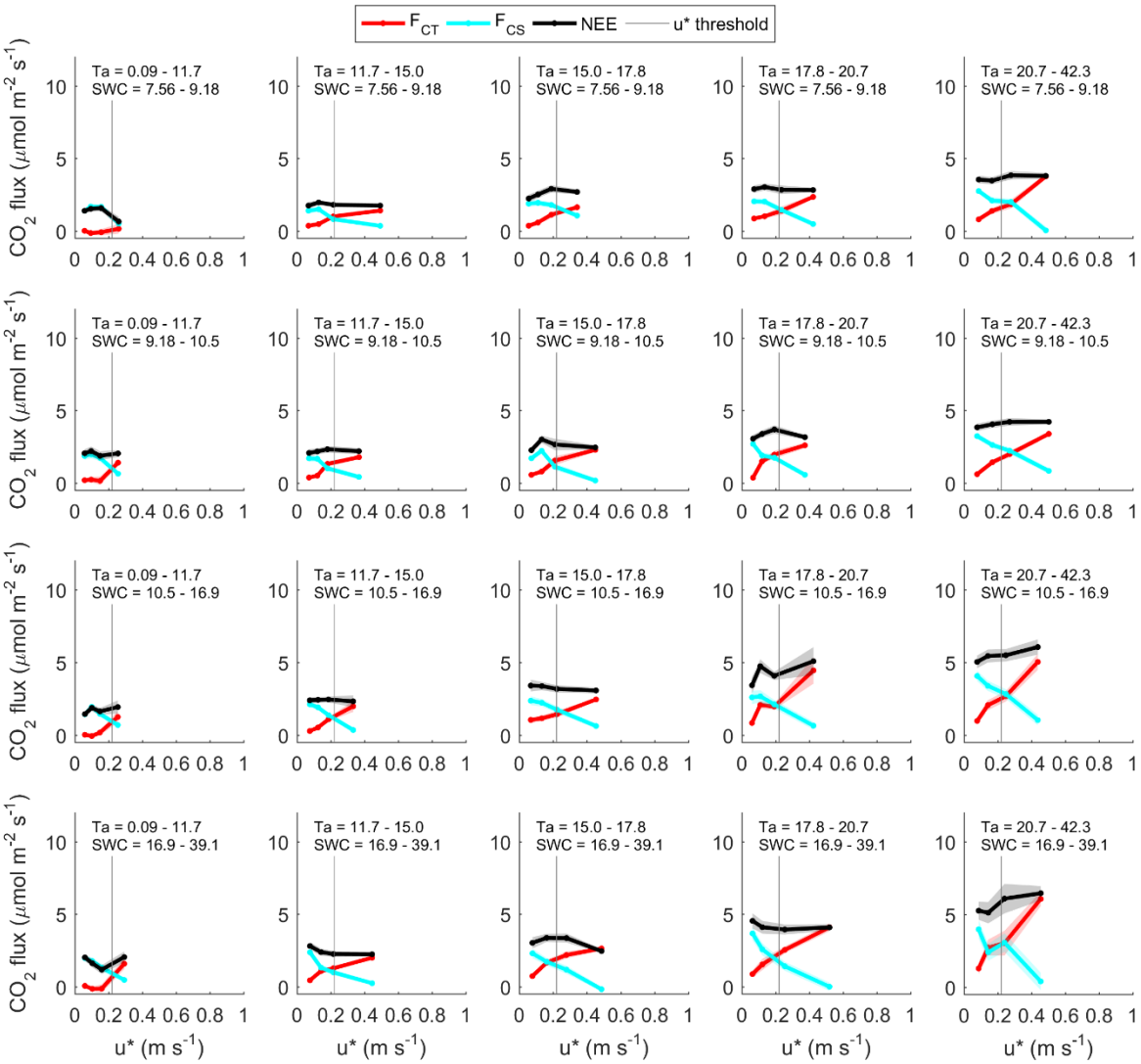

Figure S2. 2. Nighttime net ecosystem exchange, vertical turbulent exchange and change in storage vs. friction velocity, for 5 air temperature quantiles and 4 soil moisture quantiles. Nighttime NEE (black), F_{CT} (red) and F_{CS} (cyan) vs. friction velocity (u_*), per air temperature (T_a, left to right) and soil moisture quantiles (SWC, top to bottom). Actual values of T_a and SWC quantiles are shown in the figure. The vertical grey line show the u_* threshold chosen to be conservative (no threshold detected using change point detection as NEE vs. u_* was relatively flat for most T_a and SWC bins).

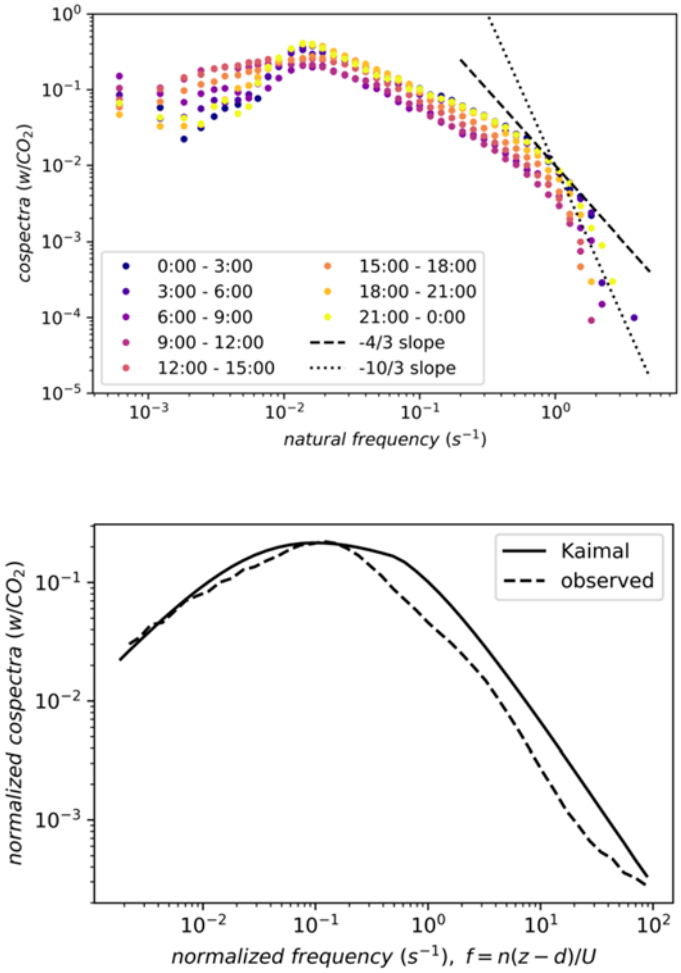

Figure S2. 3. Vertical wind and CO_2 concentration cospectra, and comparison with the Kaimal model, using 2014-2017 data. Top panel: 3-hourly binned w/CO_2 cospectra at AU-Cum. I observed the expected minor deviation from the 'ideal' -4/3 slope to a -10/3 slope in the high frequency domain due to the path length difference of the sonic anemometer and the IRGA (Burba 2013).

Bottom panel: comparison with the Kaimal model (Kaimal et al. 1972) did show the typical behaviour of tall towers. Observed CO_2 cospectras fall below the Kaimal model in the mid to high frequencies as expected for tall towers, where some noise might be present in the signal. These figures demonstrate that the reported fluxes are compliant with typical eddy covariance systems and hence are representative for the investigated ecosystem. Credits: Daniel Metzen

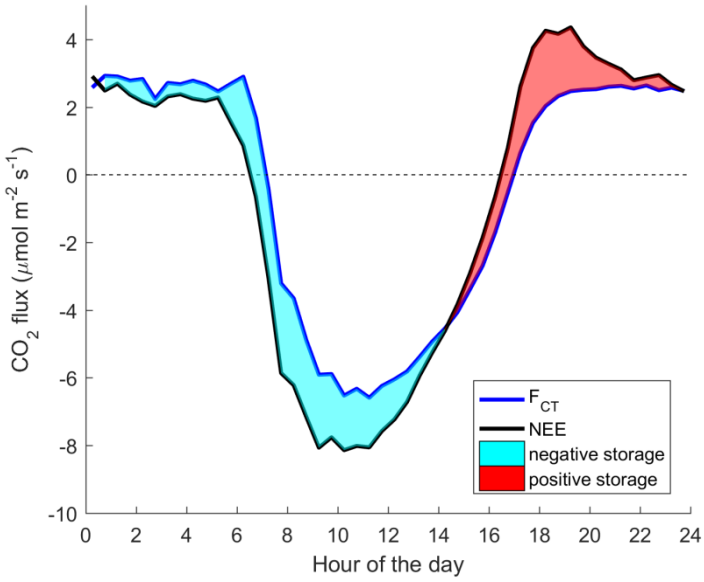

Figure S2. 4. Diurnal course of all measured, quality checked and u∗ filtered net ecosystem exchange of CO_2 (NEE) and CO_2 vertical turbulent exchange (F_{CT}). The shading shows the change in storage term of the conservation of mass balance (F_{CS}, equation 1), cyan shading shows negative F_{CS} (CO_2 inside the control volume is decreasing) and red shading shows positive F_{CS} (CO_2 inside the control volume is increasing). Note that the storage flux is very impactful on fluxes during sunrise and sunset; not accounting for storage would drastically bias light response parameters.

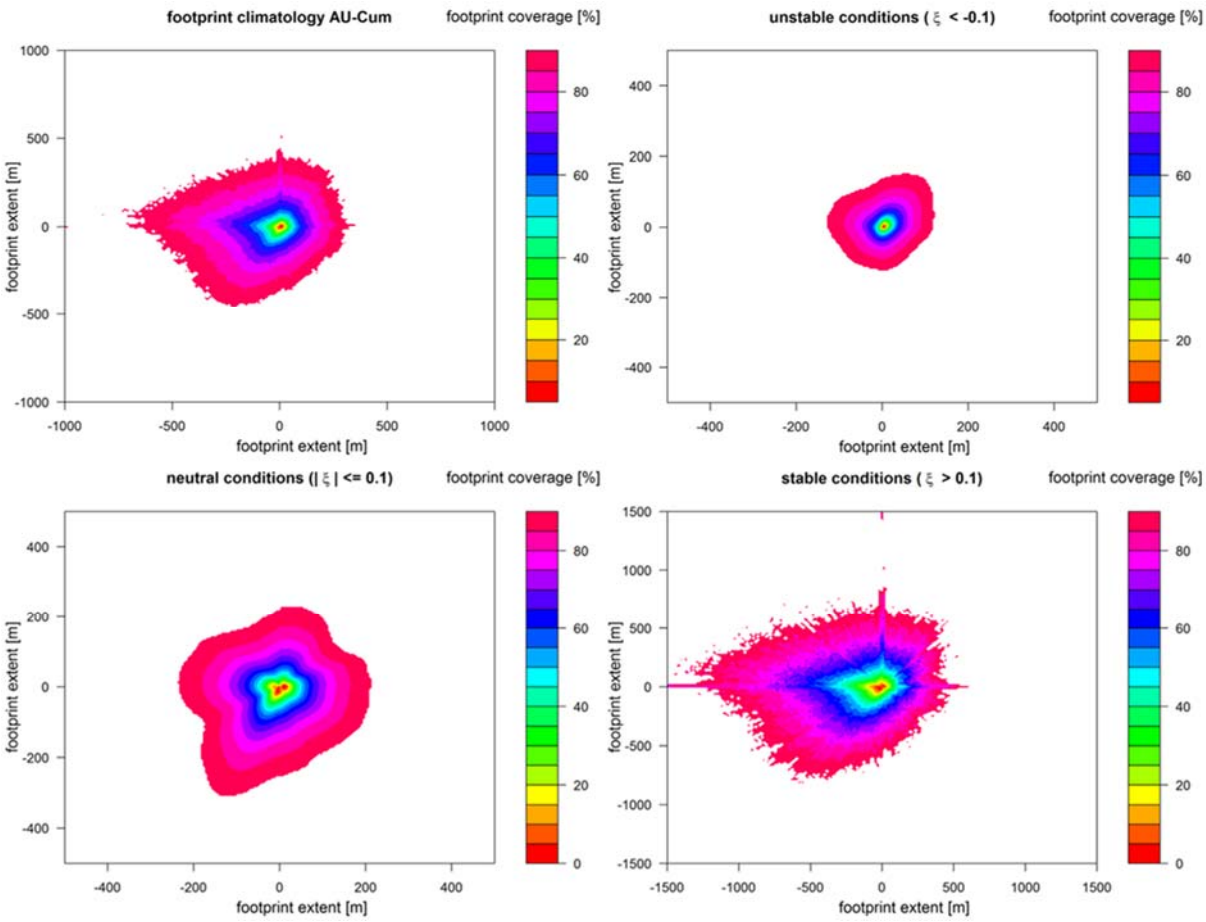

Figure S2. 5. Footprint climatology at AU-Cum site, for all data, unstable, neutral and stable conditions. (Kormann and Meixner 2001) model was used, the figure was produced using FREddyPro package in R. Color show the footprint coverage in % (cumulative), up to 90%. Note that the x-axis and y-axis scales (footprint extent, in m) change between subplots, as under stable conditions the footprint extends further from the tower. Credits: Anne Griebel.

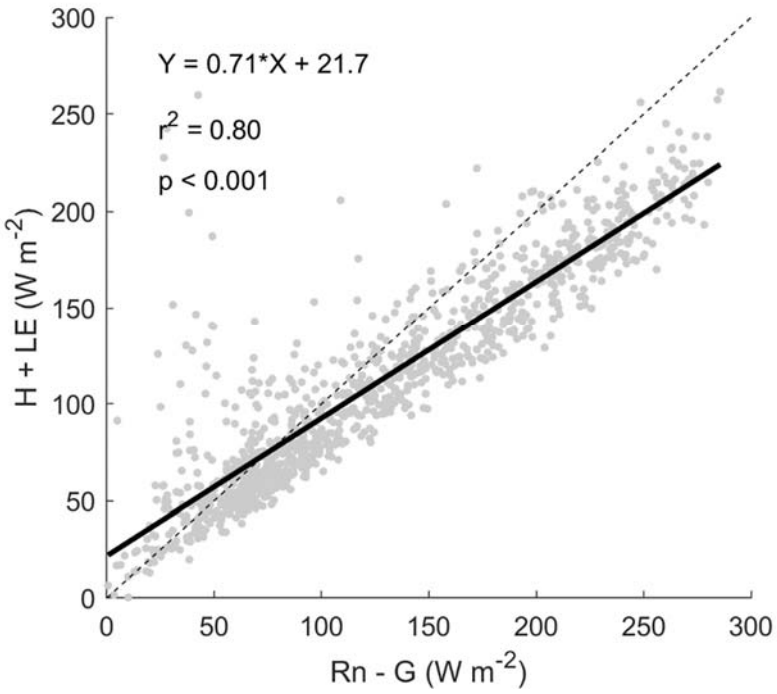

Figure S2. 6. Energy balance closure (sensible + latent heat flux vs. net radiation - ground heat flux), daily data from 2014 through end of 2016. The black dotted line shows 1 to 1 line, the solid line shows linear regression (y = 0.7x + 16), r^2 = 0.85. Note that the closure deficit, about 30%, is comparable to what is obtained on most forested sites.

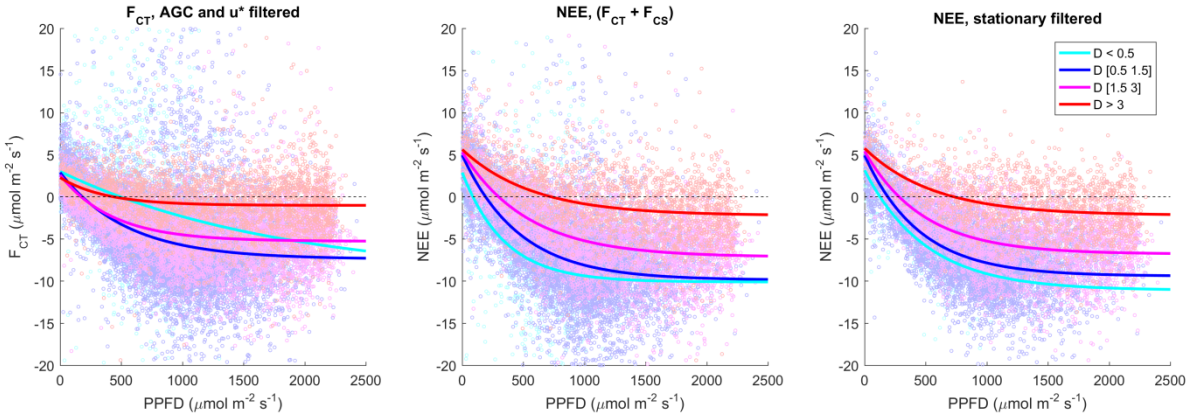

Figure S2. 7. Light response of F_{CT}, NEE, and NEE after stationarity filter, colored by D. Line shows light response curve fits (Mitscherlich (1909); Eq. 5). Note that accounting for the change in storage flux (F_{CS}) is necessary for constraining light response parameters correctly; light response parameters using F_{CT} can lead to negative R_d or low D limiting photosynthesis, both are incoherent. Stationarity filter enhances the quality of NEE data. These two steps are particularly important under low D conditions (e.g., at sunrise, when PAR ~ 0, where data constrain both R_d and α).

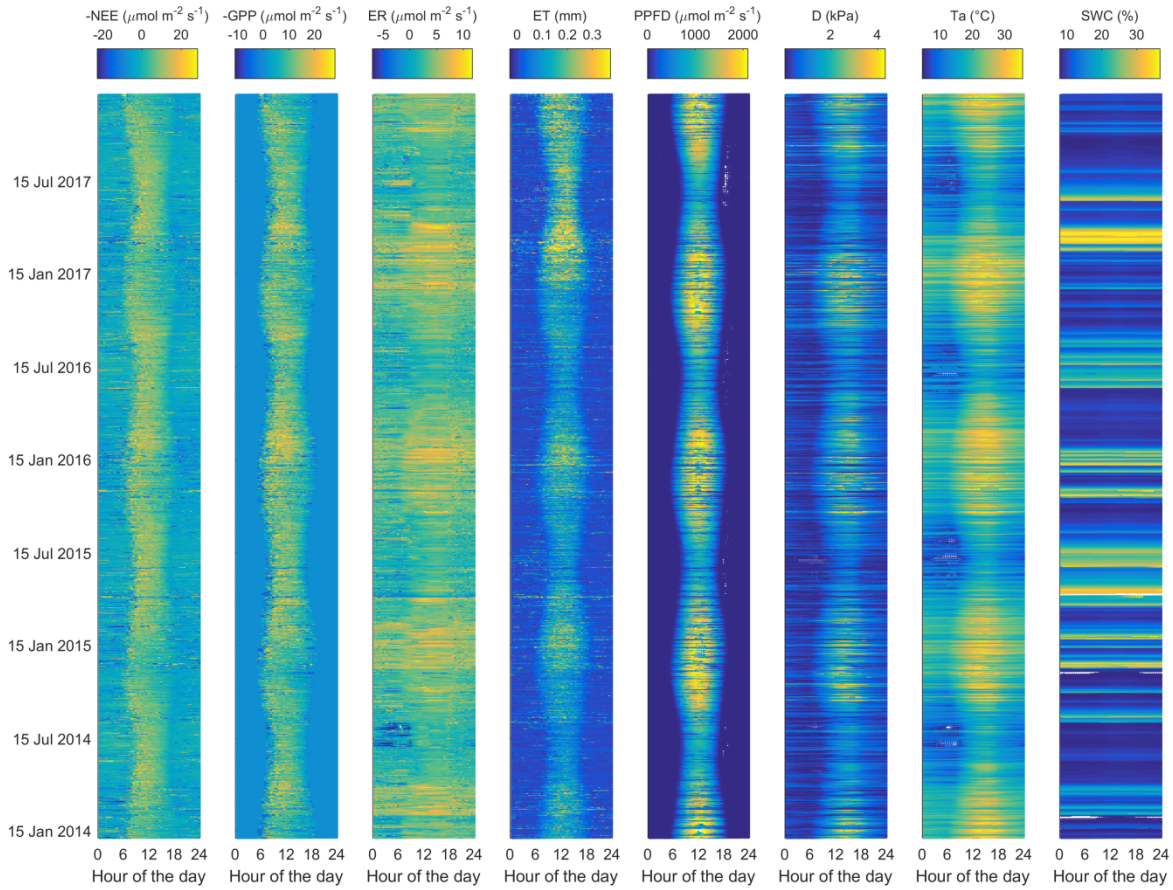

Figure S2. 8. Time series (bottom: January 2014, top: January 2017) and diurnal course of fluxes and environmental drivers over the three years of the study. Note the reduced NEE and GPP in the afternoon during summer, despite estimated R_{eco} being higher (which would increase estimated GPP). Note the shorter day length and light intensity in winter. 98% of the data (> 0.01 quantile and < 0.99 quantile) is shown, in order to filter extreme value impacts on color-axis range.

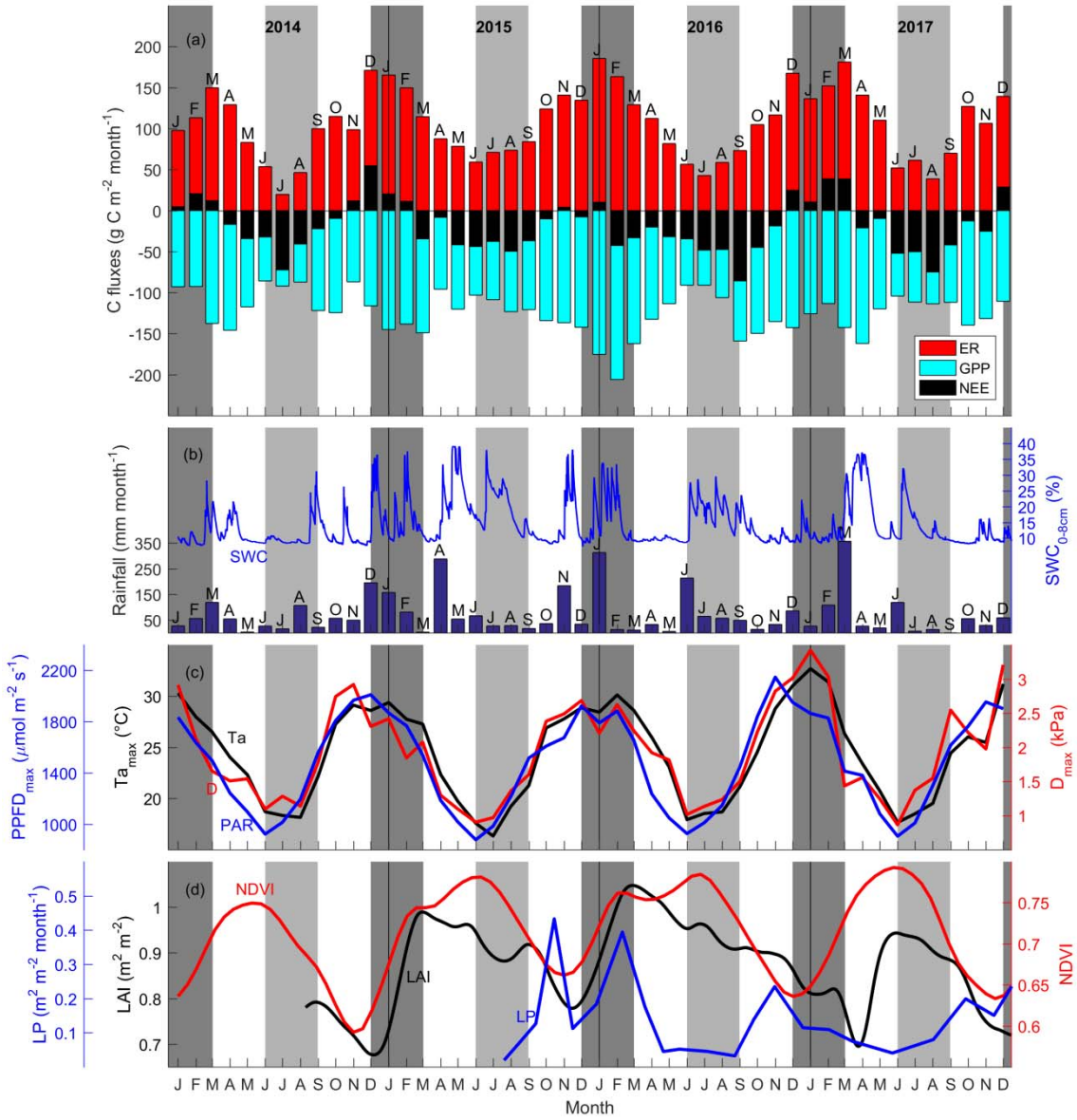

Figure S2. 9. Similar to figure 2.1, but with NDVI instead of EVI in panel (d). a) Time series of monthly carbon flux (net ecosystem exchange (NEE), ecosystem respiration (R_{eco}) and gross primary productivity (GPP), g C m^{-2} $month^{-1}$) (negative indicates ecosystem uptake); b) rainfall, mm $month^{-1}$; soil water content from 0 to 8 cm ($SWC_{0\text{-}8cm}$, %); c) average of daily maximum for each month photosynthetically active radiation ($PPFD_{max}$, µmol m^{-2} s^{-1}), air temperature (Ta_{max} , °C) and vapour pressure deficit (D_{max}, kPa)]. Canopy dynamics trends [normalised difference vegetation index (NDVI, unitless); d) leaf area index (LAI, m^2 m^{-2}) from November 2013 to April 2016 and litter production (LP, m^2 m^{-2} $month^{-1}$)]. Shaded areas

shows summer (dark grey) and winter (light grey). Note Ta_{max} and $PPFD_{max}$ remained above 15 °C and 800 µmol m^{-2} s^{-1}.

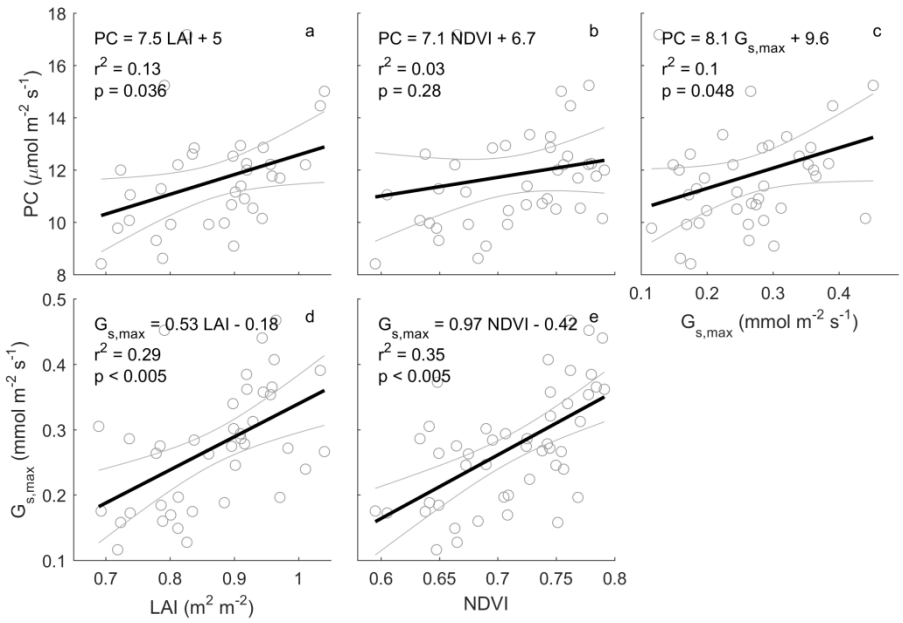

Figure S2. 10. Similar to figure 2.6, but with NDVI instead of EVI. Relationships between monthly photosynthetic capacity (PC, µmol m^{-2} s^{-1}), leaf area index (LAI, m^2 m^{-2}), 250 m^2 normalised difference vegetation index (NDVI), and maximum surface conductance ($G_{s,max}$). Monthly PC / $G_{s,max}$ are calculated as the median / 75% quantile of half-hourly GPP / G_s when PPFD [800-1200 µmol m^{-2} s^{-1}] and D [1-1.5 kPa]; rain events are filtered for $G_{s,max}$ estimation, to minimise evaporation contribution to evapotranspiration (see methods). Monthly LAI is calculated as mean of LAI smoothed by a spline. Thick black line shows a linear regression. For PC calculation, GPP data is only used when quality-checked NEE is available (GPP = NEE measured – R_{eco} estimated by a neural network, see method).

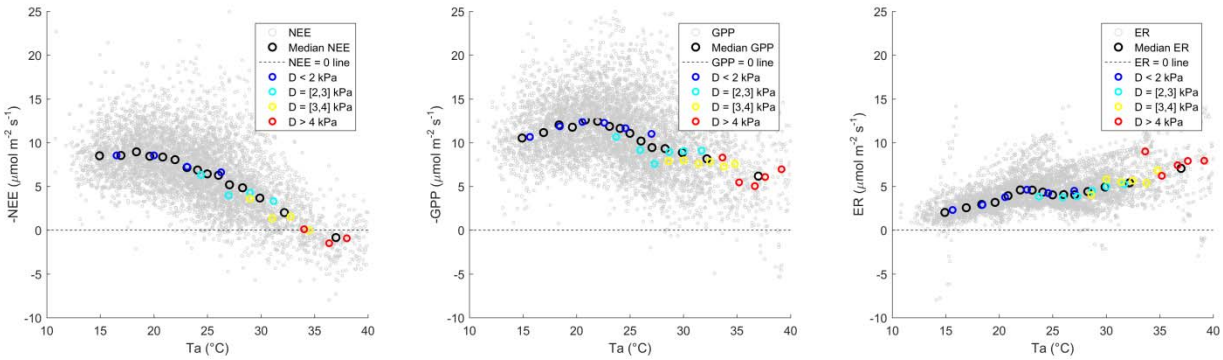

Figure S2. 11. Light-saturated (photosynthetically active radiation (PAR) > 1000 µmol m^{-2} s^{-1}) C-fluxes: net ecosystem exchange (NEE), gross primary productivity (GPP) and ecosystem respiration (R_{eco}, from SOLO) versus air temperature. Grey dots are half-hourly measurements; black dots are C-flux for 15 T_a bins of equal sized n; colored dots are C-fluxes for 4 T_a bins within a D bin. Maximum light-saturated GPP rates occur around 22 °C, NEE becomes negative (net C source) at light saturation above 35 °C.

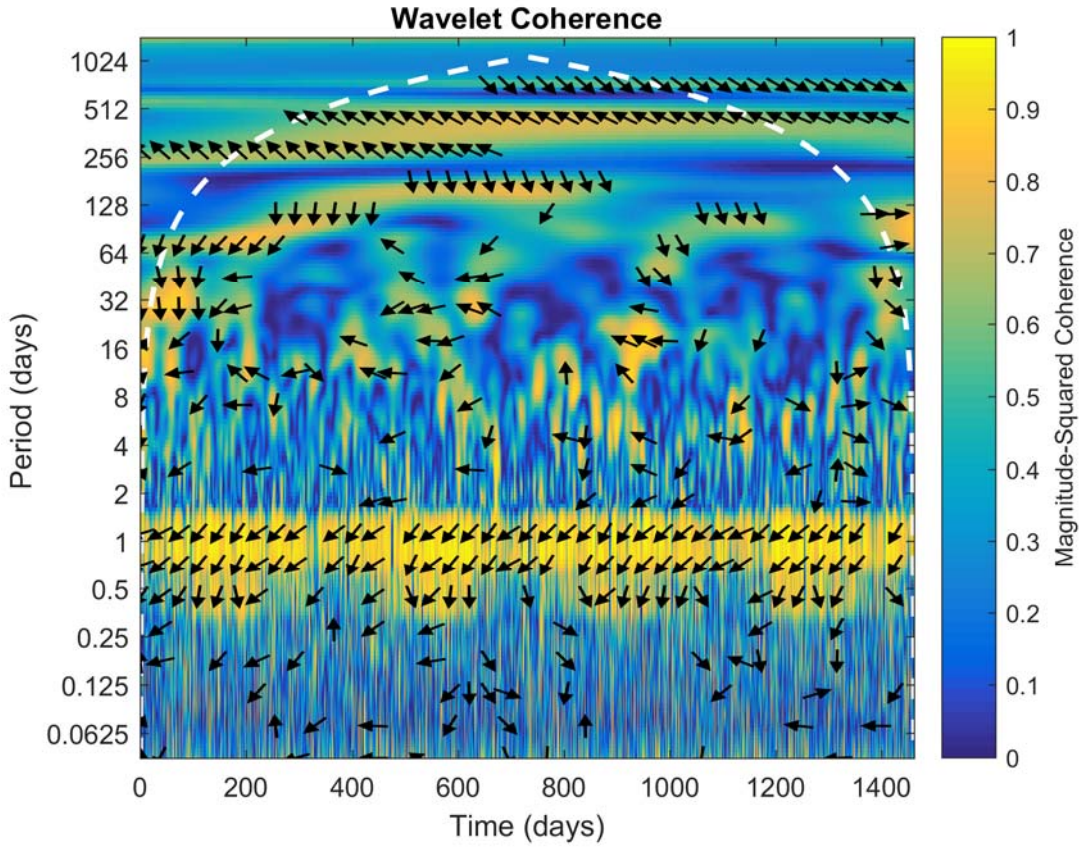

Figure S2. 12. Wavelet coherence between D and GPP, for the four year study (2014 through 2017). The arrows represent the difference in phase between D and GPP for the specific time and period. Daily coherence is evident, which is expected as diurnal of D and GPP follow day/night cycle, the lag is due to GPP peaking around noon, while VPD peaks around 3pm. Similarly, annual coherence is high, as D and GPP are high in summer, low in winter. Some incursion of hot weather creates weekly coherences in summer, as GPP decreases when D increases.

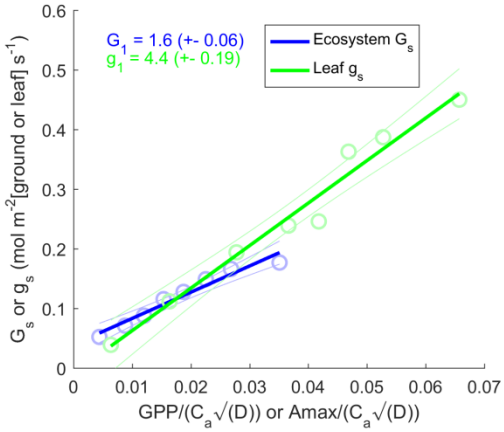

Figure S2. 13. G_s or g_s vs. GPP or Amax/√D. g_1 and G_1 are estimated by solving equation (S1) or (S2) below. Eddy-covariance data filtered out periods after rain events (see surface conductance methods) in order to minimise contribution of soil evaporation to ET. G_s and g_s datasets are binned into 8 bins of equal size. Leaf-level data were measured at a site within 1.5km of the flux tower (Gimeno et al. 2016). Note the discrepancy between leaf level and ecosystem level g_1 and G_1, discussed in a recent study (Medlyn et al. 2017), where G_1 was found to be larger than g_1, which is opposite to our result.

$$G_s = G_0 + 1.6 \cdot \left(1 + \frac{G_1}{\sqrt{D}}\right) \frac{GPP_{max}}{400} \tag{S1}$$

$$g_s = g_0 + 1.6 \cdot \left(1 + \frac{g_1}{\sqrt{D}}\right) \frac{A_{max}}{400} \tag{S2}$$

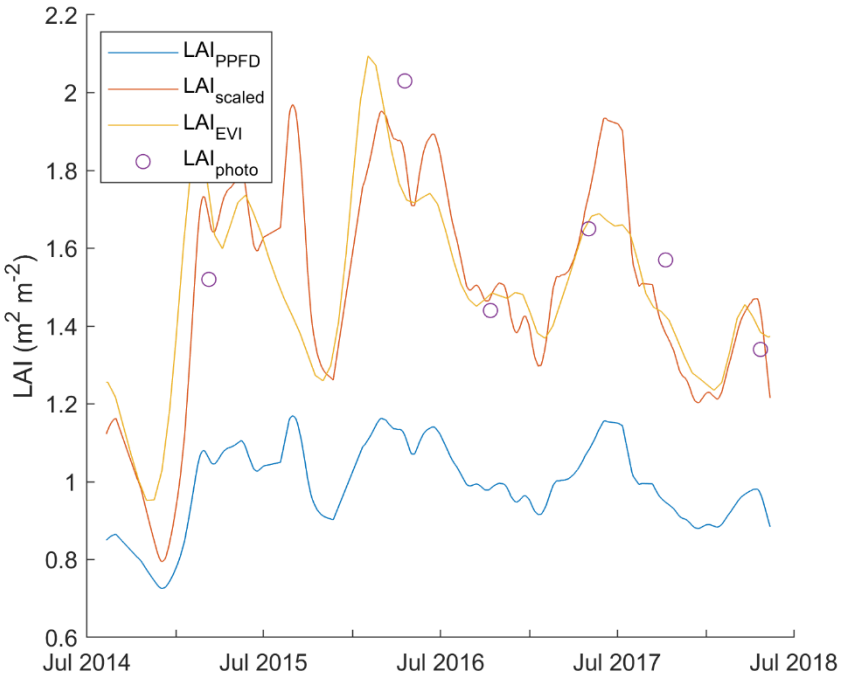

Figure S3. 1. Comparison of estimates of LAI at the Cumberland Plain site. Blue line (LAI_{PPFD} smoothed), data estimated from continuous measurements of above-canopy incident and understorey photosynthetic photon flux density (F_{PPFD}). Data are averaged across three sensors. Purple dots (LAI_{photo}), LAI estimated from canopy photography using MacFarlane method (Macfarlane et al. 2007). Data are means of ~ 200 LAI estimates from upward photography taken on 6 dates. Red line (LAI_{scaled}), LAI_{PPFD} scaled on LAI_{photo} (linear regression of LAI_{PPFD} vs. LAI_{photo}, $r^2 = 0.6$, $p = 0.07$, $n = 6$, equation: $LAI_{scaled} = 2.65\ LAI_{PPFD} - 1.13$). Yellow line: LAI estimated from enhanced vegetation index (EVI) (linear regression of LAI_{scaled} vs. EVI, $r^2 = 0.68$, $p << 0.005$, equation: $LAI_{EVI} = 11.95\ EVI – 2.34$).

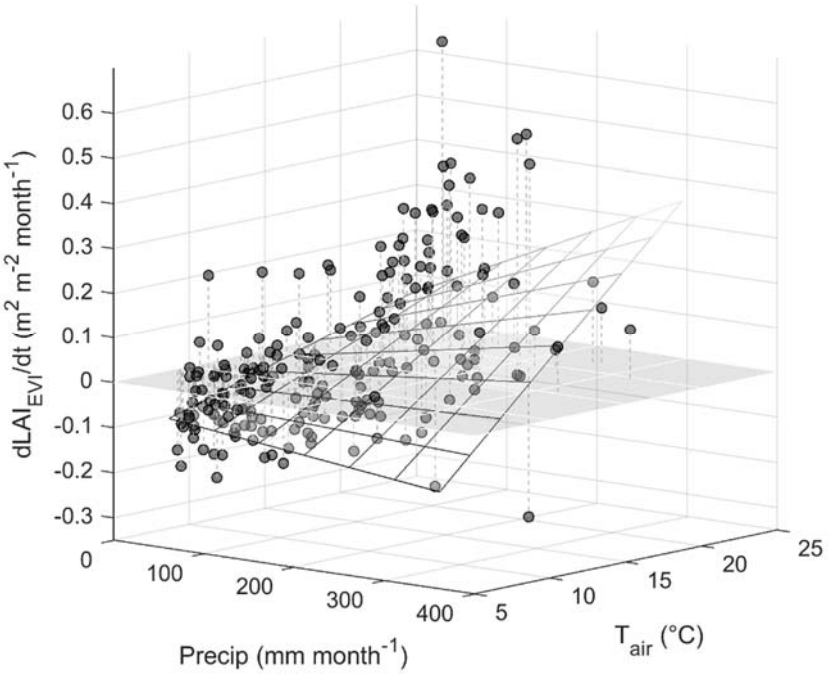

Figure S3. 2. Monthly change in leaf area index over time ($dLAI_{EVI}/dt$, $m^2\ m^{-2}\ month^{-1}$) as a function (multiple linear regression) of monthly precipitation (Precip, mm $month^{-1}$) and monthly average air temperature (T_{air}, °C). Regression fit: $r^2 = 0.29$, $p < 0.005$, $n = 214$. $dLAI_{EVI}/dt$ also correlated significantly with precipitation only ($r^2 = 0.20$, $p < 0.005$, $n = 214$) and T_{air} only ($r^2 = 0.24$, $p < 0.005$, $n = 214$), as T_{air} and precipitation correlates ($r^2 = 0.16$, $p < 0.005$, $n = 214$) due to wet summers and dry winters at the site. Maximum $dLAI_{EVI}/dt$ occurred in hot and wet months, was always low in cold months, and was also low in extremely dry hot months.

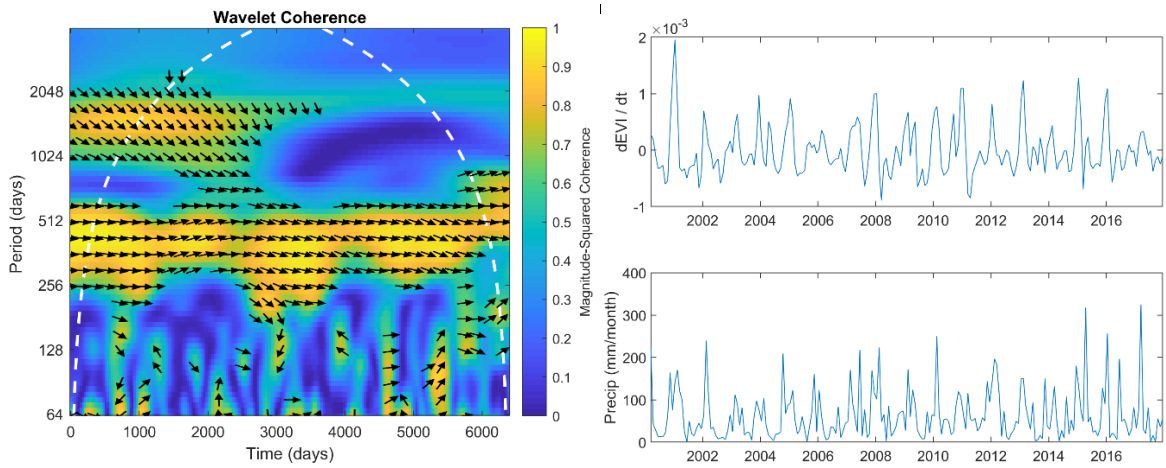

Figure S3. 3. Wavelet coherence between dEVI/dt and monthly precipitation (mm month^{-1}) , showing high coherence at annual time scale with no lag, as dEVI/dt and monthly precipitation peaked once a year, in summer. Some seasonal coherence appeared during summer months.

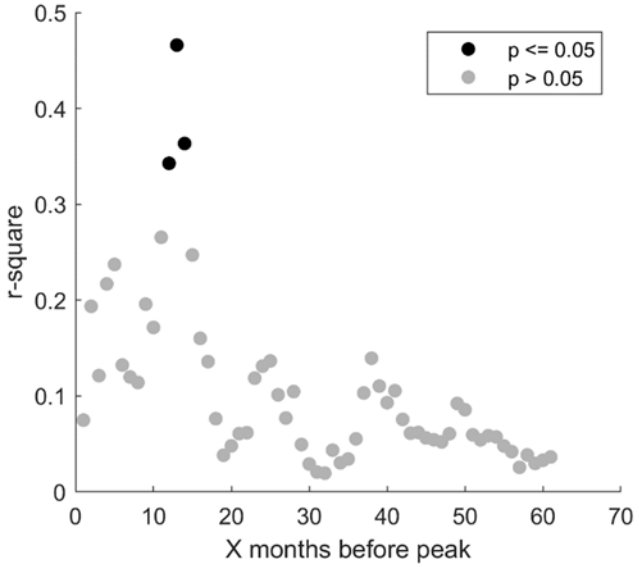

Figure S3. 4. r-square of linear regression of yearly peak of LAI_{EVI} vs. sum of precipitation X months before LAI_{EVI} max. The highest correlation appear when integrating precipitation in the past 13 months.

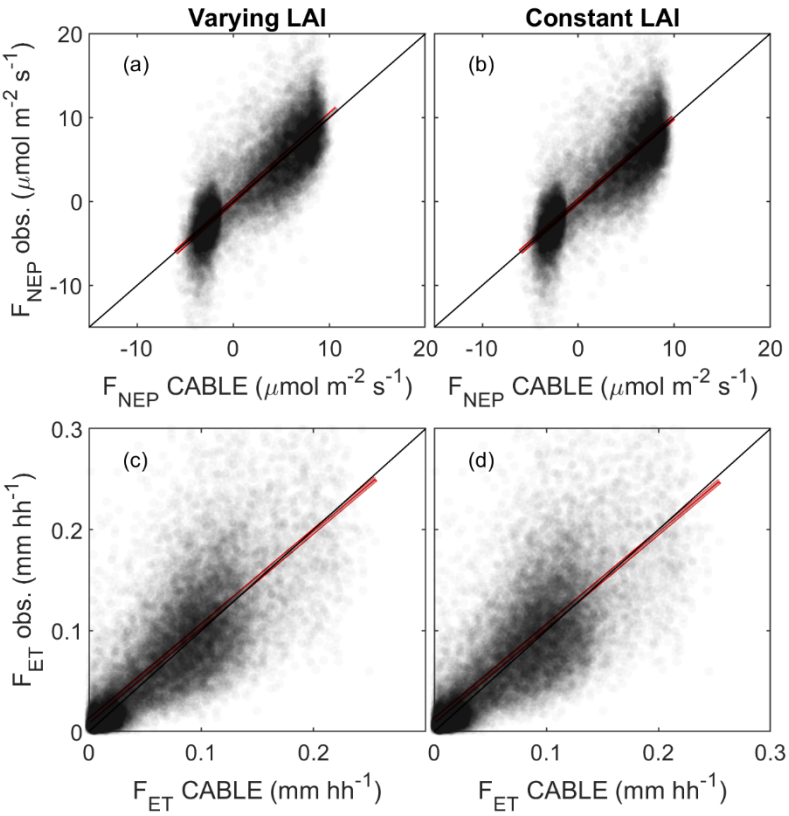

Figure S3. 5. Correlation between half-hourly eddy-covariance net ecosystem productivity observation (F_{NEP} obs., μmol m^{-2} s^{-1}) and evapotranspiration observation (F_{ET} obs., mm hh^{-1}) and CABLE half-hourly F_{NEP} and F_{ET} model. (a) F_{NEP} obs. vs. F_{NEP} CABLE varying LAI (LAI_{EVI}): r^2 = 0.595, n = 17005, (b) F_{NEP} obs. vs. F_{NEP} CABLE constant LAI (LAI = 1.5 m^2 m^{-2}): r^2 = 0.581, n = 17005, (c) F_{ET} obs. vs. F_{ET} CABLE varying LAI: r^2 = 0.62, n = 22081, (d) F_{ET} obs. vs. F_{ET} CABLE constant LAI: r^2 = 0.61, n = 22081.

Table S3. 1. Parameters of CABLE after PEST optimisation, refer to Table 3.2 for description and units

Parameter	Estimation and 95% CI
α	0.14 ± 0.002
k_n	0.61 ± 0.015
g1	5.36 ± 0.085
γ	2.80E-03 ± 0.600E-03
Vcmax_scalar	0.69 ± 0.010

Table S3. 2. Parameter correlation matrix (pearson's r), refer to Table 3.2 for description and units

	α	**k_n**	**g1**	**γ**	**Vcmax**
α	1	-0.12	-0.54	4.45E-03	0.29
k_n	-0.12	1	0.34	0.11	0.58
g1	-0.54	0.34	1	0.26	-0.32
γ	4.45E-03	0.11	0.26	1	0.12
Vcmax_scalar	0.29	0.58	-0.32	0.12	1

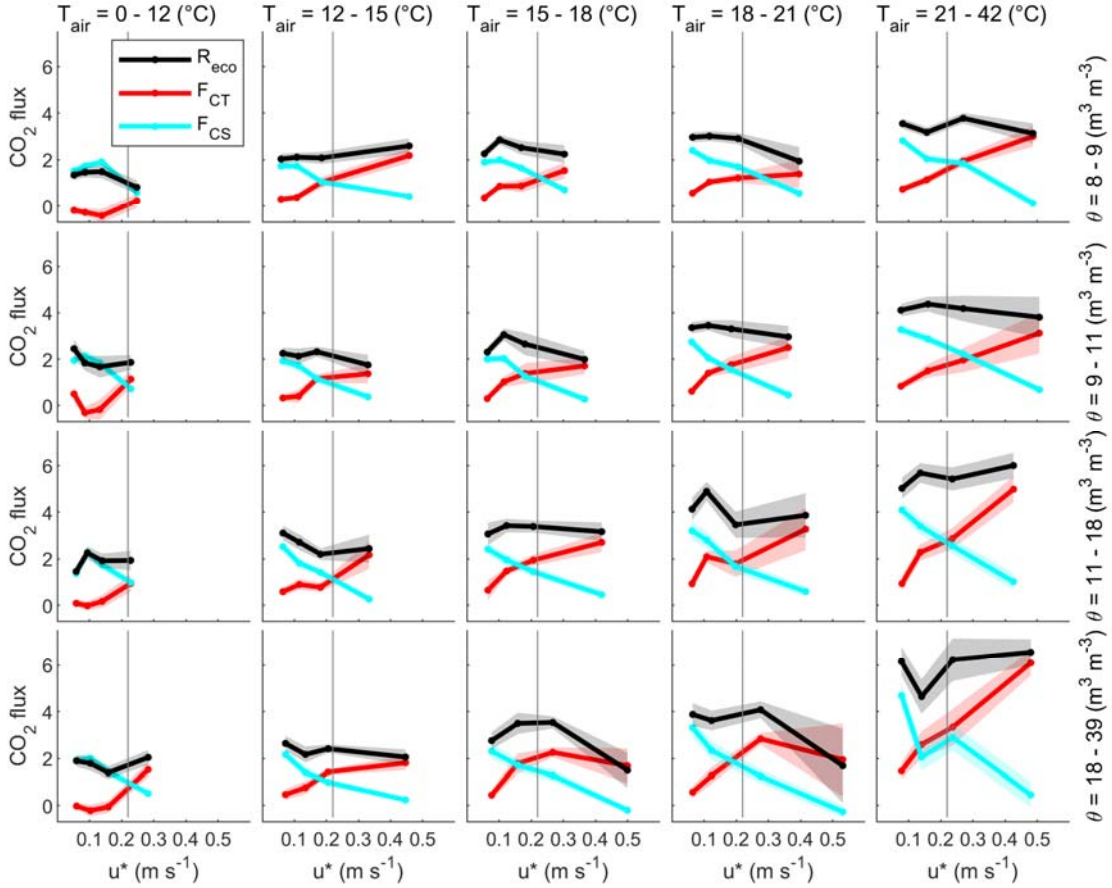

Figure S4. 1. Responses of nighttime CO_2 flux (vertical turbulent exchange F_{CT}, change in storage F_{CS} and ecosystem respitation $R_{eco} = F_{CT} + F_{CS}$) to friction velocity ($u_*$). 4 years (2014-2017) of data is divided into 20 quantiles, first into 5 air temperature (T_{air}) quantiles, then 4 soil moisture (θ) quantiles for each T_{air} quantile. Note that R_{eco} does vary with u_*, hence there was no clear change point threshold. Moreover, high u_* (> 0.2) occurred more often at high T_{air} and θ, leading to a sample bias when filtering data above $u_* = 0.2$.

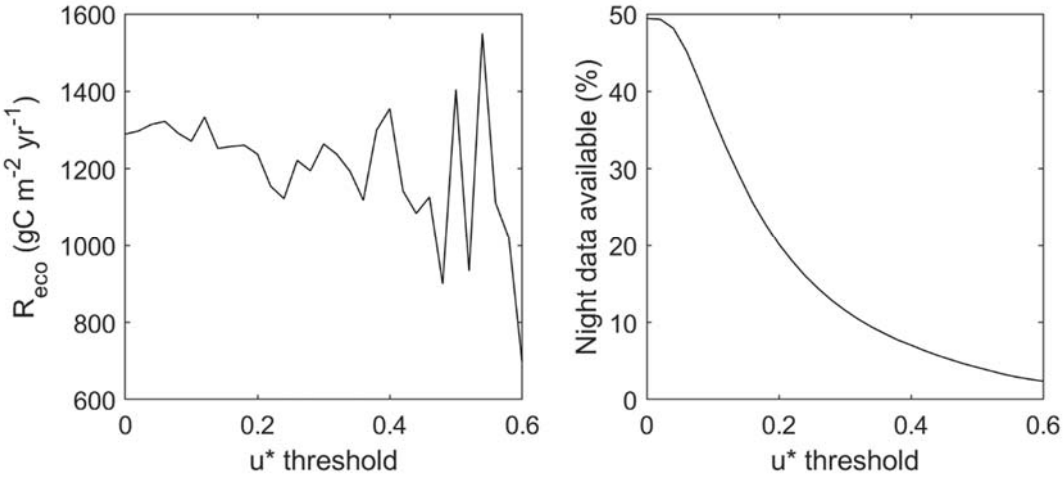

Figure S4. 2 Dependence of annual budget of R_{eco} as a function of u threshold.*

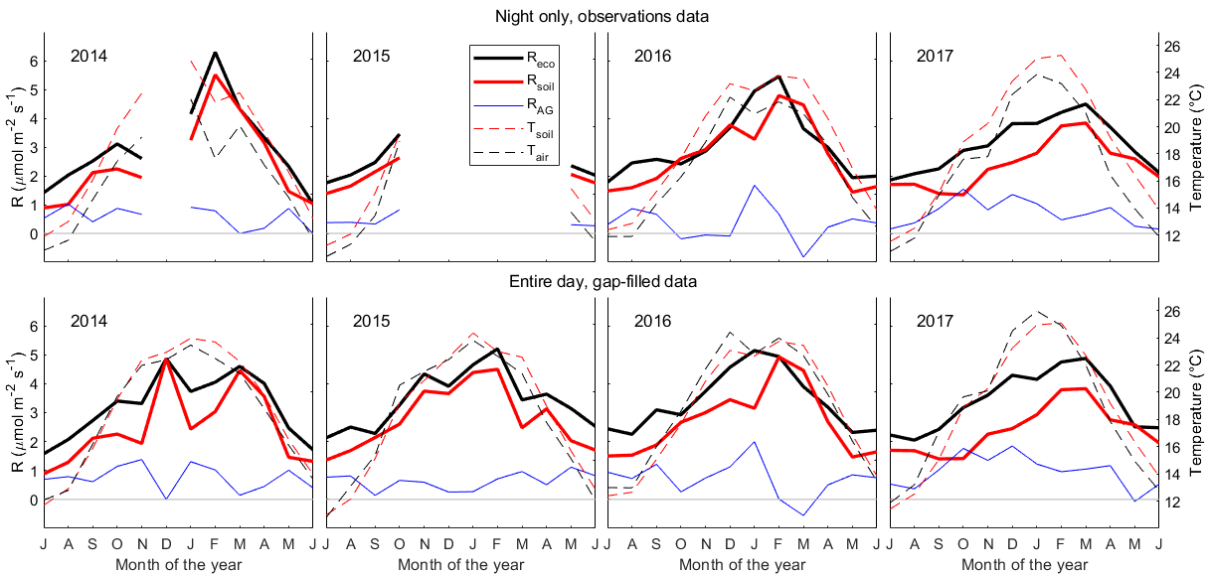

Figure S4. 3. Seasonal course (monthly median of half-hourly data) of ecosystem respiration (R_{eco}), soil respiration (R_{soil}), above-ground respiration (R_{AG}), soil temperature (T_{soil}) and air temperature (T_{air}). Top panel: night observations only. Bottom panel: gap-filled, day and night data. Note the seasonal course of R_{eco} is similar to the seasonal course of R_{soil}, but not of R_{AG}.

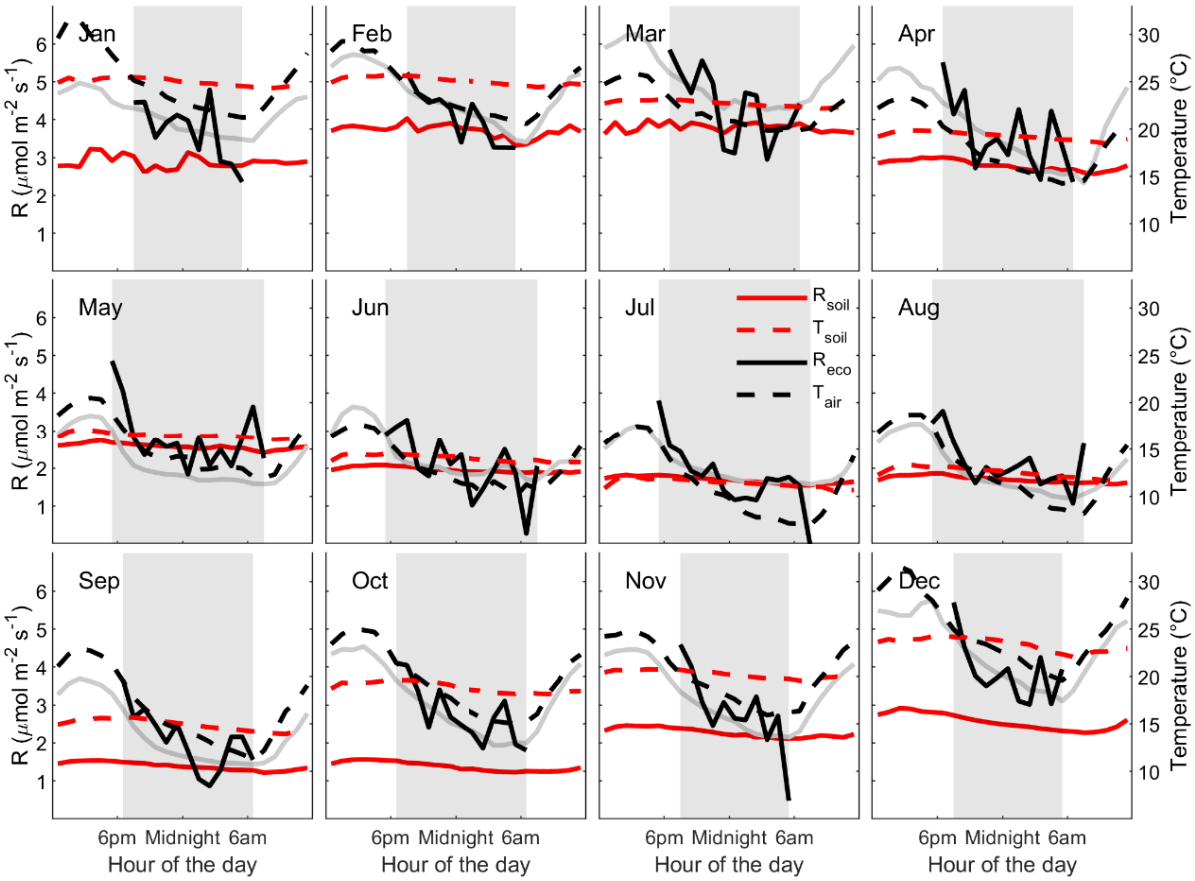

Figure S4. 4. Diurnal pattern of soil and ecosystem respiration, soil and air temperature, for each month of the year in 2017. Diurnals pattern (hourly medians), centred on midnight, for each month of the year 2017. Continuous black line is median of ecosystem respiration (R_{eco}) nighttime observations, continuous grey line is modelled R_{eco}. Dark red line is nighttime R_{soil}, light red line is daytime R_{soil}. Note how R_{soil} follows T_{soil}, and R_{eco} follows T_{air}, for each month of the year.

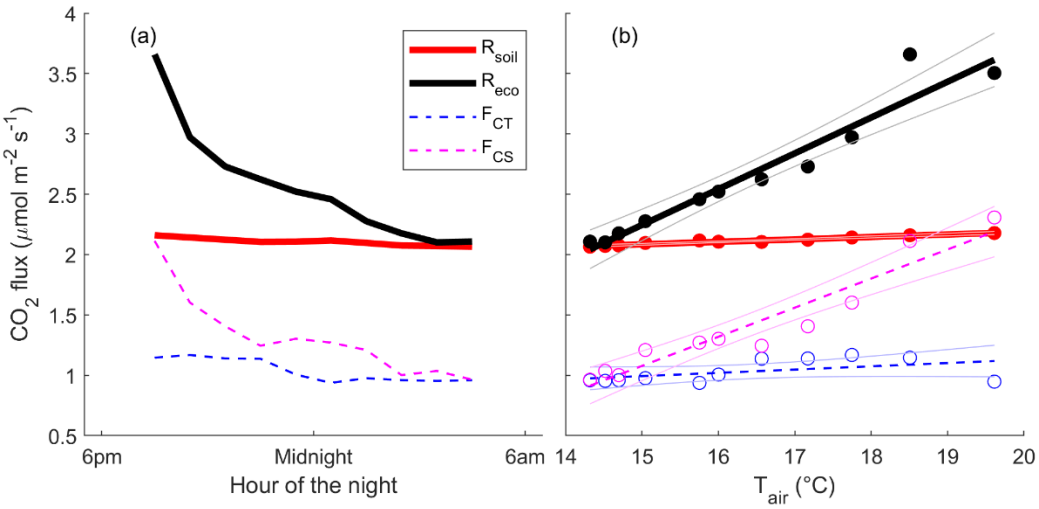

Figure S4. 5. Contribution of F_{CT} and F_{CS} to R_{eco} observation at night, (a) versus time and (b) versus air temperature. Note how $F_{CS} > F_{CT}$, indicating that at night, at AU-Cum, the change in storage component of the mass balance to determine R_{eco} is higher than the turbulent flux component on average, especially early in evening when air temperature is warm. The apparent response of R_{eco} to T_{air} was mainly accounted for by F_{CS}, as F_{CS} decreases overnight, but F_{CT} stays relatively constant.

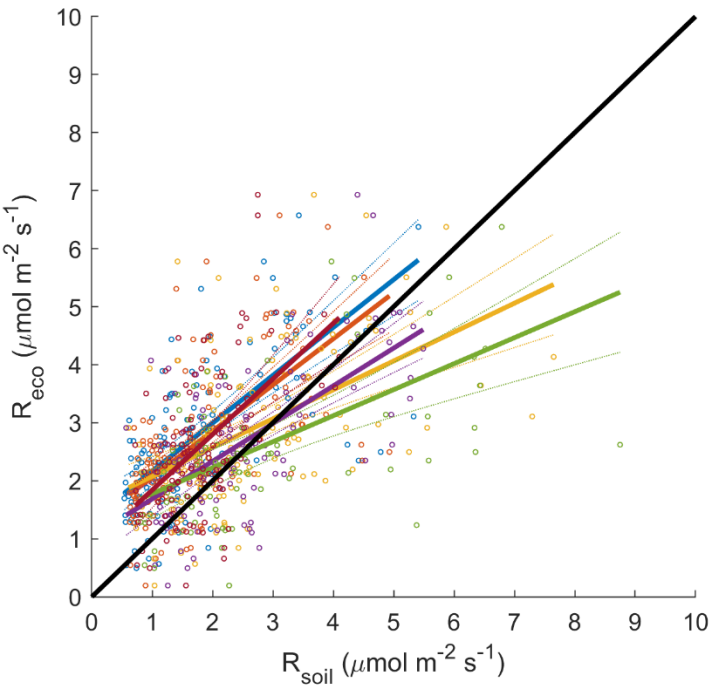

Figure S4. 6. Linear regression of nightly R_{soil} vs. R_{eco}, for 6 R_{soil} chambers. Note that in theory, $R_{eco} > R_{soil}$, as R_{soil} is a component of R_{eco}. Moreover, above-ground respiration ($R_{AG} = R_{eco} - R_{soil}$) is expected to increase with air temperature. Hence, I would expect the slopes of R_{eco} vs. R_{soil} to be higher than 1.

7 References

Anić, M., M. Ostrogović Sever, G. Alberti, I. Balenović, E. Paladinić, A. Peressotti, G. Tijan, Ž. Večenaj, D. Vuletić, and H. Marjanović. 2018. Eddy Covariance vs. Biometric Based Estimates of Net Primary Productivity of Pedunculate Oak (Quercus robur L.) Forest in Croatia during Ten Years. Forests **9**:764.

Asner, G. P., A. R. Townsend, and B. H. Braswell. 2000. Satellite observation of El Nino effects on Amazon forest phenology and productivity. Geophysical Research Letters **27**:981-984.

Atkin, O., C. Holly, and M. Ball. 2000. Acclimation of snow gum (Eucalyptus pauciflora) leaf respiration to seasonal and diurnal variations in temperature: the importance of changes in the capacity and temperature sensitivity of respiration. Plant, Cell & Environment **23**:15-26.

Aubinet, M., P. Berbigier, C. Bernhofer, A. Cescatti, C. Feigenwinter, A. Granier, T. Grünwald, K. Havrankova, B. Heinesch, and B. Longdoz. 2005. Comparing CO 2 storage and advection conditions at night at different carboeuroflux sites. Boundary-Layer Meteorology **116**:63-93.

Aubinet, M., B. Chermanne, M. Vandenhaute, B. Longdoz, M. Yernaux, and E. Laitat. 2001. Long term carbon dioxide exchange above a mixed forest in the Belgian Ardennes. Agricultural and Forest Meteorology **108**:293-315.

Aubinet, M., A. Grelle, A. Ibrom, U. Rannik, J. Moncrieff, T. Foken, A. S. Kowalski, P. H. Martin, P. Berbigier, C. Bernhofer, R. Clement, J. Elbers, A. Granier, T. Grunwald, K. Morgenstern, K. Pilegaard, C. Rebmann, W. Snijders, R. Valentini, and T. Vesala. 2000. Estimates of the annual net carbon and water exchange of forests: The EUROFLUX methodology. Advances in Ecological Research, Vol 30 **30**:113-175.

Aubinet, M., Q. Hurdebise, H. Chopin, A. Debacq, A. De Ligne, B. Heinesch, T. Manise, and C. Vincke. 2018. Inter-annual variability of Net Ecosystem Productivity for a temperate mixed forest: A predominance of carry-over effects? Agricultural and Forest Meteorology **262**:340-353.

Aubinet, M., T. Vesala, and D. Papale. 2012. Eddy Covariance A Practical Guide to Measurement and Data Analysis. Springer.

Bach, C. S. 2002. Phenological patterns in monsoon rainforests in the Northern Territory, Australia. Austral Ecology **27**:477-489.

Bain, W. G., L. Hutyra, D. C. Patterson, A. V. Bright, B. C. Daube, J. W. Munger, and S. C. Wofsy. 2005. Wind-induced error in the measurement of soil respiration using closed dynamic chambers. Agricultural and Forest Meteorology **131**:225-232.

Baldocchi, D. 2008. 'Breathing'of the terrestrial biosphere: lessons learned from a global network of carbon dioxide flux measurement systems. Australian journal of botany **56**:1-26.

Baldocchi, D., H. Chu, and M. Reichstein. 2018. Inter-annual variability of net and gross ecosystem carbon fluxes: A review. Agricultural and Forest Meteorology **249**:520-533.

Baldocchi, D., E. Falge, L. Gu, R. Olson, D. Hollinger, S. Running, P. Anthoni, C. Bernhofer, K. Davis, and R. Evans. 2001a. FLUXNET: A new tool to study the temporal and spatial variability of ecosystem-scale carbon dioxide, water vapor, and energy flux densities. Bulletin of the American Meteorological Society **82**:2415-2434.

Baldocchi, D., E. Falge, L. Gu, R. Olson, D. Hollinger, S. Running, P. Anthoni, C. Bernhofer, K. Davis, and R. Evans. 2001b. FLUXNET: A new tool to study the temporal and spatial variability of ecosystem–scale carbon dioxide, water vapor, and energy flux densities. Bulletin of the American Meteorological Society **82**:2415-2434.

Baldocchi, D., Y. Ryu, and T. Keenan. 2016. Terrestrial Carbon Cycle Variability. F1000Research **5**.

Baldocchi, D., R. Valentini, S. Running, W. Oechel, and R. Dahlman. 1996. Strategies for measuring and modelling carbon dioxide and water vapour fluxes over terrestrial ecosystems. Global Change Biology **2**:159-168.

Baldocchi, D. D., B. B. Hicks, and T. P. Meyers. 1988. MEASURING BIOSPHERE-ATMOSPHERE EXCHANGES OF BIOLOGICALLY RELATED GASES WITH MICROMETEOROLOGICAL METHODS. Ecology **69**:1331-1340.

Barba, J., A. Cueva, M. Bahn, G. A. Barron-Gafford, B. Bond-Lamberty, P. J. Hanson, A. Jaimes, L. Kulmala, J. Pumpanen, and R. L. Scott. 2018. Comparing ecosystem and soil respiration: Review and key challenges of tower-based and soil measurements. Agricultural and Forest Meteorology **249**:434-443.

Barr, A., A. Richardson, D. Hollinger, D. Papale, M. Arain, T. Black, G. Bohrer, D. Dragoni, M. Fischer, and L. Gu. 2013. Use of change-point detection for friction–velocity threshold evaluation in eddy-covariance studies. Agricultural and Forest Meteorology **171**:31-45.

Barr, A. G., T. Black, E. Hogg, N. Kljun, K. Morgenstern, and Z. Nesic. 2004. Inter-annual variability in the leaf area index of a boreal aspen-hazelnut forest in relation to net ecosystem production. Agricultural and Forest Meteorology **126**:237-255.

Bastos, A., S. W. Running, C. Gouveia, and R. M. Trigo. 2013. The global NPP dependence on ENSO: La Niña and the extraordinary year of 2011. Journal of Geophysical Research: Biogeosciences **118**:1247-1255.

Battaglia, M., and P. Sands. 1997. Modelling site productivity of Eucalyptus globulus in response to climatic and site factors. Functional Plant Biology **24**:831-850.

Bauerle, W. L., R. Oren, D. A. Way, S. S. Qian, P. C. Stoy, P. E. Thornton, J. D. Bowden, F. M. Hoffman, and R. F. Reynolds. 2012. Photoperiodic regulation of the seasonal pattern of photosynthetic capacity and the implications for carbon cycling. Proceedings of the National Academy of Sciences **109**:8612-8617.

Beringer, J., L. B. Hutley, I. McHugh, S. K. Arndt, D. Campbell, H. A. Cleugh, J. Cleverly, V. R. de Dios, D. Eamus, B. Evans, C. Ewenz, P. Grace, A. Griebel, V. Haverd, N. Hinko-Najera, A. Huete, P. Isaac, K. Kanniah, R. Leuning, M. J. Liddell, C. Macfarlane, W. Meyer, C. Moore, E. Pendall, A. Phillips, R. L. Phillips, S. M. Prober, N. Restrepo-Coupe, S. Rutledge, I. Schroder, R. Silberstein, P. Southall, M. S. Yee, N. J. Tapper, E. van Gorsel, C. Vote, J. Walker, and T. Wardlaw. 2016. An introduction to the Australian and New Zealand flux tower network - OzFlux. Biogeosciences **13**:5895-5916.

Betts, R., P. Cox, M. Collins, P. Harris, C. Huntingford, and C. Jones. 2004. The role of ecosystem-atmosphere interactions in simulated Amazonian precipitation decrease and forest dieback under global climate warming. Theoretical and applied climatology **78**:157-175.

Brændholt, A., A. Ibrom, K. S. Larsen, and K. Pilegaard. 2018. Partitioning of ecosystem respiration in a beech forest. Agricultural and Forest Meteorology **252**:88-98.

Breiman, L. 2001. Random forests. Machine learning **45**:5-32.

Burba, G. 2013. Eddy covariance method for scientific, industrial, agricultural and regulatory applications: A field book on measuring ecosystem gas exchange and areal emission rates. LI-Cor Biosciences.

Campbell, G. S., and J. M. Norman. 2012. An introduction to environmental biophysics. Springer Science & Business Media.

Crous, K. Y., J. ZARAGOZA-CASTELLS, D. S. Ellsworth, R. A. Duursma, M. Loew, D. T. Tissue, and O. K. Atkin. 2012. Light inhibition of leaf respiration in field-grown

Eucalyptus saligna in whole-tree chambers under elevated atmospheric CO2 and summer drought. Plant, Cell & Environment **35**:966-981.

Crous, K. Y., J. ZARAGOZA-CASTELLS, M. Loew, D. S. Ellsworth, D. T. Tissue, M. G. Tjoelker, C. V. Barton, T. E. Gimeno, and O. K. Atkin. 2011. Seasonal acclimation of leaf respiration in Eucalyptus saligna trees: impacts of elevated atmospheric CO2 and summer drought. Global Change Biology **17**:1560-1576.

Cueva, A., M. Bahn, M. Litvak, J. Pumpanen, and R. Vargas. 2015. A multisite analysis of temporal random errors in soil CO2 efflux. Journal of Geophysical Research: Biogeosciences **120**:737-751.

Davidson, E. A., S. Samanta, S. S. Caramori, and K. Savage. 2012. The D ual A rrhenius and M ichaelis–M enten kinetics model for decomposition of soil organic matter at hourly to seasonal time scales. Global Change Biology **18**:371-384.

De Kauwe, M. G., J. Kala, Y. S. Lin, A. J. Pitman, B. E. Medlyn, R. A. Duursma, G. Abramowitz, Y. P. Wang, and D. G. Miralles. 2015. A test of an optimal stomatal conductance scheme within the CABLE land surface model. Geoscientific Model Development **8**:431-452.

De Kauwe, M. G., B. E. Medlyn, S. Zaehle, A. P. Walker, M. C. Dietze, Y. P. Wang, Y. Luo, A. K. Jain, B. El-Masri, and T. Hickler. 2014. Where does the carbon go? A model–data intercomparison of vegetation carbon allocation and turnover processes at two temperate forest free-air CO2 enrichment sites. New Phytologist **203**:883-899.

Desai, A. R., A. D. Richardson, A. M. Moffat, J. Kattge, D. Y. Hollinger, A. Barr, E. Falge, A. Noormets, D. Papale, M. Reichstein, and V. J. Stauch. 2008. Cross-site evaluation of eddy covariance GPP and RE decomposition techniques. Agricultural and Forest Meteorology **148**:821-838.

Didan, K. 2015a. MOD13Q1 MODIS/Terra Vegetation Indices 16-Day L3 Global 250 m SIN Grid V006. NASA EOSDIS Land Processes DAAC.

Didan, K. 2015b. MOD13Q1 MODIS/Terra vegetation indices 16-day L3 global 250m SIN grid V006. NASA EOSDIS Land Processes DAAC.

Dixon, R. K., S. Brown, R. e. a. Houghton, A. Solomon, M. Trexler, and J. Wisniewski. 1994. Carbon pools and flux of global forest ecosystems. Science(Washington) **263**:185-189.

Dou, X., and Y. Yang. 2018. Estimating forest carbon fluxes using four different data-driven techniques based on long-term eddy covariance measurements: Model comparison and evaluation. Science of the Total Environment **627**:78-94.

Drake, J. E., C. A. Macdonald, M. G. Tjoelker, P. B. Reich, B. K. Singh, I. C. Anderson, and D. S. Ellsworth. 2018. Three years of soil respiration in a mature eucalypt woodland exposed to atmospheric CO 2 enrichment. Biogeochemistry **139**:85-101.

Duursma, R. A., C. V. Barton, Y.-S. Lin, B. E. Medlyn, D. Eamus, D. T. Tissue, D. S. Ellsworth, and R. E. McMurtrie. 2014. The peaked response of transpiration rate to vapour pressure deficit in field conditions can be explained by the temperature optimum of photosynthesis. Agricultural and Forest Meteorology **189**:2-10.

Duursma, R. A., T. E. Gimeno, M. M. Boer, K. Y. Crous, M. G. Tjoelker, and D. S. Ellsworth. 2016. Canopy leaf area of a mature evergreen Eucalyptus woodland does not respond to elevated atmospheric CO2 but tracks water availability. Global Change Biology **22**:1666-1676.

Ellsworth, D. S., I. C. Anderson, K. Y. Crous, J. Cooke, J. E. Drake, A. N. Gherlenda, T. E. Gimeno, C. A. Macdonald, B. E. Medlyn, and J. R. Powell. 2017. Elevated CO 2 does not increase eucalypt forest productivity on a low-phosphorus soil. Nature Climate Change **7**:279.

England, J. R., and P. M. Attiwill. 2008. Patterns of growth and nutrient accumulation in expanding leaves of Eucalyptus regnans (Myrtaceae). Australian journal of botany **56**:44-50.

Fan, S.-M., S. C. Wofsy, P. S. Bakwin, D. J. Jacob, and D. R. Fitzjarrald. 1990. Atmosphere-biosphere exchange of CO 2 and O 3 in the central Amazon forest.

Farquhar, G., and S. Wong. 1984. An Empirical Model of Stomatal Conductance. Functional Plant Biology **11**:191-210.

Farquhar, G. D., S. V. Caemmerer, and J. A. Berry. 1980. A BIOCHEMICAL-MODEL OF PHOTOSYNTHETIC CO2 ASSIMILATION IN LEAVES OF C-3 SPECIES. Planta **149**:78-90.

Foken, T. 2008. The energy balance closure problem: an overview. Ecological Applications **18**:1351-1367.

Foken, T., M. Gockede, M. Mauder, L. Mahrt, B. Amiro, and W. Munger. 2004. Post-field data quality control. Handbook of Micrometeorology: A Guide for Surface Flux Measurement and Analysis **29**:181-208.

Foken, T., F. Wimmer, M. Mauder, C. Thomas, and C. Liebethal. 2006. Some aspects of the energy balance closure problem. Atmospheric Chemistry and Physics **6**:4395-4402.

Forkel, M., N. Carvalhais, C. Rödenbeck, R. Keeling, M. Heimann, K. Thonicke, S. Zaehle, and M. Reichstein. 2016. Enhanced seasonal CO2 exchange caused by amplified plant productivity in northern ecosystems. Science **351**:696-699.

Franklin, O., J. Johansson, R. C. Dewar, U. Dieckmann, R. E. McMurtrie, Å. Brännström, and R. Dybzinski. 2012. Modeling carbon allocation in trees: a search for principles. Tree Physiology **32**:648-666.

Friedlingstein, P., I. Fung, E. Holland, J. John, G. Brasseur, D. Erickson, and D. Schimel. 1995. On the contribution of CO2 fertilization to the missing biospheric sink. Global Biogeochemical Cycles **9**:541-556.

Furze, M. E., B. A. Huggett, D. M. Aubrecht, C. D. Stolz, M. S. Carbone, and A. D. Richardson. 2019. Whole-tree nonstructural carbohydrate storage and seasonal dynamics in five temperate species. New Phytologist **221**:1466-1477.

Garonna, I., R. De Jong, A. J. De Wit, C. A. Mücher, B. Schmid, and M. E. Schaepman. 2014. Strong contribution of autumn phenology to changes in satellite-derived growing season length estimates across Europe (1982–2011). Global Change Biology **20**:3457-3470.

Gash, J., and A. Culf. 1996. Applying a linear detrend to eddy correlation data in realtime. Boundary-Layer Meteorology **79**:301-306.

Giasson, M.-A., A. M. Ellison, R. D. Bowden, P. M. Crill, E. A. Davidson, J. E. Drake, S. D. Frey, J. L. Hadley, M. Lavine, and J. M. Melillo. 2013. Soil respiration in a northeastern US temperate forest: a 22-year synthesis. Ecosphere **4**:1-28.

Gimeno, T. E., K. Y. Crous, J. Cooke, A. P. O'Grady, A. Ósvaldsson, B. E. Medlyn, and D. S. Ellsworth. 2016. Conserved stomatal behaviour under elevated CO2 and varying water availability in a mature woodland. Functional Ecology **30**:700-709.

Graham, E. A., S. S. Mulkey, K. Kitajima, N. G. Phillips, and S. J. Wright. 2003. Cloud cover limits net CO2 uptake and growth of a rainforest tree during tropical rainy seasons. Proceedings of the National Academy of Sciences **100**:572-576.

Grant, I., D. Jones, W. Wang, R. Fawcett, and D. Barratt. 2008. Meteorological and remotely sensed datasets for hydrological modelling: a contribution to the Australian Water Availability Project. Australian Bureau of Meteorology: Canberra.

Griebel, A., L. T. Bennett, D. S. Culvenor, G. J. Newnham, and S. K. Arndt. 2015. Reliability and limitations of a novel terrestrial laser scanner for daily monitoring of forest canopy dynamics. Remote Sensing of Environment **166**:205-213.

Griebel, A., D. M. Watson, and E. Pendall. 2017. Mistletoe, friend and foe: synthesizing ecosystem implications of mistletoe infection. Environmental Research Letters.

Haverd, V., M. R. Raupach, P. R. Briggs, J. G. Canadell, P. Isaac, C. Pickett-Heaps, S. H. Roxburgh, E. van Gorsel, R. A. Viscarra Rossel, and Z. Wang. 2013. Multiple observation types reduce uncertainty in Australia's terrestrial carbon and water cycles. Biogeosciences **10**:2011-2040.

Haverd, V., B. Smith, L. Nieradzik, P. R. Briggs, W. Woodgate, C. M. Trudinger, and J. G. Canadell. 2017. A new version of the CABLE land surface model, incorporating land-use change, woody vegetation demography and a novel optimisation-based approach to plant coordination of photosynthesis. arXiv preprint arXiv:1711.05351.

Haverd, V., B. Smith, L. Nieradzik, P. R. Briggs, W. Woodgate, C. M. Trudinger, J. G. Canadell, and M. Cuntz. 2018. A new version of the CABLE land surface model (Subversion revision r4601) incorporating land use and land cover change, woody vegetation demography, and a novel optimisation-based approach to plant coordination of photosynthesis. Geoscientific Model Development **11**.

Hayek, M. N., R. Wehr, M. Longo, L. R. Hutyra, K. Wiedemann, J. W. Munger, D. Bonal, S. R. Saleska, D. R. Fitzjarrald, and S. C. Wofsy. 2018. A novel correction for biases in forest eddy covariance carbon balance. Agricultural and Forest Meteorology **250**:90-101.

Heinemeyer, A., I. P. Hartley, S. P. Evans, J. A. Carreira de La Fuente, and P. Ineson. 2007. Forest soil CO2 flux: uncovering the contribution and environmental responses of ectomycorrhizas. Global Change Biology **13**:1786-1797.

Heskel, M. A., O. K. Atkin, M. H. Turnbull, and K. L. Griffin. 2013. Bringing the Kok effect to light: a review on the integration of daytime respiration and net ecosystem exchange. Ecosphere **4**:1-14.

Hill, M. J., U. Senarath, A. Lee, M. Zeppel, J. M. Nightingale, R. D. J. Williams, and T. R. McVicar. 2006. Assessment of the MODIS LAI product for Australian ecosystems. Remote Sensing of Environment **101**:495-518.

Hinko-Najera, N., P. Isaac, J. Beringer, E. van Gorsel, C. Ewenz, I. McHugh, J. F. Exbrayat, S. J. Livesley, and S. K. Arndt. 2017a. Net ecosystem carbon exchange of a dry temperate eucalypt forest. Biogeosciences **14**:3781-3800.

Hinko-Najera, N., P. Isaac, J. Beringer, E. van Gorsel, C. M. Ewenz, I. McHugh, J.-F. Exbrayat, S. J. Livesley, and S. K. Arndt. 2017b. Net ecosystem carbon exchange of a dry temperate eucalypt forest.

Huete, A., N. Restrepo-Coupe, P. Ratana, K. Didan, S. Saleska, K. Ichii, S. Panuthai, and M. Gamo. 2008. Multiple site tower flux and remote sensing comparisons of tropical forest dynamics in Monsoon Asia. Agricultural and Forest Meteorology **148**:748-760.

Hutyra, L. R., J. W. Munger, S. R. Saleska, E. Gottlieb, B. C. Daube, A. L. Dunn, D. F. Amaral, P. B. De Camargo, and S. C. Wofsy. 2007. Seasonal controls on the exchange of carbon and water in an Amazonian rain forest. Journal of Geophysical Research: Biogeosciences **112**.

Isaac, P., J. Cleverly, I. McHugh, E. van Gorsel, C. Ewenz, and J. Beringer. 2017. OzFlux Data: Network integration from collection to curation. Biogeosciences **14**:2903.

Jian, J., M. K. Steele, S. D. Day, R. Q. Thomas, and S. C. Hodges. 2018. Measurement strategies to account for soil respiration temporal heterogeneity across diverse regions. Soil Biology and Biochemistry **125**:167-177.

Jones, D. A., W. Wang, and R. Fawcett. 2009. High-quality spatial climate data-sets for Australia. Australian Meteorological and Oceanographic Journal **58**:233.

Jones, T. L., D. E. Tucker, and D. R. Ort. 1998. Chilling delays circadian pattern of sucrose phosphate synthase and nitrate reductase activity in tomato. Plant Physiology **118**:149-158.

Kaimal, J. C., J. Wyngaard, Y. Izumi, and O. Coté. 1972. Spectral characteristics of surface-layer turbulence. Quarterly Journal of the Royal Meteorological Society **98**:563-589.

Karan, M., M. Liddell, S. M. Prober, S. Arndt, J. Beringer, M. Boer, J. Cleverly, D. Eamus, P. Grace, and E. Van Gorsel. 2016. The Australian SuperSite Network: A continental, long-term terrestrial ecosystem observatory. Science of the Total Environment **568**:1263-1274.

Keeling, C. D., S. C. Piper, R. B. Bacastow, M. Wahlen, T. P. Whorf, M. Heimann, and H. A. Meijer. 2001. Exchanges of atmospheric CO2 and 13CO2 with the terrestrial biosphere and oceans from 1978 to 2000. I. Global aspects. Scripps Institution of Oceanography.

Keenan, T., M. Migliavacca, D. Papale, D. Baldocchi, M. Reichstein, M. Torn, and T. Wutzler. 2018. Inhibition of leaf respiration by light: implications for eddy-covariance partitioning. Page 18603 *in* EGU General Assembly Conference Abstracts.

Keenan, T. F., J. Gray, M. A. Friedl, M. Toomey, G. Bohrer, D. Y. Hollinger, J. W. Munger, J. O'Keefe, H. P. Schmid, and I. S. Wing. 2014. Net carbon uptake has increased through warming-induced changes in temperate forest phenology. Nature Climate Change **4**:598.

Keenan, T. F., M. Migliavacca, D. Papale, D. Baldocchi, M. Reichstein, M. Torn, and T. Wutzler. 2019. Widespread inhibition of daytime ecosystem respiration. Nature Ecology & Evolution:1.

Keenan, T. F., I. C. Prentice, J. G. Canadell, C. A. Williams, H. Wang, M. Raupach, and G. J. Collatz. 2016. Recent pause in the growth rate of atmospheric CO 2 due to enhanced terrestrial carbon uptake. Nature communications **7**:13428.

Keith, H., E. van Gorsel, K. L. Jacobsen, and H. A. Cleugh. 2012. Dynamics of carbon exchange in a Eucalyptus forest in response to interacting disturbance factors. Agricultural and Forest Meteorology **153**:67-81.

Kicklighter, D. W., M. Bruno, S. DZönges, G. Esser, M. Heimann, J. Helfrich, F. Ift, F. Joos, J. Kaduk, and G. H. Kohlmaier. 1999. A first-order analysis of the potential role of CO2 fertilization to affect the global carbon budget: a comparison of four terrestrial biosphere models. Tellus B: Chemical and Physical Meteorology **51**:343-366.

King, A. W., C. A. Gunderson, W. M. Post, D. J. Weston, and S. D. Wullschleger. 2006. Plant respiration in a warmer world. Science **312**:536-537.

Knauer, J., C. Werner, and S. Zaehle. 2015. Evaluating stomatal models and their atmospheric drought response in a land surface scheme: A multibiome analysis. Journal of Geophysical Research: Biogeosciences **120**:1894-1911.

Knauer, J., S. Zaehle, B. E. Medlyn, M. Reichstein, C. A. Williams, M. Migliavacca, M. G. De Kauwe, C. Werner, C. Keitel, and P. Kolari. 2017. Towards physiologically meaningful water-use efficiency estimates from eddy covariance data. Global Change Biology.

Kok, B. 1949. On the interrelation of respiration and photosynthesis in green plants. Biochimica et biophysica acta **3**:625-631.

Kolari, P., H. K. Lappalainen, H. Hänninen, and P. Hari. 2007. Relationship between temperature and the seasonal course of photosynthesis in Scots pine at northern timberline and in southern boreal zone. Tellus B **59**:542-552.

Kormann, R., and F. X. Meixner. 2001. An analytical footprint model for non-neutral stratification. Boundary-Layer Meteorology **99**:207-224.

Kowalczyk, E. A., Y. P. Wang, R. M. Law, H. L. Davies, J. L. McGregor, and G. Abramowitz. 2006. The CSIRO Atmosphere Biosphere Land Exchange (CABLE) model for use in climate models and as an offline model. CSIRO Marine and Atmospheric Research.

Lasslop, G., M. Reichstein, D. Papale, A. D. Richardson, A. Arneth, A. Barr, P. Stoy, and G. Wohlfahrt. 2010. Separation of net ecosystem exchange into assimilation and respiration using a light response curve approach: critical issues and global evaluation. Global Change Biology **16**:187-208.

Law, B. E., M. G. Ryan, and P. M. Anthoni. 1999. Seasonal and annual respiration of a ponderosa pine ecosystem. Global Change Biology **5**:169-182.

Le Quéré, C., R. M. Andrew, P. Friedlingstein, S. Sitch, J. Hauck, J. Pongratz, P. Pickers, J. I. Korsbakken, G. P. Peters, and J. G. Canadell. 2018. Global Carbon Budget 2018. Earth System Science Data **10**:2141-2194.

Lim, P. O., H. J. Kim, and H. Gil Nam. 2007. Leaf senescence. Annu. Rev. Plant Biol. **58**:115-136.

Lindroth, A., A. Grelle, and A. S. Morén. 1998. Long-term measurements of boreal forest carbon balance reveal large temperature sensitivity. Global Change Biology **4**:443-450.

Lindroth, A., L. Klemedtsson, A. Grelle, P. Weslien, and O. Langvall. 2008. Measurement of net ecosystem exchange, productivity and respiration in three spruce forests in Sweden shows unexpectedly large soil carbon losses. Biogeochemistry **89**:43-60.

Lloyd, J., and J. A. Taylor. 1994. ON THE TEMPERATURE-DEPENDENCE OF SOIL RESPIRATION. Functional Ecology **8**:315-323.

Macfarlane, C., A. Grigg, and C. Evangelista. 2007. Estimating forest leaf area using cover and fullframe fisheye photography: Thinking inside the circle. Agricultural and Forest Meteorology **146**:1-12.

Macfarlane, C., Y. Ryu, G. N. Ogden, and O. Sonnentag. 2014. Digital canopy photography: Exposed and in the raw. Agricultural and Forest Meteorology **197**:244-253.

Maeda, E. E., J. Heiskanen, L. E. Aragão, and J. Rinne. 2014. Can MODIS EVI monitor ecosystem productivity in the Amazon rainforest? Geophysical Research Letters **41**:7176-7183.

McHugh, I. D., J. Beringer, S. C. Cunningham, P. J. Baker, T. R. Cavagnaro, R. Mac Nally, and R. M. Thompson. 2017. Interactions between nocturnal turbulent flux, storage and advection at an “ideal” eucalypt woodland site. Biogeosciences **14**:3027-3050.

Medlyn, B. E., M. G. De Kauwe, Y. S. Lin, J. Knauer, R. A. Duursma, C. A. Williams, A. Arneth, R. Clement, P. Isaac, and J. M. Limousin. 2017. How do leaf and ecosystem measures of water-use efficiency compare? New Phytologist.

Medlyn, B. E., M. G. De Kauwe, S. Zaehle, A. P. Walker, R. A. Duursma, K. Luus, M. Mishurov, B. Pak, B. Smith, and Y. P. Wang. 2016. Using models to guide field experiments: a priori predictions for the CO 2 response of a nutrient-and water-limited native Eucalypt woodland. Global Change Biology **22**:2834-2851.

Medlyn, B. E., R. A. Duursma, D. Eamus, D. S. Ellsworth, I. C. Prentice, C. V. M. Barton, K. Y. Crous, P. De Angelis, M. Freeman, and L. Wingate. 2011. Reconciling the optimal and empirical approaches to modelling stomatal conductance. Global Change Biology **17**:2134-2144.

Medlyn, B. E., S. Zaehle, M. G. De Kauwe, A. P. Walker, M. C. Dietze, P. J. Hanson, T. Hickler, A. K. Jain, Y. Luo, and W. Parton. 2015. Using ecosystem experiments to improve vegetation models. Nature Climate Change **5**:528.

Mitscherlich, E. A. 1909. Das Gesetz des Minimums und das Gesetz des abnehmenden Bodenertrages. Landw. Jahrb **38**:537-552.

Moffat, A. M., D. Papale, M. Reichstein, D. Y. Hollinger, A. D. Richardson, A. G. Barr, C. Beckstein, B. H. Braswell, G. Churkina, and A. R. Desai. 2007. Comprehensive comparison of gap-filling techniques for eddy covariance net carbon fluxes. Agricultural and Forest Meteorology **147**:209-232.

Moncrieff, J., R. Clement, J. Finnigan, and T. Meyers. 2004. Averaging, detrending, and filtering of eddy covariance time series. Pages 7-31 Handbook of micrometeorology. Springer.

Moncrieff, J. B., J. M. Massheder, H. deBruin, J. Elbers, T. Friborg, B. Heusinkveld, P. Kabat, S. Scott, H. Soegaard, and A. Verhoef. 1997. A system to measure surface fluxes of momentum, sensible heat, water vapour and carbon dioxide. Journal of Hydrology **189**:589-611.

Monteith, J. L. 1965. Evaporation and environment. Page 4 *in* Symp. Soc. Exp. Biol.

Moore, C. E., T. F. Keenan, R. A. Duursma, A. I. van Dijk, L. B. Hutley, J. R. Taylor, and M. J. Liddell. 2016. Reviews and syntheses: Australian vegetation phenology: new insights from satellite remote sensing and digital repeat photography. Biogeosciences **13**:5085.

Munné-Bosch, S., and L. Alegre. 2004. Die and let live: leaf senescence contributes to plant survival under drought stress. Functional Plant Biology **31**:203-216.

Noormets, A. 2009. Phenology of ecosystem processes: applications in global change research. Springer.

Novick, K. A., D. L. Ficklin, P. C. Stoy, C. A. Williams, G. Bohrer, A. C. Oishi, S. A. Papuga, P. D. Blanken, A. Noormets, B. N. Sulman, R. L. Scott, L. X. Wang, and R. P. Phillips. 2016. The increasing importance of atmospheric demand for ecosystem water and carbon fluxes. Nature Climate Change **6**:1023-1027.

Novick, K. A., A. C. Oishi, E. J. Ward, M. B. S. Siqueira, J. Y. Juang, and P. C. Stoy. 2015. On the difference in the net ecosystem exchange of CO2 between deciduous and evergreen forests in the southeastern United States. Global Change Biology **21**:827-842.

Ohkubo, S., Y. Kosugi, S. Takanashi, T. Mitani, and M. Tani. 2007. Comparison of the eddy covariance and automated closed chamber methods for evaluating nocturnal CO2 exchange in a Japanese cypress forest. Agricultural and Forest Meteorology **142**:50-65.

Ollinger, S. V., P. B. Reich, S. Frolking, L. C. Lepine, D. Y. Hollinger, and A. D. Richardson. 2013. Nitrogen cycling, forest canopy reflectance, and emergent properties of ecosystems. Proceedings of the National Academy of Sciences **110**:E2437-E2437.

Olofsson, P., F. Lagergren, A. Lindroth, J. Lindström, L. Klemedtsson, and L. Eklundh. 2007. Towards operational remote sensing of forest carbon balance across Northern Europe. Biogeosciences Discussions **4**:3143-3193.

Ouimette, A. P., S. V. Ollinger, A. D. Richardson, D. Y. Hollinger, T. F. Keenan, L. C. Lepine, and M. A. Vadeboncoeur. 2018. Carbon fluxes and interannual drivers in a temperate forest ecosystem assessed through comparison of top-down and bottom-up approaches. Agricultural and Forest Meteorology **256**:420-430.

Pan, Y., R. A. Birdsey, J. Fang, R. Houghton, P. E. Kauppi, W. A. Kurz, O. L. Phillips, A. Shvidenko, S. L. Lewis, and J. G. Canadell. 2011. A large and persistent carbon sink in the world's forests. Science **333**:988-993.

Phillips, C. L., B. Bond-Lamberty, A. R. Desai, M. Lavoie, D. Risk, J. Tang, K. Todd-Brown, and R. Vargas. 2017. The value of soil respiration measurements for interpreting and modeling terrestrial carbon cycling. Plant and Soil **413**:1-25.

Phillips, O. L., S. L. Lewis, T. R. Baker, K.-J. Chao, and N. Higuchi. 2008. The changing Amazon forest. Philosophical Transactions of the Royal Society B: Biological Sciences **363**:1819-1827.

Piao, S., Q. Liu, A. Chen, I. A. Janssens, Y. Fu, J. Dai, L. Liu, X. Lian, M. Shen, and X. Zhu. 2019. Plant phenology and global climate change: current progresses and challenges. Global Change Biology.

Pierce, M., and K. Raschke. 1980. Correlation between loss of turgor and accumulation of abscisic acid in detached leaves. Planta **148**:174-182.

Pilegaard, K., A. Ibrom, M. S. Courtney, P. Hummelshøj, and N. O. Jensen. 2011. Increasing net CO2 uptake by a Danish beech forest during the period from 1996 to 2009. Agricultural and Forest Meteorology **151**:934-946.

Ponge, J.-F. 2005. Emergent properties from organisms to ecosystems: towards a realistic approach. Biological Reviews **80**:403-411.

Pook, E. 1984a. Canopy dynamics of Eucalyptus maculata Hook. I. Distribution and dynamics of leaf populations. Australian journal of botany **32**:387-403.

Pook, E. 1984b. Canopy dynamics of Eucalyptus maculata Hook. II. Canopy leaf area balance. Australian Journal of Botany **32**:405-413.

Pook, E., A. Gill, and P. Moore. 1997. Long-term variation of litter fall, canopy leaf area and flowering in a Eucalyptus maculata forest on the south coast of New South Wales. Australian journal of botany **45**:737-755.

Poulter, B., D. Frank, P. Ciais, R. B. Myneni, N. Andela, J. Bi, G. Broquet, J. G. Canadell, F. Chevallier, Y. Y. Liu, S. W. Running, S. Sitch, and G. R. van der Werf. 2014. Contribution of semi-arid ecosystems to interannual variability of the global carbon cycle. Nature **509**:600-603.

Prior, L., D. Bowman, and D. Eamus. 2004. Seasonal differences in leaf attributes in Australian tropical tree species: family and habitat comparisons. Functional Ecology **18**:707-718.

Prior, L. D., and D. M. Bowman. 2014. Big eucalypts grow more slowly in a warm climate: evidence of an interaction between tree size and temperature. Global Change Biology **20**:2793-2799.

Pumpanen, J., P. Kolari, H. Ilvesniemi, K. Minkkinen, T. Vesala, S. Niinistö, A. Lohila, T. Larmola, M. Morero, and M. Pihlatie. 2004. Comparison of different chamber techniques for measuring soil CO2 efflux. Agricultural and Forest Meteorology **123**:159-176.

Rastetter, E. B., J. D. Aber, D. P. Peters, D. S. Ojima, and I. C. Burke. 2003. Using mechanistic models to scale ecological processes across space and time. BioScience **53**:68-76.

Reich, P., C. Uhl, M. Walters, and D. Ellsworth. 1991. Leaf lifespan as a determinant of leaf structure and function among 23 Amazonian tree species. Oecologia **86**:16-24.

Reich, P. B., D. S. Falster, D. S. Ellsworth, I. J. Wright, M. Westoby, J. Oleksyn, and T. D. Lee. 2009. Controls on declining carbon balance with leaf age among 10 woody species in Australian woodland: do leaves have zero daily net carbon balances when they die? New Phytologist **183**:153-166.

Reichstein, M., E. Falge, D. Baldocchi, D. Papale, M. Aubinet, P. Berbigier, C. Bernhofer, N. Buchmann, T. Gilmanov, A. Granier, T. Grunwald, K. Havrankova, H. Ilvesniemi, D. Janous, A. Knohl, T. Laurila, A. Lohila, D. Loustau, G. Matteucci, T. Meyers, F. Miglietta, J. M. Ourcival, J. Pumpanen, S. Rambal, E. Rotenberg, M. Sanz, J. Tenhunen, G. Seufert, F. Vaccari, T. Vesala, D. Yakir, and R. Valentini. 2005. On the separation of net ecosystem exchange into assimilation and ecosystem respiration: review and improved algorithm. Global Change Biology **11**:1424-1439.

Renchon, A. A., A. Griebel, D. Metzen, C. A. Williams, B. Medlyn, R. A. Duursma, C. V. Barton, C. Maier, M. M. Boer, and P. Isaac. 2018. Upside-down fluxes Down Under: CO 2 net sink in winter and net source in summer in a temperate evergreen broadleaf forest. Biogeosciences **15**:3703-3716.

Resco de Dios, V., A. W. Fellows, R. H. Nolan, M. M. Boer, R. A. Bradstock, F. Domingo, and M. L. Goulden. 2015. A semi-mechanistic model for predicting the moisture content of fine litter. Agricultural and Forest Meteorology **203**:64-73.

Restrepo-Coupe, N., A. Huete, K. Davies, J. Cleverly, J. Beringer, D. Eamus, E. v. Gorsel, L. B. Hutley, and W. S. Meyer. 2016. MODIS vegetation products as proxies of photosynthetic potential along a gradient of meteorologically and biologically driven ecosystem productivity. Biogeosciences **13**:5587-5608.

Restrepo-Coupe, N., N. M. Levine, B. O. Christoffersen, L. P. Albert, J. Wu, M. H. Costa, D. Galbraith, H. Imbuzeiro, G. Martins, and A. C. Araujo. 2017a. Do dynamic global vegetation models capture the seasonality of carbon fluxes in the Amazon basin? A data-model intercomparison. Global change biology **23**:191-208.

Restrepo-Coupe, N., N. M. Levine, B. O. Christoffersen, L. P. Albert, J. Wu, M. H. Costa, D. Galbraith, H. Imbuzeiro, G. Martins, and A. C. da Araujo. 2017b. Do dynamic global vegetation models capture the seasonality of carbon fluxes in the Amazon basin? A data-model intercomparison. Global Change Biology **23**:191-208.

Reyes-Fox, M., H. Steltzer, M. Trlica, G. S. McMaster, A. A. Andales, D. R. LeCain, and J. A. Morgan. 2014. Elevated CO 2 further lengthens growing season under warming conditions. Nature **510**:259.

Richardson, A. D., R. S. Anderson, M. A. Arain, A. G. Barr, G. Bohrer, G. Chen, J. M. Chen, P. Ciais, K. J. Davis, and A. R. Desai. 2012. Terrestrial biosphere models need better representation of vegetation phenology: results from the N orth A merican C arbon P rogram S ite S ynthesis. Global Change Biology **18**:566-584.

Richardson, A. D., T. Andy Black, P. Ciais, N. Delbart, M. A. Friedl, N. Gobron, D. Y. Hollinger, W. L. Kutsch, B. Longdoz, and S. Luyssaert. 2010. Influence of spring and autumn phenological transitions on forest ecosystem productivity. Philosophical Transactions of the Royal Society B: Biological Sciences **365**:3227-3246.

Saleska, S. R., S. D. Miller, D. M. Matross, M. L. Goulden, S. C. Wofsy, H. R. Da Rocha, P. B. De Camargo, P. Crill, B. C. Daube, and H. C. De Freitas. 2003. Carbon in Amazon forests: unexpected seasonal fluxes and disturbance-induced losses. Science **302**:1554-1557.

Schimel, D. S., J. I. House, K. A. Hibbard, P. Bousquet, P. Ciais, P. Peylin, B. H. Braswell, M. J. Apps, D. Baker, and A. Bondeau. 2001. Recent patterns and mechanisms of carbon exchange by terrestrial ecosystems. Nature **414**:169-172.

Schuur, E. A. 2003. Productivity and global climate revisited: the sensitivity of tropical forest growth to precipitation. Ecology **84**:1165-1170.

Shi, H., L. Li, D. Eamus, A. Huete, J. Cleverly, X. Tian, Q. Yu, S. Wang, L. Montagnani, and V. Magliulo. 2017. Assessing the ability of MODIS EVI to estimate terrestrial ecosystem gross primary production of multiple land cover types. Ecological indicators **72**:153-164.

Smith, F. W., and J. N. Long. 2001. Age-related decline in forest growth: an emergent property. Forest Ecology and Management **144**:175-181.

Smith, M. 2018. Non-structural carbohydrate storage and use in eucalypt trees of south-east Australia.

Song, X.-P., M. C. Hansen, S. V. Stehman, P. V. Potapov, A. Tyukavina, E. F. Vermote, and J. R. Townshend. 2018. Global land change from 1982 to 2016. Nature **560**:639.

Speckman, H. N., J. M. Frank, J. B. Bradford, B. L. Miles, W. J. Massman, W. J. Parton, and M. G. Ryan. 2015. Forest ecosystem respiration estimated from eddy covariance and chamber measurements under high turbulence and substantial tree mortality from bark beetles. Global Change Biology **21**:708-721.

Stenberg, P. 2006. A note on the G-function for needle leaf canopies. Agricultural and Forest Meteorology **136**:76-79.

Tang, X., X. Wang, Z. Wang, D. Liu, M. Jia, Z. Dong, J. Xie, Z. Ding, H. Wang, and X. Liu. 2013. Influence of vegetation phenology on modelling carbon fluxes in temperate deciduous forest by exclusive use of MODIS time-series data. International journal of remote sensing **34**:8373-8392.

Tans, P. P., I. Y. Fung, and T. Takahashi. 1990. Observational contrains on the global atmospheric CO2 budget. Science **247**:1431-1438.

Tcherkez, G., R. Schaeufele, S. Nogues, C. Piel, A. Boom, G. Lanigan, C. Barbaroux, C. Mata, S. Elhani, and D. Hemming. 2010. On the 13C/12C isotopic signal of day and night respiration at the mesocosm level. Plant, Cell & Environment **33**:900-913.

Teets, A., S. Fraver, D. Y. Hollinger, A. R. Weiskittel, R. S. Seymour, and A. D. Richardson. 2018. Linking annual tree growth with eddy-flux measures of net ecosystem productivity across twenty years of observation in a mixed conifer forest. Agricultural and Forest Meteorology **249**:479-487.

Thom, A. 1972. Momentum, mass and heat exchange of vegetation. Quarterly Journal of the Royal Meteorological Society **98**:124-134.

Thomas, C. K., J. G. Martin, B. E. Law, and K. Davis. 2013. Toward biologically meaningful net carbon exchange estimates for tall, dense canopies: multi-level eddy covariance observations and canopy coupling regimes in a mature Douglas-fir forest in Oregon. Agricultural and Forest Meteorology **173**:14-27.

Tjoelker, M. G., J. Oleksyn, and P. B. Reich. 2001. Modelling respiration of vegetation: evidence for a general temperature-dependent Q10. Global Change Biology **7**:223-230.

Trenberth, K. E. 1983. What are the seasons? Bulletin of the American Meteorological Society **64**:1276-1282.

Trudinger, C. M., V. Haverd, P. R. Briggs, and J. G. Canadell. 2016. Interannual variability in Australia's terrestrial carbon cycle constrained by multiple observation types. Biogeosciences **13**:6363-6383.

Ummenhofer, C. C., M. H. England, P. C. McIntosh, G. A. Meyers, M. J. Pook, J. S. Risbey, A. S. Gupta, and A. S. Taschetto. 2009. What causes southeast Australia's worst droughts? Geophysical Research Letters **36**.

van Gorsel, E., J. A. J. Berni, P. Briggs, A. Cabello-Leblic, L. Chasmer, H. A. Cleugh, J. Hacker, S. Hantson, V. Haverd, D. Hughes, C. Hopkinson, H. Keith, N. Kljun, R.

Leuning, M. Yebra, and S. Zegelin. 2013. Primary and secondary effects of climate variability on net ecosystem carbon exchange in an evergreen Eucalyptus forest. Agricultural and Forest Meteorology **182-183**:248-256.

Van Gorsel, E., R. Leuning, H. A. Cleugh, H. Keith, and T. Suni. 2007. Nocturnal carbon efflux: reconciliation of eddy covariance and chamber measurements using an alternative to the u.-threshold filtering technique. Tellus B: Chemical and Physical Meteorology **59**:397-403.

Van Gorsel, E., S. Wolf, J. Cleverly, P. Isaac, V. Haverd, C. M. Ewenz, S. Arndt, J. Beringer, V. R. De Dios, and B. J. Evans. 2016. Carbon uptake and water use in woodlands and forests in southern Australia during an extreme heat wave event in the" angry Summer" of 2012/2013.

Vickers, D., and L. Mahrt. 1997. Quality control and flux sampling problems for tower and aircraft data. Journal of Atmospheric and Oceanic Technology **14**:512-526.

Walker, A. P., P. J. Hanson, M. G. De Kauwe, B. E. Medlyn, S. Zaehle, S. Asao, M. Dietze, T. Hickler, C. Huntingford, and C. M. Iversen. 2014. Comprehensive ecosystem model-data synthesis using multiple data sets at two temperate forest free-air CO2 enrichment experiments: Model performance at ambient CO2 concentration. Journal of Geophysical Research: Biogeosciences **119**:937-964.

Walker, M. D., R. C. Ingersoll, and P. J. Webber. 1995. Effects of interannual climate variation on phenology and growth of two alpine forbs. Ecology **76**:1067-1083.

Wang, X., C. Wang, and B. Bond-Lamberty. 2017. Quantifying and reducing the differences in forest CO2-fluxes estimated by eddy covariance, biometric and chamber methods: A global synthesis. Agricultural and Forest Meteorology **247**:93-103.

Webb, E. K., G. I. Pearman, and R. Leuning. 1980. Correction of flux measurements for density effects due to heat and water vapour transfer. Quarterly Journal of the Royal Meteorological Society **106**:85-100.

Wehr, R., J. Munger, J. McManus, D. Nelson, M. Zahniser, E. Davidson, S. Wofsy, and S. Saleska. 2016. Seasonality of temperate forest photosynthesis and daytime respiration. Nature **534**:680.

White, M., S. W. Running, and P. E. Thornton. 1999. The impact of growing-season length variability on carbon assimilation and evapotranspiration over 88 years in the eastern US deciduous forest. International Journal of Biometeorology **42**:139-145.

Wilczak, J. M., S. P. Oncley, and S. A. Stage. 2001. Sonic anemometer tilt correction algorithms. Boundary-Layer Meteorology **99**:127-150.

Williams, R., B. Myers, W. Muller, G. Duff, and D. Eamus. 1997. Leaf phenology of woody species in a north Australian tropical savanna. Ecology **78**:2542-2558.

Wilson, K., A. Goldstein, E. Falge, M. Aubinet, D. Baldocchi, P. Berbigier, C. Bernhofer, R. Ceulemans, H. Dolman, and C. Field. 2002. Energy balance closure at FLUXNET sites. Agricultural and Forest Meteorology **113**:223-243.

Wilson, K. B., D. D. Baldocchi, and P. J. Hanson. 2001. Leaf age affects the seasonal pattern of photosynthetic capacity and net ecosystem exchange of carbon in a deciduous forest. Plant Cell and Environment **24**:571-583.

Windsor, D. M. 1990. Climate and moisture variability in a tropical forest: long-term records from Barro Colorado Island, Panama.

Wofsy, S., M. Goulden, J. Munger, S.-M. Fan, P. Bakwin, B. Daube, S. Bassow, and F. Bazzaz. 1993. Net exchange of CO2 in a mid-latitude forest. Science **260**:1314-1317.

Wu, J., L. P. Albert, A. P. Lopes, N. Restrepo-Coupe, M. Hayek, K. T. Wiedemann, K. Guan, S. C. Stark, B. Christoffersen, N. Prohaska, J. V. Tavares, S. Marostica, H. Kobayashi, M. L. Ferreira, K. S. Campos, R. da Silva, P. M. Brando, D. G. Dye, T. E. Huxman, A. R. Huete, B. W. Nelson, and S. R. Saleska. 2016a. Leaf development and demography explain photosynthetic seasonality in Amazon evergreen forests. Science **351**:972-976.

Wu, J., L. P. Albert, A. P. Lopes, N. Restrepo-Coupe, M. Hayek, K. T. Wiedemann, K. Y. Guan, S. C. Stark, B. Christoffersen, N. Prohaska, J. V. Tavares, S. Marostica, H. Kobayashi, M. L. Ferreira, K. S. Campos, R. da Silva, P. M. Brando, D. G. Dye, T. E. Huxman, A. R. Huete, B. W. Nelson, and S. R. Saleska. 2016b. Leaf development and demography explain photosynthetic seasonality in Amazon evergreen forests. Science **351**:972-976.

Wu, J., K. Guan, M. Hayek, N. Restrepo-Coupe, K. T. Wiedemann, X. Xu, R. Wehr, B. O. Christoffersen, G. Miao, and R. da Silva. 2017. Partitioning controls on Amazon forest photosynthesis between environmental and biotic factors at hourly to interannual timescales. Global Change Biology **23**:1240-1257.

Wujeska-Klause, A., K. Y. Crous, O. Ghannoum, and D. S. Ellsworth. 2019. Leaf age and eCO2 both influence photosynthesis by increasing light harvesting in mature Eucalyptus tereticornis at EucFACE. Environmental and Experimental Botany:103857.

Wujeska-Klause, A., K. Y. Crous, O. Ghannoum, and D. S. Ellsworth. 2019. Lower photorespiration in elevated CO2 reduces leaf N concentrations in mature Eucalyptus trees in the field. Global Change Biology.

Xia, J. Y., S. L. Niu, P. Ciais, I. A. Janssens, J. Q. Chen, C. Ammann, A. Arain, P. D. Blanken, A. Cescatti, D. Bonal, N. Buchmann, P. S. Curtis, S. P. Chen, J. W. Dong, L. B. Flanagan, C. Frankenberg, T. Georgiadis, C. M. Gough, D. F. Hui, G. Kiely, J. W. Li, M. Lund, V. Magliulo, B. Marcolla, L. Merbold, L. Montagnani, E. J. Moors, J. E. Olesen, S. L. Piao, A. Raschi, O. Roupsard, A. E. Suyker, M. Urbaniak, F. P. Vaccari, A. Varlagin, T. Vesala, M. Wilkinson, E. Weng, G. Wohlfahrt, L. M. Yan, and Y. Q. Luo. 2015. Joint control of terrestrial gross primary productivity by plant phenology and physiology. Proceedings of the National Academy of Sciences of the United States of America **112**:2788-2793.

Yang, Y., R. J. Donohue, T. R. McVicar, M. L. Roderick, and H. E. Beck. 2016. Long-term CO2 fertilization increases vegetation productivity and has little effect on hydrological partitioning in tropical rainforests. Journal of Geophysical Research: Biogeosciences **121**:2125-2140.

Yi, C., D. Ricciuto, R. Li, J. Wolbeck, X. Xu, M. Nilsson, L. Aires, J. D. Albertson, C. Ammann, and M. A. Arain. 2010. Climate control of terrestrial carbon exchange across biomes and continents. Environmental Research Letters **5**:034007.

Zhang, Y., Z. Tan, Q. Song, G. Yu, and X. Sun. 2010. Respiration controls the unexpected seasonal pattern of carbon flux in an Asian tropical rain forest. Atmospheric Environment **44**:3886-3893.

Zhang, Y., X. Xiao, X. Wu, S. Zhou, G. Zhang, Y. Qin, and J. Dong. 2017. A global moderate resolution dataset of gross primary production of vegetation for 2000–2016. Scientific data **4**:170165.

Zhu, Z., S. Piao, R. B. Myneni, M. Huang, Z. Zeng, J. G. Canadell, P. Ciais, S. Sitch, P. Friedlingstein, and A. Arneth. 2016. Greening of the Earth and its drivers. Nature Climate Change **6**:791.

Zuidema, P. A., B. Poulter, and D. C. Frank. 2018. A Wood Biology Agenda to Support Global Vegetation Modelling. Trends in plant science.